Development of an eye-safe solid-state tunable laser transmitter around 1.45 μm based on Cr^{4+}:YAG crystal for lidar applications

Dissertation zur Erlangung des Doktorgrades der Naturwissenschaften (Dr. rer. nat.)

Fakultät Naturwissenschaften
Universität Hohenheim

Institut für Physik und Meteorologie

vorgelegt von
Anna Petrova-Mayor

aus Vratsa, Bulgarien
2008

This thesis was accepted as a doctoral dissertation in fulfillment of the requirements for the degree "Doktor der Naturwissenschaften" by the Faculty of Natural Sciences at the University of Hohenheim, Stuttgart, Germany on 24 October 2007.

Date of oral examination: 2 April 2008

Examination committee:

Supervisor and reviewer:	Prof. Dr. V. Wulfmeyer Institute for Physics and Meteorology, University of Hohenheim
Co-reviewer:	Prof. Dr. G. Huber Institute for Laser Physics, University of Hamburg
Additional examiner:	Prof. Dr. K. Jetter Institute for Applied Mathematics and Statistics, University of Hohenheim
Dean:	Prof. Dr. H. Breer Faculty of Natural Sciences, University of Hohenheim

Abstract

A gain switched tunable Cr^{4+}:YAG laser was developed using a Q-switched flash-lamp–pumped Nd:YAG pump laser at 10 Hz. A vacuum spatial filter (VSF) was designed in order to filter the "hot spots" of the pump beam profile. As a result of applying the VSF, a nearly Gaussian-shaped beam profile was achieved which enabled safe pumping of the Cr^{4+}:YAG crystal with pulse energies in excess of 100 mJ. An extensive experimental optimization of the efficiency of the wavelength converter was performed. A maximum output energy of ≈7 mJ at 1430–1450 nm, corresponding to ≈7 % conversion efficiency (with regard to absorbed pump energy), and a pulse duration of 30–35 ns were obtained with a 25-cm-long stable resonator. Tunability in the range 1350–1500 nm and spectral linewidth of ≈200 GHz were demonstrated using a 3-plate birefringent filter. The laser was multimode with a flat-top profile and sufficiently good $M^2 \approx 4$.

The performance and size of the laser are acceptable for use in a laboratory-based non-scanning lidar system if a narrow-band birefringent filter is installed. In order to employ a scanning mobile lidar, high pulse frequency (≥100 Hz) of the pump laser for the Cr^{4+}:YAG laser is required. The tunability permits the improvement of the laser transmitter for water-vapor DIAL measurements at on-line wavelengths of approximately 1459 nm or 1484 nm if injection-seeding is applied.

Zusammenfassung

Ein gain-geschalteter, abstimmbarer Cr^{4+}:YAG Wellenlängenkonverter wurde entwickelt. Er wurde mit einem gütegeschalteten blitzlampengepumpten Nd:YAG-Laser mit einer Repetitionsrate von 10 Hz und einer Pulsdauer von 6–8 gepumpt. Dieses System ist ein erster Schritt zur Entwicklung eines augensicheren Wasserdampf-DIAL-Systems bei 1459 nm und 1484 nm. Ein Vakuum-Raumfilter (VRF) wurde aufgebaut, um die Hot Spots im Pumpstrahlprofil herauszufiltern. Mit dem VRF wurde ein nahezu Gaußsches Pumprofil erzielt. Das ermöglichte das Pumpen von Cr^{4+}:YAG mit Pulsenergien von mehr als 100 mJ, ohne den Kristall zu beschädigen. Eine experimentelle Optimierung der Effizienz des Wellenlängenkonverters wurde durchgeführt. Eine maximale Ausgangsenergie von ≈7 mJ bei 1430–1450 nm, was ≈7 % Konversionseffizienz (bezüglich der absorbierten Pumpenergie) entspricht, und eine Pulslänge von 30–35 ns wurden mit einem 25 cm langen Resonator erreicht. Laserabstimmbarkeit im Wellenlängenbereich von 1350–1500 nnm und eine spektrale Linienbreite von ≈200 GHz wurden mit einem 3-Platten doppelbrechenden Filter demonstriert. Der Cr^{4+}:YAG Laser besitzt ein Multimoden-Flat top-Strahlprofil und einen guten M^2 Wert von ungefähr 4.

Die Effizienz und die Größe des Lasers sind akzeptabel zur Anwendung in einem nicht abtastenden Labor-Lidarsystem, falls ein schmalbandiger doppelbrechender Filter benutzt wird. Um Cr^{4+}:YAG als Laser für ein abtastendes mobiles Lidar zu verwenden, ist ein kompakter Pumplaser mit hoher Repetitionsrate (≥100 Hz) erforderlich. In Verbindung mit diesem Pumplaser und der Anwendung der Injection-Seeding-Technik hat der Laser das Potential als Transmitter für ein augensicheren Wasserdampf-DIAL-System eingesetzt zu werden.

Contents

Abstract i
Zusammenfassung ii
List of Figures vi
List of Tables xi

1 Introduction **1**
1.1 Motivation 1
1.2 Aerosol backscatter lidar 3
1.3 Eye-safety considerations and choice of operating wavelength 7
1.4 Wavelength converters in the eye-safe spectral region around 1500 nm. 9
1.4.1 Raman shifter 9
1.4.2 OPO 10
1.4.3 Solid-state lasers 11
1.5 The goal of this project 12

2 Laser theory **13**
2.1 Laser dynamics 14
2.2 Laser resonator modes 18
2.2.1 Transverse modes 18
2.2.2 Longitudinal modes 19
2.2.3 Characteristics of the fundamental mode TEM_{00} 20
2.3 Beam propagation of laser modes 21
2.4 Thermal lensing of the laser crystal 23
2.5 Design of a dynamically stable linear resonator 24
2.5.1 Dynamical stability 25
2.5.2 Misalignment sensitivity 27
2.6 Properties of real laser beams 29
2.6.1 Beam width 29
2.6.2 Beam propagation factor M^2 30
2.6.3 Measurement of M^2 31

3 Pump configuration **32**
3.1 Pump laser . . . 32
3.1.1 IBL pump laser . . . 33
3.1.2 Continuum pump laser . . . 34
3.2 Vacuum spatial filter . . . 38
3.2.1 Theory of operation . . . 38
3.2.2 Design . . . 38
3.2.3 Improvement of the pump beam characteristics . . . 42
3.3 Cooling of the laser crystal . . . 42

4 Chromium YAG laser **44**
4.1 Laser crystal . . . 44
4.1.1 Physical properties . . . 44
4.1.2 Laser properties . . . 45
4.2 Measurement of the pump absorption . . . 48
4.3 Measurement of thermal lensing . . . 52
4.4 Resonator design . . . 55
4.5 Experimental optimization of the laser performance . . . 61
4.5.1 Optimization of the mode size . . . 61
4.5.2 Optimization of the pump beam diameter . . . 69
4.5.3 Optimization of the temperature of the crystal . . . 72
4.5.4 Discussion of the experimental results . . . 79
4.6 Tunable Cr^{4+}:YAG laser . . . 87
4.6.1 Tuning element . . . 87
4.6.2 Experimental set up for measurement of the spectral characteristics of the laser . . . 89
4.6.3 Experimental results . . . 90

5 Summary **101**

6 Conclusions and outlook **105**

A Suitable water vapor absorption lines for DIAL **108**

B Ray transfer matrix **113**

C Thermal lensing of Cr^{4+}:YAG for PRF 125 Hz and 250 Hz **114**

D Two-rod resonator **115**

E Birefringent filter **120**

F Grating spectrometer **121**

Bibliography **123**

List of Figures

1.1 Schematic of a lidar. 4
1.2 Maximum permissible energy as a function of the wavelength for a scanning and stationary beam. 7
1.3 Transmission of a standard atmosphere. 9

2.1 Principle of a laser. 13
2.2 Gaussian beam. 20
2.3 Linear resonator with variable thermal lens with focal length f_T and other intracavity elements. 26

3.1 IBL Nd:YAG pump laser. 33
3.2 Continuum Surelite III Nd:YAG pump laser. 34
3.3 Set up for achieving horizontal polarization (with a thin film polarizer TFP_1) and external energy attenuation (with a half waveplate $\lambda/2$ P_1 and TFP_2). 35
3.4 Beam profile at distances 1.12 m (left) and 2.12 m (right) after the laser output. 36
3.5 M^2 measurement of the Surelite Nd:YAG laser beam using a PLCX lens with a focal length of 572.7 mm at 1064 nm. 37
3.6 Principal of spatial filtering. 38
3.7 Pump configuration. 40
3.8 Variation of the maximum energy density of the beam propagating after the VSF's input focusing lens for 100 mJ pulse energy. 40
3.9 Photograph of the vacuum spatial filter in the lab. 41
3.10 Beam profiles after the vacuum spatial filter. 42
3.11 Solid model of the crystal cooler. 43

4.1 Energy level diagram of Cr^{4+} ions. 46
4.2 Cr^{4+}:YAG laser crystal. 49
4.3 Theoretical fit of the experimental data obtained with a 20 mm long laser rod with a small-signal absorption coefficient $\alpha = 2.2\,cm^{-1}$. . . . 49
4.4 Theoretical transmission of the pump energy at 1064 nm as a function of the pump energy density for Cr^{4+}:YAG crystal with various lengths. 50

4.5 Theoretical fit to the experimentally measured transmission of the 40-mm long Cr^{4+}:YAG crystal. 51
4.6 Experimental transmission of the new crystal vs. pump pulse energy for two pump beam sizes as indicated in the legend. 52
4.7 Experimental setup for measuring the thermal focal length with the pump-probe technique. 53
4.8 Matrix method for calculation of the thermal focal length. 54
4.9 Mode radius and overall misalignment sensitivity in the tangential plane vs. the distance between the crystal and the output coupler, for output couplers with different radius of curvature R_2. 57
4.10 Mode radius and overall misalignment sensitivity as a function of the thermal focal length for different resonator configurations. 58
4.11 Propagation of the fundamental laser mode in a resonator with $R_1 \rightarrow \infty$, L_1= 0.1 m, L_2= 0.08 m. 59
4.12 Propagation of the fundamental laser mode in a resonator with $R_1 \rightarrow \infty$, L_1= 0.1 m, L_2= 0.57 m. 60
4.13 Propagation of the fundamental laser mode in a resonator with $R_1 \rightarrow \infty$, L_1= 0.1 m, L_2= 0.8 m. 60
4.14 Experimental setup of Cr^{4+}:YAG laser. 62
4.15 Output energy vs. absorbed pump energy obtained with resonators with radius of the fundamental mode in the range 0.45 mm to 0.56 mm. 63
4.16 Output energy vs. absorbed pump energy obtained with resonators with radius of the fundamental mode in the range 0.6 mm to 0.82 mm. 64
4.17 Conversion efficiency for various resonator configurations using flat rear mirror placed at L_1= 0.1 m from the crystal and an output coupler as indicated in the legend. 65
4.18 Build up time and pulse width obtained with resonators with radius of the fundamental mode in the range 0.45 mm to 0.56 mm. 66
4.19 Build up time and pulse width obtained with resonators with radius of the fundamental mode in the range 0.6 mm to 0.82 mm. 67
4.20 Build up time and pulse width obtained with resonators with radius of the fundamental mode in the range 0.75 mm to 0.82 mm. 68
4.21 Power curves obtained with resonators with radius of the fundamental mode in the range 0.45 mm to 0.8 mm. 69
4.22 Conversion efficiency obtained with resonators with radius of the fundamental mode in the range 0.45 mm to 0.8 mm. 70
4.23 Build up time and pulse width obtained with resonators with radius of the fundamental mode in the range 0.45 mm to 0.8 mm. 71
4.24 Transmission of the pump radiation as a function of the pump energy for different temperature of the crystal. 72
4.25 Output energy vs. temperature of the crystal for different absorbed pump energies. 73

4.26 Laser pulse duration vs. temperature of the crystal for different absorbed pump energies. 74
4.27 Build up time vs. temperature of the crystal for different absorbed pump energies. 75
4.28 Output energy vs. temperature of the crystal for absorbed pump energy of 115 mJ and different resonator configurations. 76
4.29 Output energy and conversion efficiency as a function of the absorbed energy for different resonator configurations using a flat rear mirror placed at L_1= 0.1 m from the crystal and output couplers as indicated in the legend. 77
4.30 Build up time and pulse width vs. absorbed pump energy for various resonators with a flat rear mirror placed at L_1= 0.1 m from the crystal and output couplers as indicated in the legend. 78
4.31 Optimization of the laser performance for various resonator configurations with a flat rear mirror placed at L_1= 0.1 m and output coupler as indicated under each image. 79
4.32 Theoretical inversion population ratio $(n_i - n_f)/n_T$, experimental transmission T_{exp} and its fit T_{fit} vs. pump energy fluence. 80
4.33 Theoretical laser output energy as a function of the pump energy fluence for different values of the ratio $\sigma_{ESA_L}/\sigma_{SE}$. 81
4.34 Theoretical output energy as a function of the pump energy fluence for different values of the dissipative losses in the resonator. 82
4.35 Theoretical fit of the experimental results obtained with resonator with a flat rear mirror placed at L_1= 0.1 m and an output coupler R_2= 3 m, $\mathcal{R}$=90 %, and L_2= 0.08 m. 83
4.36 Theoretical pulse duration for the tested resonators with a flat rear mirror placed at distance L_1= 0.1 m and an output coupler R_2= 3 m, $\mathcal{R}$=90 %. 86
4.37 Laser resonator with a 3-stage birefringent filter at the Brewster angle. 87
4.38 Experimental set up for measuring the tuning range of Cr^{4+}:YAG with a grating spectrometer. 89
4.39 Tuning curves of two resonator configurations for 105 mJ absorbed pump energy. 91
4.40 Pulse width and build up time as a function of the laser wavelength for 105 mJ absorbed pump energy. 92
4.41 Output energy at 1432 nm vs. absorbed energy of the resonator configuration L_1= 0.065 m, L_2= 0.135 m, R_2= 2 m. 93
4.42 Output energy at 1432 nm vs. absorbed energy of the resonator configuration L_1= 0.065 m, L_2= 0.57 m, R_2= 2 m. 94
4.43 Tuning curves for different absorbed pump energies, obtained from two resonator configurations in multimode regime. 95

4.44 Linewidth at 1455 nm, obtained with the resonator L_2= 0.135 m and R_2= 2 m with reflectivity $\mathcal{R}$ =90 % and $\mathcal{R}$ =80 %. 96
4.45 Generation of high order modes by increasing the pump energy. . . . 97
4.46 Laser beam profile at a distance 1.78 m (1.88 m in (d)) after the output coupler for various resonator configurations with output coupler R_2= 2 m. 98
4.47 Beam propagation after PLCX lens with focal length f=620 mm. The resonator configuration was L_1= 0.065 m, L_2= 0.135 m, R_2= 2 m, $\mathcal{R}$=80 %, with BF and T_{opt}= 34 °C. 99
4.48 Beam propagation after PLCX lens with focal length f=620 mm. The resonator configuration was L_1= 0.065 m, L_2= 0.135 m, R_2= 2 m, $\mathcal{R}$=80 %, with BF and T_{opt}= 34 °C. 99
4.49 Beam propagation after PLCX lens with focal length f=620 mm. The resonator configuration was L_1= 0.065 m, L_2= 0.57 m, R_2= 2 m, $\mathcal{R}$=80 %, with BF and T_{opt}= 34 °C. 99
4.50 Beam propagation after PLCX lens with focal length f=620 mm. The resonator configuration was L_1= 0.065 m, L_2= 0.135 m, $\mathcal{R}$=80 %, without BF and T_{opt}= 34 °C. 100

A.1 Water-vapor absorption lines in the spectral region 1400–1550 nm with line strength of $10^{-24} - 10^{-22}$ cm and ground-state energy $< 320\,\mathrm{cm}^{-1}$. 109
A.2 Optical depth of water vapor absorption lines in different spectral regions for standard atmosphere (altitude: sea level, air temperature: 296 K, partial pressure: 775 Pa) and 100 m path length. 110
A.3 Optical depth of water vapor absorption lines in different spectral regions for standard atmosphere (altitude: sea level, air temperature: 296 K, partial pressure: 775 Pa) and 100 m path length. 111

C.1 Thermal lens focal length as a function of the absorbed pump power. 114

D.1 Experimental arrangement for a two-rod cavity pumped from opposing ends with the equivalent pump energy. 115
D.2 Resonator parameters as a function of the distance between the rear mirror and the first rod L_1 and the distance between the rods d in the tangential plane. 116
D.3 Resonator parameters as a function of the distance between the rear mirror and the first rod L_1 and the distance between the rods d in the sagittal plane. 117
D.4 Sensitivity of the laser rods to misalignment of the cavity mirrors as a function of the distance between the rear mirror and the first rod L_1 and the distance between the rods d in the tangential plane. 118
D.5 Sensitivity of the laser rods to misalignment of the cavity mirrors as a function of the distance between the rear mirror and the first rod L_1 and the distance between the rods d in the sagittal plane. 118

D.6 Stability zones for the resonator with R_1=∞ m, L_1=0.05 m, R_2=1 m, L_2=0.45 m, and d=0.02 m. 119
D.7 Propagation of the fundamental laser mode in a 2-rod resonator. . . . 119

E.1 Transmission of a 5-stage birefringent filter for single pass. 120

F.1 Grating spectrometer in Czerny-Turner configuration 121

List of Tables

1.1 Desired specifications of the new lidar transmitter 12

3.1 Specifications of the Nd:YAG lasers used to pump the Cr^{4+}:YAG crystal 32

4.1 Physical parameters of Cr^{4+}:YAG crystal 45
4.2 Published values of the initial absorption coefficient and the cross-section of the transitions in Cr^{4+}:YAG crystal 47

A.1 Suitable water vapor absorption lines for ground-based DIAL. 112

Acknowledgments

I would like to thank Prof. Dr. Volker Wulfmeyer for giving me the opportunity to work on this project and earn a Ph.D. I appreciate the many helpful discussions on the theoretical and experimental part of this study and for finding an alternative solution at NCAR in order to complete this project. Dr. Andreas Behrendt provided oversight of my project, helped with Mathematica, and commented on the first draft.

I also thank the NCAR EOL Directorate and the Remote Sensing Facility for use of their laboratory and equipment to achieve these results. I am indebted to Dr. Petter Weibring for providing technical support, frequent discussions, and critical review of the first draft. Dr. Scott Spuler was always ready to discuss the ongoing progress and provide insight. Thanks to Scott also for sharing the beam diagnostic devices, for lending some optics and mounts.

I wish to thank Dr. S. Kück from the Physikalisch-Technische Bundesanstalt, Braunschweig, Germany, and Dr. P. Mathieu from the Defense Research Establishment Valcartier, Quebec, Canada, for helpful discussions about the Cr^{4+}:YAG laser performance.

The development of this laser benefited from the contributions of many. Prof. G. Huber and Dr. K. Petermann from the University of Hamburg provided the first Cr^{4+}:YAG crystal. Prof. S. Svanberg from the Department of Atomic Physics at the Lund Institute of Technology, Sweden, kindly loaned a significant part of the vacuum spatial filter. The vacuum gauge, the vacuum testing equipment, and the grating spectrometer were borrowed from Dr. A. Fried, EOL NCAR. The custom parts were created by O. Eberwein from the machine shop at IPM and NCAR's Design and Fabrication Services (DFS). The clamp shells were designed by Jack Fox from DFS.

Thanks to my colleagues at IPM: Max Shiler,who is also a very good friend, Gerd Wagner, Sandip Pal, Matthias Grzeschnik and Marcus Radlach for creating nice and positive working atmosphere.

I would like to thank my Boulder friends Marga Powell, Christoph Senff and Joyce Jay for their support. I thank my Mother, who has always put my education as the highest priority. The biggest thanks goes to my husband for his love, support and encouragement. I particularly appreciate his patience and many trips to Stuttgart.

Dedicated to my Mother

Chapter 1

Introduction

1.1 Motivation

LIght Detection And Ranging (LIDAR) is an active optical remote sensing technology that provides images of atmospheric structure and quantative measurements of atmospheric variables. Lidars transmit short laser pulses into the atmosphere and detect the elastically and inelastically backscattered radiation from molecules and aerosol particles (diameters range from approximately 0.001 to 100 μm). Molecules and fine aerosol particles scatter the light according to Rayleigh scattering theory—inversely proportional to the fourth power of the transmitted laser wavelength [158]. Spherical aerosol particles with diameters on the order of the transmitted laser wavelength scatter the light according to the Mie theory [158]. Scattering from non-spherical particles require different treatment [110]. The lidar sensitivity to different size particles is dependent on the transmitted wavelength and the concentration of the particles. Clouds and precipitation, which are composed of very large particles (>100's μm) cause strong backscatter and extinction of the lidar signal. Thus, lidars are ideal for probing the visually clear atmosphere to determine the distribution of aerosol backscatter and some trace gases. Lidars are also of use in observing optically thin clouds such as cirrus [41, 125].

Elastic backscatter lidars provide 2- to 4-dimensional images of the atmosphere continuously over periods ranging from hours to days and covering areas of tens of km^2. While lidars have contributed to virtually all aspects of atmospheric science, are particularly useful in studies of the atmospheric boundary layer (ABL) [88]. In general, the ABL is the lowest layer of the troposphere, the layer closest to the earth's surface. The ABL is defined by Stull [152] as "the part of the troposphere that is directly influenced by the presence of the earth's surface, and responds to surface forcing with a time scale of about an hour or less". In the ABL, elastic backscatter lidars are capable of detecting aerosol plumes and atmospheric structure that is far superior to the ability of the human eye or microwave radars. Moreover, they are able to map variability of the atmospheric structures with high temporal and spatial

resolution, which can not be obtained otherwise with passive remote sensing and in situ sensors.

By scanning the atmosphere from a ground site, lidars can monitor the emission of particle effluents from natural sources (e.g. forest fires [91, 159], volcano eruptions, wind blown dust) as well as anthropogenic induced plumes from industrial and agricultural sites. The aerosol particles have a direct impact on the climate, by absorbing and scattering the solar and terrestrial radiation, and affecting the cloud properties [65, 127]. Their indirect impact is by serving as cloud condensation nuclei [65, 92, 156, 157]. Aerosol particles also influence the chemistry and air quality and thus have an effect on human health [9, 27, 117, 171].

The appearance, motion and temporal evolution of aerosol plumes can be visualized by animating sequences of lidar images. The observations of the movement of aerosol structures over time can be used to extract vector wind fields [102, 149] and project the transport and dispersion of pollutants. This capability is useful in studies of pollutant dispersion, atmospheric chemistry, and respiratory health.

Simply by pointing the laser beam vertically, the depth of the cloud-free atmospheric boundary layer can be monitored, if the depth is greater than the minimum range of the lidar being used [49, 118]. ABL depth is a key variable required in microscale and mesoscale meteorological studies. The ABL depth also has a large impact on air quality. Low ABL depths trap pollutants and reduce air quality. A vertically pointing lidar can also locate clouds and determine their base altitude [118].

An example of the atmospheric science gained from simply operating vertically pointing lidar is the Lidars in Flat Terrain (LIFT) experiment [28, 29, 94]. This experiment studied the structure and evolution of the convective boundary layer over the very flat terrain of central Illinois. Scientific goals included the measurement of fluxes of heat, moisture, and momentum; vertical velocity statistics; study of entrainment and boundary layer height; and observation of organized coherent structures. The data collected was also used to evaluate the performance of these new lidars and compare measurements of velocity and boundary layer height to those obtained from nearby radar wind profilers.

Elastic backscatter lidars are also very useful from airborne platforms. By flying above the atmospheric boundary layer and looking down, one can determine the boundary layer depth along the flight line. Quite often airborne elastic lidars are used on board research aircraft to locate tropospheric and stratospheric aerosol layers above the ABL. This information can be used to redirect the aircraft into the layers for in situ sampling. The in situ data provides information on the chemical and microphysical characteristics of the aerosols in atmospheric and air quality studies.

Additional applications of elastic backscatter lidars include extracting spatial and temporal statistics of the aerosol distribution as a guide and evaluation of numerical simulations [14, 104, 150, 176]. For instance, in the spring of 2006, a field campaign designed to study the formation of atmospheric rotors was conducted in the Owens Valley of California. This experiment (named T-REX for Terrain-induced Rotors

Experiment) included two coherent Doppler lidars and the eye-safe backscatter lidar REAL of the National Center for Atmospheric Research (NCAR) operating at a wavelength of 1543 nm. At the time of this writing, the NCAR REAL is being used in the Canopy Horizontal Array Turbulence Study (CHATS) experiment. Data will be used to verify the ability of large eddy simulations to reproduce turbulence coherent structures over homogeneous forest canopies.

An advanced application of elastic backscatter lidar is a technique known as differential absorption lidar (DIAL) [18, 167]. Here, rather than using just one wavelength, two wavelengths are transmitted in an alternating sequence to determine the concentration of a gas such as water vapor [16, 19, 37, 58, 95, 174, 178] or ozone [17, 20, 128] in dependence of range and with high accuracy. One wavelength is centered in the absorption line and the other is "off-line" where the gas does not absorb. Elastic backscattering of particles is required in order to sense the small differences in backscatter intensity at those wavelengths due to the presence of the gas of interest. Elastic backscattering is also the basis for heterodyne Doppler lidars which are capable of detecting the frequency shift of the backscattered radiation [48, 57, 120, 168, 180].

Three factors influence the success of lidars: performance, required wavelength, and eye-safety. For some applications such as rapid scanning, a measure of performance is long range and high temporal resolution which is best accomplished with high laser pulse energy. This can pose an ocular hazard which limits the number of environments where the lidar can be employed. In order to ensure eye-safety with minimal sacrifice of transmit pulse energy, an operational wavelengths should be chosen that holds a higher maximum permissible exposure.

In addition to eye-safety, it is highly desirable to select a lidars operational wavelength near water vapor absorption lines in order to conduct water vapor DIAL. Water vapor is a very important atmospheric constituent—strongly influencing the atmospheric radiation budget, storm formation [12, 47, 68, 164, 165, 166, 175, 177], and atmospheric chemistry [43]. For these reasons, the development of a laser transmitter that would operate in the challenging eye-safe wavelength region around 1500 nm is desirable. However, to date, we are not aware of the development of a tunable laser transmitter in this wavelength region. Therefore, the goal of this work was to investigate a suitable laser material, which has the potential to be operated with high-average power: Cr^{4+}:YAG.

1.2 Aerosol backscatter lidar

The basis for lidar remote sensing lies in the interaction of laser radiation with gas molecules and particulate matter (aerosol particles). A schematic of an elastic backscatter lidar is illustrated in Fig. 1.1. The laser wavelength converter discussed in this dissertation is shown as part of the transmitter on the left hand side. Ideally, the transmitter emits short pulses of laser radiation (few ns to few tens of ns) with a

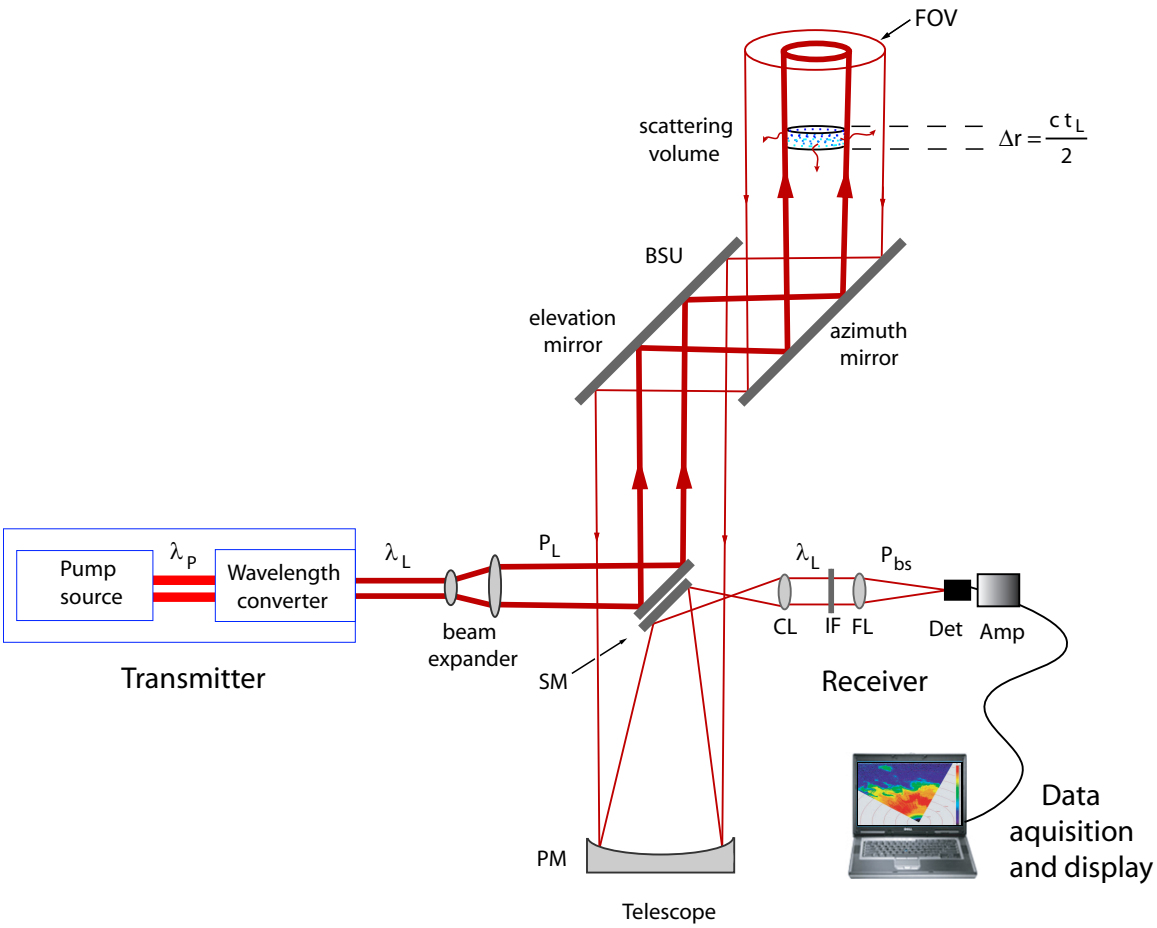

Figure 1.1: Schematic of a lidar. λ_P: pump wavelength, λ_L: (laser) wavelength of the transmitted light, P_L and P_{bs}: transmitted pulse and received backscattered power, PM and SM: primary and secondary mirror of the telescope, FOV: field of view of the receiver, BSU: beam steering unit (or scanner), CL: collimating lens, IF: interference filter, FL: focusing lens, Det: detector, Amp: amplifier.

narrow spectral width into the atmosphere. The photons are scattered and absorbed by molecules and aerosol particles. Light scattered back in the direction to the system is collected by a telescope and projected onto a detector that converts the photons into electrons. The electrical signal is amplified and digitized. In the case of elastic backscatter the wavelength remains unchanged. The backscattered radiation comes from various distances with respect to the lidar. The time delay between sending the laser pulse and receiving the backscattered photons is proportional to the distance (range) between the scatterers and the lidar as $r = ct/2$ where c is the speed of light. The factor $1/2$ appears because the pulse travels $2\,r$ for time t. In the very small amount of time (t=1 μs for 150 m range) that takes for the laser pulse to travel to the desired maximum range, the atmosphere can be regarded as "frozen" [154]. The laser beam can be pointed at various elevations and in various directions by rotating one or both mirrors of a beam-steering unit (scanner). By scanning, a ground-based lidar system can gather information about the 2- to 4-dimensional (spatial coordinates x, y, z and time t) distribution of aerosol particles in the atmosphere [40].

The range resolved backscattered radiation incident on the receiver is described by the lidar equation [80, 108, 169]. The power of the return signal is a function of the transmitted power, system geometry and efficiency, and the backscatter and transmission of the atmosphere. In case of direct detection, the lidar equation reads:

$$P_{bs}(r) = P_L \, \frac{c\,t_L}{2} \, \frac{A}{r^2} \, O(r) \, \eta \, \beta(r) \exp(-2 \int_0^{r'} \alpha(r')\, dr'). \tag{1.1}$$

Here, P_L is the transmitted average power and t_L is the pulse duration. The factor $c\,t_L/2$ is the length of the sampled volume of the atmosphere at a fixed time (see Fig. 1.1). Thus, the laser pulse length can determine the range resolution. In the case of short laser pulses on the order of a few ns, the range resolution can be limited by the bandwidth of the receiver's amplifier [103]. The temporal resolution, or the rate at which the lidar gathers information about the atmosphere, is determined by the pulse repetition frequency (PRF) of the lidar transmitter.

The amount of detected backscattered photons depends on the overlap between the laser beam and the receiver's field of view (FOV), the overlap function $O(r)$, and the area of the telescope A. The divergence of the FOV is restricted mainly by the size of the active area of the detector. If small area detectors (200 μm diameter or less) are used, a lot of effort is put towards designing a laser with low divergence (small beam propagation factor M^2, also known as "beam quality") in order to ensure full overlap $O(r) = 1$ [100]. In addition, the beam can be expanded to decrease the beam divergence. Very often the expansion of the beam is necessary in order to meet the eye-safety requirements (see Section 1.3). Using telescopes with a large primary mirror will result in more expensive system and it will give a rise of the background level in the lidar data, especially if the transmitted radiation is at wavelength of the solar spectrum.

The factor A/r^2 represents the acceptance solid angle in which scattered light is collected from distance r. Thus, the backscattered signal falls quadratically with range. This is a pure geometric factor responsible for a large dynamic range (few orders of magnitude) of the power of the return signal. As a result of the $1/r^2$ effect the backscattered radiation coming from a few-km-range is very weak when compared to backscattered signal at shorter distances. In order to create a detectable signal from a single or small number of laser pulses, high pulse energy transmitters must be used.

The efficiency of the system indicated with η in the lidar equation includes the efficiency of all optics in the path between transmitting and receiving of the laser pulses (transmission of the beam expander, focusing lenses and interference filter, reflectivity of the telescope and the BSU mirrors) and the efficiency of the detector. These are parameters that can be optimized by the instrument designer and developer.

The atmospheric factors that determine the intensity of the detected radiation are the backscatter coefficient $\beta(r)$ and the extinction coefficient $\alpha(r)$. β represents how much of the scattered light by aerosol particles and molecules per meter and solid angle ($\mathrm{m^{-1}\,sr^{-1}}$) is scattered back to the lidar. It is dependent upon the size distribution, the concentration and scattering efficiency of the particles. α ($\mathrm{m^{-1}}$) describes the lost energy due to scattering in other directions and absorption by aerosols and molecules. It accounts for absorption and scattering of the lidar beam. α and β are the sum of the corresponding coefficients for aerosols and molecules:

$$\beta(r) = \beta_a(r) + \beta_m(r) \tag{1.2}$$

and

$$\alpha(r) = \alpha_{a,sc}(r) + \alpha_{a,abs}(r) + \alpha_{m,sc}(r) + \alpha_{m,abs}(r). \tag{1.3}$$

The indices a and m stand for aerosols and molecules, and sc and abs for scattering and absorption, respectively.

Together with the elastically backscattered radiation the receiver captures background radiation. During daytime measurements this is the solar radiation and during nocturnal measurements it is the moon light and artifical light. The background radiation sets the average intensity level of the detected signal before the laser discharges. Therefore, narrow-band filters are utilized in order to suppress the background radiation. In addition, the receiver electronics are sources of high frequency noise. A measure of the performance of the lidar is the signal-to-noise ratio (SNR). High SNR means that the intensity of the backscattered radiation is much larger than the standard deviation of the background noise. Therefore, low noise detectors with high gain and amplifiers are desired. The SNR can be increased by averaging the return signal waveform over several laser pulses or by using a high-pulse energy transmitter. For real time information, the backscatter intensity can be displayed after performing background subtraction and range correction (multiplying the power of the backscattered radiation by r^2).

1.3 Eye-safety considerations and choice of operating wavelength

The lidar technique implies probing of the atmosphere with laser radiation which poses a potential eye-safety hazard. It is not convenient to use a non eye-safe lidar e.g. near airports, in field campaigns with other instruments around or in urban areas. The risk of eye injury arises in the case of scanning lidars and unattended operation, which are desirable for atmospheric research. Therefore, eye-safety is an important factor that determines the number of applications and environments in which the lidar can be used.

Ocular damage can occur at any wavelength if the energy for a given beam size and exposure time exceeds a certain limit: the maximum permissible exposure (MPE). The level of MPE depends on the spectral transmission of the eye. Fig. 1.2 presents the maximum permissible energy (MPE multiplied by the area of the beam) as a function of wavelength for single pulse and a stare, based on the American National Standard for Safe Use of Lasers [3].

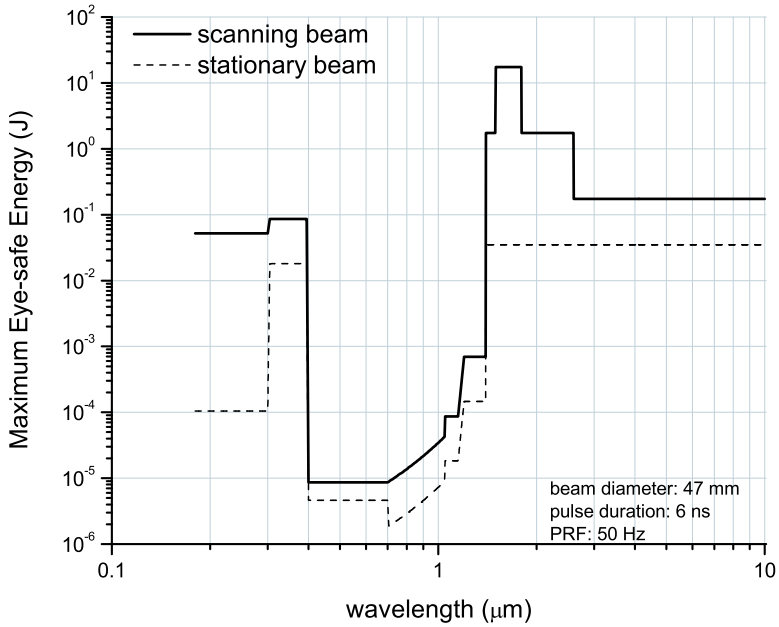

Figure 1.2: Maximum permissible energy as a function of the wavelength for a scanning and stationary beam. The laser radiation parameters are as indicated in the legend. Courtesy by S. Spuler and S. Mayor [147].

The least eye-safe spectral region in terms of permissable energy is the visible to near infrared part of the spectrum (400–1400 nm). Radiation at those wavelengths penetrates the cornea and the lens of the eye and is focused on the retina to a tiny spot on the order of 10–20 μm with high energy density. Therefore, only a small amount

of energy is enough to damage the retina. A possible solution for lidar operating at those wavelengths is to expand the beam in order to reduce the energy density below to the MPE. Another possibility is to emit low-energy pulses ($\approx \mu$J) at high PRF (at least 1 kHz). This technique, known as micropulse lidar [49, 145], requires photon-counting and averaging over many laser shots to obtain reasonable SNR. Thus micro pulse lidars are not optimal for rapid scanning.

Considerably higher energy can be safely transmitted in the UV (<400 nm) and near IR (>1400 nm). UV radiation is absorbed by the anterior parts of the eye and can cause damage to the cornea or the lens. Radiation at wavelengths between 1500 nm and 1800 nm is absorbed volumetrically in the aqueous and vitreous humor of the eye. Thus, the energy that reaches the retina is strongly attenuated and even higher energies, compared to the UV, are acceptable. Radiation at wavelengths 1400–1500 nm and beyond 1800 nm are absorbed more strongly in the anterior parts of the eye compared to wavelengths 1500–1800 nm and thus the MPE is reduced by 1 order of magnitude. For backscatter lidar applications, the near IR region has the advantage over the UV that it features low sky radiance, meaning low background radiation, and low molecular scattering, resulting in a good contrast between the backscattered radiation from aerosols and from molecules. Therefore, wavelengths greater than 1400 nm are considered for a new aerosol lidar transmitter proposed in this thesis.

In order to choose the operating wavelength one must also take into account the availability of detectors for direct detection and the transparency of the atmosphere (see Eq. 1.1). Adequate performance detectors are available in the 1400–1700-nm region. These are Indium-Gallium-Arsenate Avalanche Photo Detectors (InGaAs APD) that feature high quantum efficiency, no cooling and low cost [100]. Mayor and Spuler [103, 147, 148] have successfully demonstrated the use of InGaAs APDs in a high pulse energy, eye-safe lidar operating at 1543 nm. At wavelengths beyond 1800 nm the MPE remains modestly high but the detector performance decreases with increasing wavelength.

The choice of wavelength for an aerosol lidar transmitter is further narrowed by the transmission of the atmosphere. The absorption spectrum of air molecules and trace gases (ozone, water vapor, carbon dioxide) can be obtained from spectroscopic databases such as HITRAN [124]. Fig. 1.3 shows the composite transmission of a standard atmosphere for 1 km path length.

Strong absorption of water vapor is present at wavelengths in the spectral regions 1400–1530 nm and 1700–1800 nm. The absorption of radiation at around 1570–1600 nm is due to carbon dioxide (CO_2). Absorption lines of CO_2 are found also around 1430 nm. However, the absorption lines can be avoided by using lasers with very narrow linewidth (few 100s MHz) tuned precisely to a wavelength that is not absorbed by these species. Therefore, the spectral region around 1500 nm, which offers the maximum eye-safe energy and good performance detectors, was chosen for the development of the lidar transmitter.

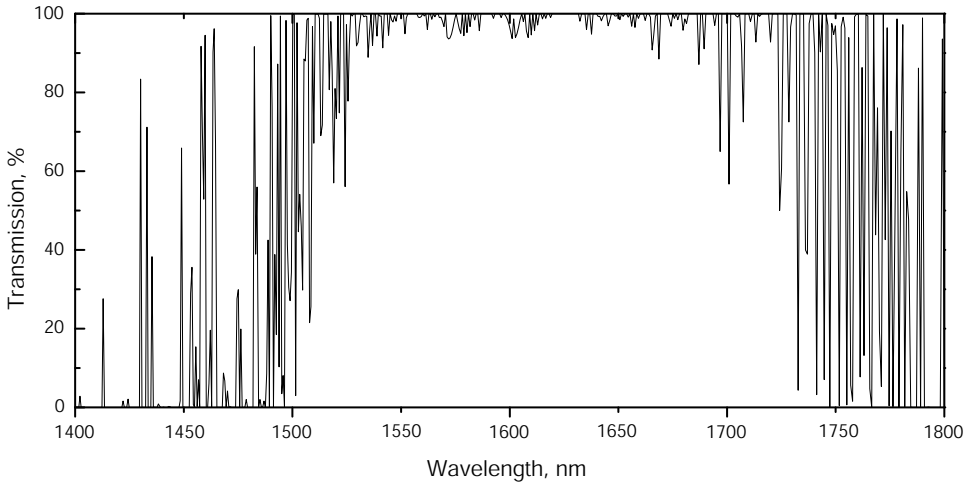

Figure 1.3: Transmission of a standard atmosphere: at sea level, air pressure of 101.325 kPa, air temperature of 296 K, water vapor partial pressure of 775 Pa. The path length is 1 km.

1.4 Wavelength converters in the eye-safe spectral region around 1500 nm.

The goal of this project is to develop an eye-safe transmitter operating at a wavelength near 1500 nm for a mobile ground-based scanning backscatter lidar. In order to enable rapid scanning with good signal-to-noise ratio and maximum range of a few kilometers the transmit pulse energy should finally be at the order of tens of mJ and pulse repetition rate of at least 10 Hz. Due to small area detectors at this wavelength region and consequently small receiver's FOV, the beam should feature low divergence (small M^2). A compact and rigid design is also desirable.

There are few possibilities to generate pulsed laser radiation around 1500 nm. They include solid-state lasers, optical parametric oscillators (OPOs) and stimulated Raman scattering (SRS).

1.4.1 Raman shifter

Stimulated Raman scattering (SRS) in solid-states (β-BBO, Nd:YVO_4) and gas (methane, deuterium) produces radiation at wavelength around 1540 nm with high conversion efficiency ($\geq$40%) and short pulse duration. Raman shifters do not require the use of high-quality pump beams to yield an efficient frequency conversion.

Murray et. al [112] have demonstrated frequency conversion of a Nd:YAG laser operating at wavelengths 1318 nm and 1338 nm to 1535 nm and 1556 nm, respectively by intracavity SRS in $Ba(NO_3)_2$ (beta-barium borate, β-BBO). They have achieved 12 mJ output pulse energy at 10 Hz and 250 mJ at 1 Hz. The beam had a near

diffraction limited profile and was better than the pump beam profile. A compact all-solid-state laser at 1525 nm by using a self-SRS in a diode pumped Q-switched Nd:YVO_4 has been reported [24, 25]. This laser delivered 0.7 mJ in 6-ns pulses at rate 20 kHz. There is no information about the beam divergence of the latter two techniques.

Raman shifting of 1064 nm to 1543 nm in methane and deuterium has been already employed in lidar systems [22, 146]. Traditionally, the main problems with this technique include poor beam quality, limited repetition rates and frequent maintenence of the Raman cell. However, these problems have been recently overcome with the aid of an advanced design by Mayor and Spuler [103, 147, 148]. In the past 2–3 years they have demonstrated high pulse energy of 350 mJ in 4-ns pulses for pulsed operation at 10 Hz to 50 Hz. By optimizing the design of the Raman cell, the pump configuration, and by utilizing injection-seeding of both the pump laser and the Raman cell, they have achieved acceptable beam divergence ($M^2 < 6$) and narrow spectral linewidth (210 MHz) of the generated radiation at 1543 nm. The reliability of the Raman shifter has been proven and successfully employed as a transmitter for a ground-based, unattended, scanning, high-power, and eye-safe backscatter lidar [162].

Despite these recent advances in SRS, Raman cells remain large and heavy and contain compressed explosive gas. Therefore, they are not well suited for airborne lidar systems. Furthermore, Raman shifters are tunable in a very narrow range ($\sim$1 nm) so that water-vapor absorption lines cannot be covered..

1.4.2 OPO

Generation of high-pulse energy radiation near 1500 nm can be obtained in optical parametric oscillators (OPOs) employing solid-state media $KTiOPO_4$ (potassium titanyl phosphate, KTP), $KTiOAsO_4$ (potassium titanyl arsenate, KTA) and $RbTiOPO_4$ (periodically poled rubidium titanyl arsenate, PP RTA). OPOs feature high-conversion efficiency ($\geq$40%), wide tunability and compact design. An important requirement for a high-performance OPO is the use of pump lasers with good beam quality operating at single frequency.

The biggest disadvantage of OPOs as lidar transmitters at this wavelength is their large beam divergence ($M^2 > 10$). Webb et. al [163] have demonstrated high average power of 33 W (330 mJ in 20-ns pulses at 100 Hz repetition rate) at 1570 nm with a KTA OPO. However, the beam had M^2 of 30. A few eye-safe lidars employing OPOs have shown poor performance due to large beam divergence [53, 126, 122].

Recently, several techniques for improving the "beam quality" of OPOs have been demonstrated in a different spectral region. They include injection-seeding [99], gain guiding [4], OPO/OPA configuration [5]. For OPOs at 1560–1570 nm, improvement of the M^2 has been demonstrated with PP RTA crystal by using confocal unstable resonator [51] and with KTP in a noncritically phase matching configuration [42].

Soon after starting this project, a very promising technique for decreasing the beam divergence at high energy was reported by Smith and Armstrong [6, 7, 142]. They have used an image-rotating cavity (rotated image singly-resonant twisted rectangle, RISTRA OPO). By implementing the RISTRA configuration for KTA they have achieved $M^2 \sim 4$ for 170 mJ pulse energy at 10 Hz at wavelength 1550 nm. Deep theoretical and experimental knowledge in OPO design and operation, which is only available at a few institutes, is essential for developing a suitable high-power OPO system successfully.

1.4.3 Solid-state lasers

Solid-state lasers with an emission band near 1500 nm include Er:glass and Cr^{4+}:YAG. Both are low gain materials with conversion efficiency in pulsed regime from a few % to ∼12 %. However, a solid-state laser has the advantage over nonlinear wavelength converters, Raman shifters and OPOs, that its beam quality can be better controlled by a suitable resonator configuration.

Er,Yb:phosphate glass is transversely pumped either by flash-lamps [105, 119, 155] or laser diodes [52, 183] at wavelength near 1000 nm. Thus, it features a rugged and compact design. Tunability in the wavelength region 1528–1558 nm has been demonstrated [105]. Multimode Q-switched operation at moderate output energy of 45 mJ at 1 Hz repetition rate [45] and higher PRF of 50 Hz with lower output energy of 10 mJ [172] have been reported. Diode-pumped Q-switched Er,Yb:phosphate glass laser operating at single transversal and single longitudinal mode has been developed for use in coherent Doppler lidar [183]. This laser delivered 11 mJ output energy, corresponding to ≈1% conversion efficiency, with 15 Hz PRF and relatively long pulse width of 230 ns. The laser was frequency stabilized and had M^2 of 1.4. The low efficiency of Q-switched Er:glass is attributed to their small emission-cross section and low thermal conductivity.

Cr^{4+}:YAG can be pumped longitudinally by an Nd:YAG laser at the fundamental wavelength 1064 nm [87, 113], InGaAs laser diode at around 970 nm [1, 143], and Yb-doped fiber laser at 1064 nm [89]. Cr^{4+}:YAG laser is tunable between 1340 nm and 1550 nm [1, 15, 38, 85]. Short laser pulses on the order of a few 10s of ns can be produced when the crystal is operated in a gain switched regime [38, 101]. A maximum conversion efficiency of 16.4 %, resulting in 11 mJ output energy, at 1 Hz has been demonstrated by Mathieu et. al [101]. Output energy of ≈5 mJ [15] and ≈10 mJ [101] have been reported for 12.5 Hz and 30 Hz PRF, respectively. The decreased output energy at higher PRF was attributed to the use of non optimal cooling arrangement [101]. The extraction efficiency of Cr^{4+}:YAG is limited by the existence of absorption saturation of the pump energy and excited-state absorption of both pump and emission radiation [38, 39, 101, 113]. The mode structure and beam divergence have not been discussed in the literature. However, from the employed resonator configurations one can conclude that the lasers must have operated in a

multimode regime. Gain-switched Cr^{4+}:YAG laser operation at a kHz PRF (90 μJ at 1 kHz and 55 μJ and 5 kHz in 4-ns pulses) has been reported by [101].

1.5 The goal of this project

Based on the requirements for high-performance scanning aerosol backscatter lidar (see Section 1.4), and the actual knowledge of the possible transmitters at the time this project was initiated, the development of Cr^{4+}:YAG laser was chosen. It was planned to be pumped by a novel diode-pumped Nd:YAG laser, operating at 250 Hz. An all solid-state transmitter features rugged, compact and low maintenance design which makes it suitable also for an airborne platform. Moreover, Cr^{4+}:YAG is widely tunable in the range ~1400–1500 nm and thus posses the potential for measuring water vapor absorption with the DIAL technique.

The specifications of the pump laser, the desired parameters for the wavelength converter and their importance for the lidar system are summarized in Tab. 1.1.

Table 1.1: Desired specifications of the new lidar transmitter

parameter	Nd:YAG pump laser	Cr^{4+}:YAG wavelength converter	feature
wavelength, nm	1064	1400–1500	eye-safe, possible water vapor DIAL
pulse energy, mJ	200	20–40	sufficient SNR and range, scanning
pulse length, ns	20	<100	range resolution <15 m
pulse repetition frequency, Hz	250	250	high temporal resolution, rapid scanning
beam propagation parameter, M^2	<2	<3	full overlap with the receiver's FOV

Tunability of Cr^{4+}:YAG over water vapor absorption lines near 1460 nm and 1500 nm (see Tab. A.1) should be also demonstrated.

Chapter 2

Laser theory

The word LASER is an acronym for Light Amplification by Stimulated Emission of Radiation, although today it is commonly used as a noun, laser, rather than as an acronym. The basic elements of a laser device, are as shown in Fig. 2.1.

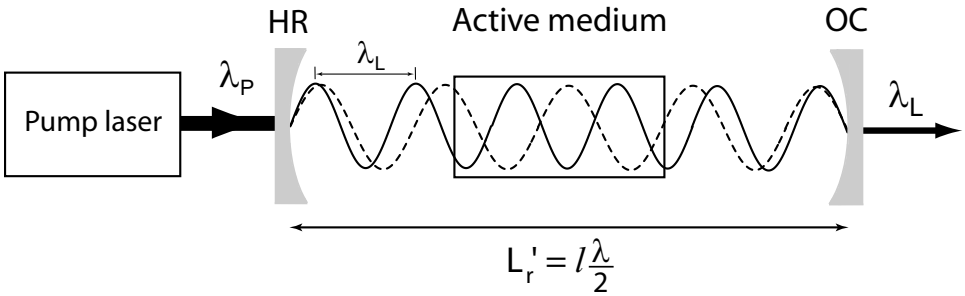

Figure 2.1: Principle of a laser. This example uses a pump laser as a source of pump radiation at wavelength λ_P. The wavelength converter includes the active medium and the resonator. The resonator mirrors are HR: mirror with high-reflectivity coating and OC: output coupler with partial transmission for the laser wavelength λ_L. L'_r is the optical length of the resonator that determines the resonant frequencies.

(i) laser gain medium with active atoms (or molecules or ions), (ii) appropriate pumping source of optical radiation (i.e laser, laser diodes, or flash-lamps) to excite these atoms to higher energy levels and (iii) a resonator (often called cavity) to provide optical feedback. The most commonly used resonator configuration, the linear resonator as illustrated in Fig. 2.1, consists of two mirrors: one with high reflectivity at the laser wavelength (HR) and another with partial reflectivity, through which the laser beam can exit the resonator, and therefore called output coupler (OC).

As a result of the pumping process inversion population between two excited levels of the active medium is obtained. Electromagnetic radiation can thus occur at frequencies within the gain bandwidth. The generated light in the resonator is reflecting back and forth repeatedly and is amplified during each transit through the

gain medium. However, the existing radiation also experiences losses from the mirrors and only some electric fields will survive. They satisfy certain eigen equations. There solutions are therefore called eigenmodes (or just modes). The cavity modes are field distributions which reproduce themselves after one cavity round trip. The particular field configuration is known as a transverse mode. Each transverse mode occur at certain discrete wavelengths (or frequencies) over the gain bandwidth, at which the electric field has integral multiple of half-wavelengths with zero magnitude at the resonator mirror surfaces. This condition establishes standing waves, referred to as longitudinal modes. In Fig. 2.1 are illustrated two resonant longitudinal modes.

In the first section of this chapter the rate equation approach is introduced in order to describe the dynamics in the laser material and to obtain expressions for the output laser parameters, such as output energy and pulse duration. Next, the formulas for calculating the cavity modes and their propagation are presented. It is followed by description of the pump induced thermal lensing in the active medium, which affects the cavity mode propagation and consequently the stability of the resonator. A method for the design of a stable resonator with large mode size is presented in the last section.

2.1 Laser dynamics

The dynamic behavior of radiation in a laser can be described by analyzing the interaction between the photons in the cavity modes and the atoms of the laser material. In a real laser system a large number N of resonant modes are present and each one is able to interact with the atoms in the cavity volume. This results in a complicated system of N coupled nonlinear differential rate equations for the photon density together with atomic rate equations for the population density of the laser levels. However, the laser dynamics can be well described even after performing some major simplifications [134], which are outlined below.

The N cavity rate equations can be represented by just one equation for a single laser mode, tuned at the central wavelength. In this case the spectral dependency of the transition cross-sections in the laser material, generally weak, and the losses in the cavity are neglected. The photon density in the mode is then $\phi_L = \sum_N \phi_N$. The atomic rate equations can also take a simple form by assuming that the relaxation decay times of most laser levels are sufficiently fast so that these levels are essentially not populated.

The rate equation approach, even with the complete set of (N+) equations, has some limitations concerning spatial interference between cavity modes which can cause spatially inhomogeneous effects in the population of the laser levels, such as saturation or "spatial hole burning" [135, 136]. Nonetheless, they are very useful for the calculation of several main parameters regarding the laser performance, such as buildup time, output energy, and pulse duration.

The form of the rate equations depends on the exact atomic system of particular interest. Here, a four-level system is considered with laser transition between excited levels $|2\rangle$ and $|1\rangle$. In addition, it is accounted for excited state absorption (ESA) of both pump and laser wavelength from the upper laser level to higher lying excited levels. Generally, one has to take into account the interplay of populations of all levels. However, the relaxation transition from all excited energy levels, except the upper laser level, occur very rapidly (decay time $\sim$ few 10's of ps) and thus their population is negligible ($n_j \approx 0,\ j = 1, 3, 4, 5$). As a result, the total number density of the active ions n_T is expressed by the sum of the population of the ground state n_0 and the upper laser level n_2 at each moment: $n_T = n_0(t) + n_2(t)$. Since the terminal laser level remains relatively depopulated the inversion population becomes $\Delta n(t) = n_2(t) - n_1(t) \approx n_2(t)$. Under these assumptions the system describing the laser dynamics reduces to two coupled rate equations for the time rate of change of the inversion population (Eq. 2.1) and the laser intensity (Eq. 2.2). Due to ESA of the pump wavelength, which affects the pumping efficiency, the third equation for the pump intensity must be added (Eq. 2.3) [15]

$$\frac{d\,n_2}{d\,t} = \sigma_{GSA}\,\frac{I_P}{h\nu_P}\,n_0 - \sigma_{SE}\,\frac{I_L}{h\nu_L}\,n_2 - \frac{n_2}{\tau_2} \tag{2.1}$$

$$\frac{\partial\,I_L}{\partial\,z} + \frac{1}{c}\frac{\partial\,I_L}{\partial\,t} = \frac{2\,l_{cr}}{c\,\tau_r}(\sigma_{SE} - \sigma_{ESA_L})\,n_2\,I_L - \frac{I_L}{\tau_c} \tag{2.2}$$

$$\frac{\partial\,I_P}{\partial\,z} + \frac{1}{c}\frac{\partial\,I_P}{\partial\,t} = -(\sigma_{GSA}\,n_0 + \sigma_{ESA_P}\,n_2)\,I_P. \tag{2.3}$$

The subscript $_P$ stands for the pump wavelength and $_L$ for the generated laser wavelength. The pump photon energy is $h\,\nu_P$ ($h = 6.626 \times 10^{-34}\,\mathrm{J \cdot s}$ is Planck's constant and $\nu_P = c/\lambda_P$ is the pump frequency, $c = 3 \times 10^{-8}\,\mathrm{m/s}$ is the speed of light, and λ_P is the pump wavelength), and analogous for the laser photon energy. The intensity is $I = h\nu\,\phi\,c$ with ϕ being the number of photons per unit volume. σ_{GSA} and σ_{SE} are the ground-state absorption and stimulated emission cross-sections, respectively. The excited cross-section is denoted by σ_{ESA}. τ_2 is the fluorescence lifetime of the upper laser level ($\tau_2 \sim$ few μs).

The round-trip time τ_r, which appears in Eq. 2.2, is related to the optical length of the cavity L_r' in the form $\tau_r = 2L_r'/c$. Thus, the ratio $2l_{cr}/(c\tau_r) = l_{cr}/L_r'$ with l_{cr} being the length of the crystal, implies that only a fraction of the light is being amplified. The photon lifetime in the cavity τ_c is expressed as the fractional power loss per round-trip:

$$\tau_c = \tau_r \left[\mathcal{L} + \ln\left(\frac{1}{\mathcal{R}_2}\right)\right]^{-1}, \tag{2.4}$$

with

$$\mathcal{L} \equiv 2\,l_{cr}\kappa_{cr} + \ln\left(\frac{1}{\mathcal{R}_1 \cdot \prod_i T_i^2}\right). \tag{2.5}$$

The first term in $\mathcal{L}$ represents the dissipative optical loss in the crystal with linear loss coefficient κ_{cr}. The second term summarizes the miscellaneous losses in the cavity (absorption, scattering and diffraction) as leakage of the optics in the resonator. $\mathcal{R}_1$ is the reflectivity of the rear mirror and T_i is transmission of the i-th element in the resonator. $\mathcal{L}$ is typically 2–10 %. $\ln(1/\mathcal{R}_2)$ is the "useful" loss due to the partial reflectivity of the output coupler.

At this point, the particular pumping regime has to be considered. The laser material is pumped with a short pulse ($t_p \sim$10 ns) so that the inversion population and the gain quickly reach a value above threshold before the laser oscillation has time to build up from the initial noise level in the resonator. The laser pulse develops after the pump pulse is complete. The build-up time is about few 100's of ns and the pulse duration is in the order of few 10's of ns, depending on the resonator configuration. This regime is known as "gain switching" and can be described in a similar way as Q-switching.

The rate equations are further simplified by the fact that no relaxation of the upper laser level occurs due to the long lifetime compared to the pump pulse. Moreover, during the pumping interval no laser oscillations are present in the cavity. Consequently, the pump pulse is over while the laser pulse is developing. As a result, the coupled equations can be solved analytically [33].

When the interaction time of the pump light with the crystal is small compared to the fluorescence lifetime ($t_p \ll \tau_2$) it is convienient to work with a pump energy fluence defined as [8, 114]

$$U_P(z) = \int_0^{t_p} I_P(t,z)\, dt. \tag{2.6}$$

The solution of Eq. 2.1 thus reads

$$n_i(z) = n_T\left[1 - \exp\left(-\frac{\sigma_{GSA}\, U_P(z)}{h\nu_P}\right)\right] \tag{2.7}$$

As it will be shown next, the rate equations are solved for the averaged values of n_2 and I_L over the length of the laser crystal. The average initial inversion population is defined as

$$n_i = \frac{1}{l_{cr}} \int_0^{l_{cr}} n_i(z)\, dz, \tag{2.8}$$

which is γ times above the threshold n_t. γ is called inversion ratio $\gamma = n_i/n_t$. The threshold inversion population required to achieve oscillations can be estimated from the emission and ESA cross-sections together with parameters of the laser cavity

$$n_t = \frac{1}{2\, l_{cr}(\sigma_{SE} - \sigma_{ESA_L})}\left[\mathcal{L} + \ln\left(\frac{1}{\mathcal{R}_2}\right)\right]. \tag{2.9}$$

At the end of the laser pulse the inversion population is reduced to a value n_f below n_t. The relation between the initial and final population densities is given by the equation

$$1 - \frac{n_f}{n_i} + \frac{1}{\gamma} \ln\left(\frac{n_f}{n_i}\right) = 0 \,, \tag{2.10}$$

which must be solved numerically.

With the aid of the above defined parameters, one can determine the laser build-up time t_b, the output energy E_{out}, and the laser pulse duration t_L. The formula for the build-up time has the form

$$t_b = \frac{\tau_c}{\gamma - 1} \cdot \ln\left(\frac{I_{ss}}{I_0}\right). \tag{2.11}$$

Here, I_0 represents the initial spontaneous-emission noise excitation of the cavity mode and I_{ss} is the final intensity level at the moment when steady-state would be reached if the laser was cw pumped at a pumping rate γ times above threshold.

The total output energy can be expressed as [15]

$$E_{out} = h\,\nu_L \left(1 - \frac{\sigma_{ESA_L}}{\sigma_{SE}}\right)(n_i - n_f)\, V_L \cdot \frac{\ln(1/\mathcal{R}_2)}{\mathcal{L} + \ln(1/\mathcal{R}_2)} \,, \tag{2.12}$$

where $V_L = \pi\,\omega_L^2\, l_{cr}$ is the volume of the laser mode with mode radius ω_L in the crystal.

From Eqs. 2.9 and 2.12 it is clear that the ESA of the laser wavelength causes an increase of the threshold and a decrease in the output energy. Also, the miscellaneous losses must be minimized by using high quality optics and, if possible, less intracavity elements. The output energy is proportional to the difference between initial and final inversion population. Investigation of Eq. 2.10 shows that the final inversion population decreases rapidly when $\gamma > 1.1$. Thus $(n_i - n_f)$ increases as γ increases, which can be accomplished by applying higher pump energy densities. Of course, the damage threshold of the optical components must be considered. Another factor, influencing the output energy, is the mode volume in the crystal. It can be adjusted by using a suitable resonator configuration (see Section 2.5).

The pulse duration can be calculated as the ratio of the output energy to the maximum peak power P_{max}

$$t_L = \frac{E_{out}}{P_{max}} = (n_i - n_f) \cdot \frac{\tau_c}{n_t\,(\gamma - 1 - \ln\gamma)}. \tag{2.13}$$

According to Eq. 2.12 the theoretical limit of the conversion efficiency η can be estimated as

$$\eta = \frac{\nu_L}{\nu_P}\left(1 - \frac{\sigma_{ESA_L}}{\sigma_{SE}}\right). \tag{2.14}$$

In addition, the pumping efficiency η_P , defined as the number of ions pumped in the upper laser level per pump photon, is reduced due to ESA. Therefore, the theoretical conversion efficiency should be corrected with the factor [101]

$$\eta_P = \frac{n_i \, l_{cr} \, h\nu_P}{U_P}. \tag{2.15}$$

In practice, lower conversion efficiency is realized due to passive losses in the cavity. Some interactions between the active atoms and surrounding atoms in the lattice can also contribute to reduction of the laser efficiency [113].

2.2 Laser resonator modes

In practice, two types of resonator modes must be distinguished: longitudinal and transverse. The longitudinal modes differ from one another in their oscillation frequency, whereas the transverse in both frequency and intensity distribution in the plane perpendicular to the propagation direction. This means that several longitudinal modes can have the same field distribution, corresponding to a given transverse mode. The resonator modes are denoted by $\mathrm{TEM_{mnl}}$ ("transverse electro-magnetic wave") where the first two indeces identify the order of the transverse mode (in x– and y– direction), and l stands for the number of longitudinal modes.

2.2.1 Transverse modes

The expression for the spatial-dependant mode is obtained by utilizing the Maxwell equations and deriving the scalar wave equation for laser radiation propagating in free space in direction z [137]

$$[\nabla^2 + k^2] \, u(x, y, z) = 0. \tag{2.16}$$

Here ∇^2 is the Laplacian operator, $k = 2\pi/\lambda$ is the propagation constant and u is a component of the electric field. The solution of Eq. 2.16 can be written as

$$u(x, y, z) = \psi(x, y, z) \, e^{-ikz} \, , \tag{2.17}$$

where the spatial function $\psi(x, y, z)$ describes the transverse intensity distribution, and e^{-ikz} is the free-space phase factor with spatial period of one wavelength λ in direction z [78]. For almost all laser amplification and laser propagation problems of practical interest, the paraxial approximation holds [138]. It basically shows that the z dependence of $\psi(x, y, z)$ is slow and therefore the second derivative $\partial^2 \, \psi(x, y, z)/\partial z^2$ can be neglected in the wave equation Eq. 2.16.

The transverse resonator modes of order mn are obtained after substituting Eq. 2.17 in Eq. 2.16 in paraxial approximation

$$u(x, y, z) = \frac{\omega_0}{\omega} \, H_m\left(\sqrt{2}\frac{x}{\omega}\right) H_n\left(\sqrt{2}\frac{y}{\omega}\right) \exp\left\{-i\left[kz - \Phi_{mn} + \frac{k}{2q} \, r^2\right]\right\}. \tag{2.18}$$

The real part of Eq. 2.18 represents the electric field E, which in general is a superposition of several cavity modes of different order. H_m and H_n are the Hermite polynomials of order m and n, respectively, with integers $m, n \geq 0$ corresponding to the order of the transverse mode. The intensity distribution of such a mode has m nodes in x–direction and n nodes in y–direction. $\Phi_{mn}(z)$ is the phase shift, which the laser mode of order mn experiences after distance z. The expression for $\Phi_{mn}(z)$ is given later in this section. $r = \sqrt{x^2 + y^2}$ and q is the complex beam parameter, defined as

$$\frac{1}{q} = \frac{1}{R(z)} - i\frac{\lambda}{\pi\,\omega(z)^2}. \tag{2.19}$$

Here, $R(z)$ is the radius of curvature of the wavefront at distance z. $w(z)$ is the beam radius (also called beam spot and beam size) at distance z. The physical meaning and the propagation variation of R and w are defined for the lowest order transverse mode (m, $n = 0$) in Section 2.2.3. More general definitions are provided in Section 2.6.

2.2.2 Longitudinal modes

The transverse modes can oscillate at such frequencies for which the electric field within the resonator experiences constructive interference after one roundtrip. The number of resonator modes can be calculated by utilizing Eq. 2.18 for optical length $2L_r'$ of one roundtrip

$$2k\,L_r' - \Phi_{mn}(L_r') = 2\pi(l+1) \quad \text{, with} \quad l \geq 0. \tag{2.20}$$

with the Gouy phase shift for one roundtrip ($z = 2L_r'$) [139]

$$\Phi_{mn}(L_r') = (m+n+1)\arctan\left(\frac{2L_r'}{z_R}\right). \tag{2.21}$$

z_R is called Rayleigh range and is defined as the distance from the waist location at which the beam waist increases $\sqrt{2}$ times. Eq. 2.21 shows that different order transverse modes will experience different phase shift and therefore Eq. 2.20 will be satisfied for different number l of longitudinal modes (frequencies).

The oscillation frequency ν_l and the frequency spacing $\Delta\nu_l$ of the longitudinal modes can be obtained from Eq. 2.20:

$$\nu_l = l\,\frac{c}{2L_r'} \tag{2.22}$$

and

$$\Delta\nu_l = \frac{c}{2L_r'}. \tag{2.23}$$

2.2.3 Characteristics of the fundamental mode TEM_{00}

The above equations will now be applied for the fundamental mode TEM_{00}.

After inserting Eq. 2.19 in the Eq. 2.18 for m, $n = 0$ ($H_0 = 1$) the expression for TEM_{00} reads

$$u(x, y, z) = \frac{\omega_0}{\omega} \exp\left\{-\frac{r^2}{\omega^2}\right\} \exp\left\{-i\left[kz - \Phi_{00} + \frac{k}{2R} r^2\right]\right\}. \tag{2.24}$$

One sees, that TEM_{00} mode has Gaussian energy distribution with maximum amplitude at the axis (Fig. 2.2). The beam radius $\omega(z)$ is defined as the radial distance at which the field amplitude drops to $1/e$ of its maximum value or speaking in terms of intensity, $I = |E|^2$, at level $1/e^2$. The right panel of Fig. 2.2 shows the caustic $\omega(z)$

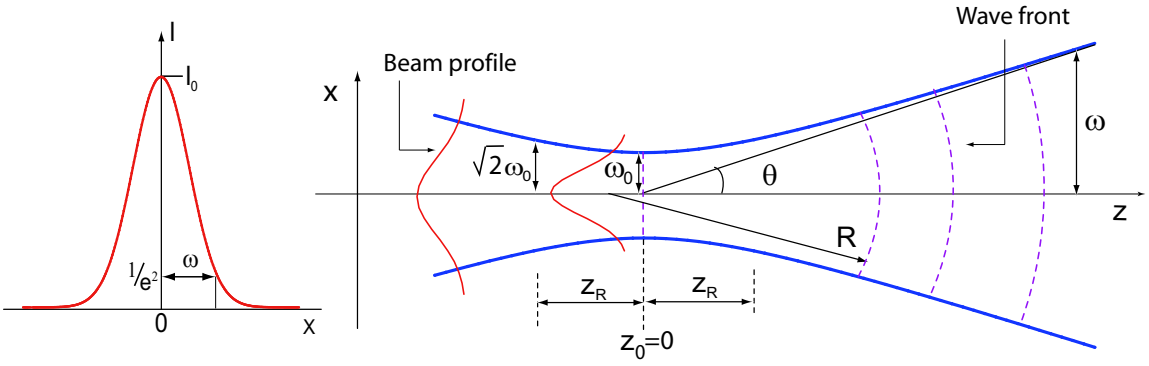

Figure 2.2: Gaussian beam. Left panel: Radial intensity distribution. Right panel: beam propagation caustic.

and the variation of the wavefront of the beam, propagating in direction z, according to the equations below

$$\omega(z) = \omega_0 \left[1 + \left(\frac{z}{z_R}\right)^2\right]^{1/2} \tag{2.25}$$

$$R(z) = z\left[1 + \left(\frac{z_R}{z}\right)^2\right]. \tag{2.26}$$

The beam profile remains Gaussian as the beam propagates along its axes and only the beam width changes. The smallest beam radius is ω_0 at position $z_0 = 0$ and therefore called beam waist. From Eq. 2.26 follows that the phase front at the waist is plane ($R(z_0) \to \infty$). The Rayleigh range $z_R = \pi\omega_0^2/\lambda$. For large z the beam radius changes linear with the distance

$$\omega \approx \frac{\omega_0}{z_R} z. \tag{2.27}$$

Using the latter equation the half angle divergence of the beam can be defined as

$$\theta = \frac{\omega}{z} = \frac{\lambda}{\pi\omega_0}. \tag{2.28}$$

If the waist is known the divergence of the beam can be calculated. From Eq. 2.28 it follows that the product of the divergence and the beam waist size is invariant to beam propagation. This constant is called beam parameter product $\mathcal{K}$.

$$\mathcal{K} = \theta\,\omega_0 = \frac{\lambda}{\pi}. \tag{2.29}$$

It is worth to point out some important properties of the fundamental mode TEM_{00}. As it can be seen from Eq. 2.18, TEM_{00} is the only mode with symmetric energy distribution without nodes in the radial cross section. This provides optimal amplification of the beam by passing through the gain medium. Also, TEM_{00} occupies the smallest mode area and smallest divergence (see Section 2.6) and thus experiences minimal losses within the cavity. Furthermore, according to Eq. 2.20, the number of resonant frequencies for TEM_{00} is minimal, compared to other modes. These properties are desirable preconditions for stable laser operation with narrow linewidth.

For some applications, such as water vapor DIAL, Doppler, and high spectral resolution lidar, laser operation at single longitudinal mode (SLM) is required. Usually additional techniques are employed to achieve this regime. Mode selection can be accomplished by insertion of an aperture in the cavity. Its size matches the TEM_{00} mode size and introduces high diffraction losses for all other modes [72]. In addition, TEM_{00} can be forced to oscillate at single frequency by using a ring-resonator design with intracavity etalon and injection-seeding [73].

For other applications, such as aerosol backscatter lidar, the demand of TEM_{00} operation is not so strong as long as the divergence of the beam allows full overlap with the field of view of the detector for a reasonable size expanded beam (see Section 1.2). Multiple-transverse-mode operation may be chosen, in order to extract more energy (due to larger mode size in the active medium Eq. 2.12), especially when low gain material is employed.

2.3 Beam propagation of laser modes

The damage threshold of the optical components within the cavity should be taken in consideration when designing the resonator. This is done by calculating the energy density at each optical surface by propagating the eigenmodes.

The laws governing the propagation of laser beams can be formulated in terms of the complex parameter q by utilizing the matrix formalism [76, 77]. If the beam parameter at the input of an optical system is known,the exit beam is transformed

according to

$$q_2 = \frac{Aq_1 + B}{Cq_1 + D}. \tag{2.30}$$

Here A, B, C and D are the elements of the ray transfer matrix M, representing the entire optical system. M is a product of the matrices representing each optical component of the system. The matrices of some fundamental components are given in Appendix B. The ray matrix determinant of any basic element satisfies the following relation

$$AD - BC = 1. \tag{2.31}$$

The transformation law can now be applied to the resonator modes. A mode, starting at a given reference plane is self-consistent after one roundtrip, in other words $q_1 = q_2 = q$ and M is the matrix for the roundtrip. From Eq. 2.30 follows a quadratic equation for the beam parameter q. The solution of this equation after applying Eq. 2.31 is

$$\frac{1}{q} = \frac{D - A}{2B} \pm i\frac{\sqrt{4 - (A + D)^2}}{2B}, \tag{2.32}$$

which yields (according to Eq. 2.19) the corresponding beam size ω and radius of the phase-front curvature R at the reference plane. The sign in front of the square root is chosen so that it provides real solutions for ω, namely $\omega^2 \geq 0$. If only imaginary solutions exist, the resonator is unstable.

In order to determine the resonator modes, the beam waist in the resonator and the Gouy phase shift must be found (Eq. 2.18). From Eq. 2.25 and Eq. 2.26 ω_0 and its location z_0 can be expressed in terms of ω and R

$$\omega_0 = \omega\left[1 + \left(\frac{\pi\omega^2}{\lambda R}\right)^2\right]^{-1/2}, \tag{2.33}$$

$$z_0 = R\left[1 + \left(\frac{\lambda R}{\pi\omega^2}\right)^2\right]^{-1}. \tag{2.34}$$

The Gouy phase shift can be also expressed in terms of the ray matrix elements.

$$\Phi_{mn}(L_r') = \pm(m + n + 1)\arccos\left(\frac{A + D}{2}\right). \tag{2.35}$$

The calculations of a stable linear resonator in this thesis are based on the formulas, presented in this section.

2.4 Thermal lensing of the laser crystal

Due to absorption of the optical pump radiation, heat is generated in the laser crystal [74]. The main reasons are as follows: (i) The energy difference of the photons between the pump and the upper laser level, as well as between the lower laser level and the ground state, is lost as heat in the host lattice. In the presence of ESA, additional non radiative transitions of the active ions from higher lying energy levels take place. (ii) The quantum efficiency of the fluorescence, defined as the ratio of the radiative rate to the total (radiative plus non radiative) fluorescence rate, is less than one.

The heat in the cylindrical rod is removed mainly through the wall which is in contact with a highly conductive metal heat sink. In addition, active cooling techniques of the heat sink are employed. The amount of heat, transfered from the end surfaces to the surrounding air due to conduction is negligible and only the generation of radial temperature gradient is considered. The temperature radial field established in the rod can be obtained by solving the heat-conduction equation [151]

$$\rho_{cr} c_p \frac{dT}{dt} = k_{cr}(T)\left[\frac{d^2T}{dr^2} + \frac{dT}{rdr}\right] + Q(r,t). \tag{2.36}$$

Here, ρ_{cr} is the rod density, c_p is the specific heat, k_{cr} is the rod thermal conductivity and Q is the heat source describing the absorbed pump energy density converted to heat. The distance from the center of the rod is r. Studies have shown that in repetitively pulsed-pumped systems a quasi-thermal steady-state will be reached for repetition rates in the order of 10 Hz [61, 151]. Therefore, $dT/dt = 0$. Furthermore, homogeneous pumping of the crystal is assumed (Q=const) and the temperature dependence of the thermal conductivity is neglected (k_{cr}=const) [30]. Under these conditions, Eq. 2.36 yields a parabolic temperature profile with the highest temperature at the center of the crystal [71].

The thermal gradient and the resulting stresses in the crystal cause spatial variation of the crystal's refractive index. According to [70, 71], the refractive index is a parabolic function with the radius of the rod, represented with the formula 2.37

$$n(r) = n_{cr,0} - c_1 \eta_h P_p = n_{cr,0}\left(1 - \frac{2}{b^2} r^2\right), \tag{2.37}$$

where $n_{cr,0}$ is the refractive index of the laser material in the center. c_1 represents the combined temperature and stress dependent radial changes of the refractive index. η_h is the fraction of the average pump power P_p which is dissipated as heat in the crystal. b is a constant, turning positive once thermal equilibrium is reached [61]. b contains both the thermal expansion coefficient and the average photoelastic coefficient. The amount of change in the index of refraction is proportional to the average incident power on the crystal. In addition, the temperature variation across the rod causes

thermal deformation of the end faces of the crystal. Thermal expansion of the material leads to bulging of the end faces [71].

Under optical pumping the laser material acts like a thick lens. The focal length of a lens-like medium f_T has been determined by [71, 76] as

$$f_T \simeq \frac{1}{c_2 \eta_h P_p} \simeq \frac{b^2}{4\, n_{cr}\, l_{cr}}, \tag{2.38}$$

where c_2 represents the contribution of the temperature and stress dependent changes of the refractive index and the distortion caused by end face curvature of the rod. Equation 2.38 shows that for η_h=const the induced thermal focusing power $1/f_T$ is proportional to the average pump power. The principal planes are inside the rod at distance h_{sag} ("sag" stands for sagittal plane) from the ends of the crystal

$$h_{sag} \simeq \frac{l_{cr}}{2\, n_{cr}}. \tag{2.39}$$

For Brewster geometry a correction factor must be added and the expression for the tangential plane becomes [60, 123]

$$h_{tan} \simeq \frac{l_{cr}}{2\, n_{cr}^3}. \tag{2.40}$$

The ratio of the sagittal and tangential focal lengths can be obtained, in first approximation, from the ray transfer matrices for tilted thin lens in Brewster angle θ_B [60]

$$\frac{f_{sag}}{f_{tan}} = \frac{1}{cos^2 \theta_B}. \tag{2.41}$$

These approximations are valid only if the focal length is very long compared to the rod length, which is fulfilled for the pump power levels used in this study. For the design of a stable optical resonator operating at the fundamental TEM_{00} mode, measurement of the thermal focal length is required.

More comprehensive treatment of the conduction equation has been done recently by [160]. In this study, temperature and spatial dependencies of the thermal conductivity are taken into account. The pump beam profile is considered and the fraction of the absorbed pump energy converted to heat is estimated. These extended analysis yield different shape of the temperature field compared to [71]. As a consequence, the value of the thermal lens focal length differs from the solutions in [64].

However, the common approximation described above is sufficient for the calculation of a stable resonator [173].

2.5 Design of a dynamically stable linear resonator

For this project, the resonator design goal is based on the desirability for high output pulse energy, operation in the fundamental mode with high energy and pointing

stability, and a mechanically rigid setup.

These requirements can be fulfilled with a well engineered stable resonator. In the case of a low gain solid-state laser material, a linear configuration must be chosen, to ensure multiple transits of the generated light through the laser medium before exiting the cavity. By doing so, multiple amplifications are achieved (see Fig. 2.1).

In stable resonators, operation of the fundamental mode is achieved by inserting a mode-selective aperture in the cavity. The mode cross-sectional area is kept small and therefore energy is extracted only from a small volume of the active medium. The efficiency of the laser can be increased by adapting the mode diameter to the diameter of the rod, which becomes the limiting aperture itself. In this case, the resonator becomes more sensitive to misalignment of the cavity mirrors. In addition, the fundamental mode is perturbed by variations of the pump-induced thermal lensing in the laser rod, especially during pump pulsed operation. A design procedure for a stable resonator with large fundamental mode size, which is stationary with respect to thermal-focal length fluctuations, has been described in [93, 96, 97, 98, 116]. Such a configuration is known as a dynamically stable resonator and is experimentally verified for pulsed Nd:YAG laser in [93, 116]. Moreover, the mechanical stability of the system to cavity mirror misalignment is treated in details in number of papers [32, 54, 96, 97, 98].

Here, the formulation for the general case of dynamically stable resonator, incorporating an arbitrary number of intracavity elements, with considered misalignment sensitivity is summarized according to [97, 98]. This method can be applied directly to calculate resonator configurations with several laser rods. Multirod resonators are used in order to achieve higher output energy without distorting the beam profile and propagation factor [36, 116].

2.5.1 Dynamical stability

This method is based on the matrix formalism presented in Section 2.3. The resonator modes are treated as Gaussian beams and the optical elements are represented by their ray-transfer matrices. The laser material is viewed as a thin lens with thermal focal length f_T and the distances are measured with respect to the principal planes of the laser rod.

The mode size and the condition for dynamical stability can be expressed after defining some ray-transfer matrices, as illustrated on Fig. 2.3, and variables.
The reference planes 1 and 2 are set on the reflective surface of the resonator mirrors and 3 is at the thermal lens. The transfer matrix from the lens to each mirror is M_1 and M_2, for mirror 1 and mirror 2 , respectively. For the opposite propagation direction the matrix elements (1,1) and (2,2) are exchanged.

New variables are defined as

$$\xi = \frac{1}{f_T} - \frac{1}{2}\left[\frac{2A_1D_1 - 1}{B_1D_1} + \frac{2A_2D_2 - 1}{B_2D_2}\right], \tag{2.42}$$

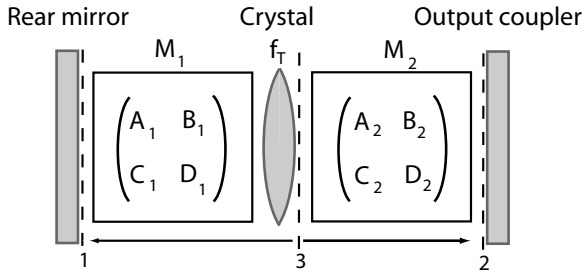

Figure 2.3: Linear resonator with variable thermal lens with focal length f_T and other intracavity elements. The dashed lines denote the reference planes. The matrices are defined for the direction of propagation indicated by the arrows.

$$u = \frac{1}{2}\left[\frac{1}{B_1 D_1} - \frac{1}{B_2 D_2}\right], \tag{2.43}$$

and

$$v = -\frac{1}{2}\left[\frac{1}{B_1 D_1} + \frac{1}{B_2 D_2}\right]. \tag{2.44}$$

The matrix for one trip from reference plane 1 to 2 can be expressed with the newly defined parameters

$$\begin{aligned} M &= \begin{pmatrix} A & B \\ C & D \end{pmatrix} = \\ & \begin{pmatrix} A_2 & B_2 \\ C_2 & D_2 \end{pmatrix} \begin{pmatrix} 1 & 0 \\ -1/f_T & 1 \end{pmatrix} \begin{pmatrix} D_1 & B_1 \\ C_1 & A_1 \end{pmatrix} = \\ & - \begin{pmatrix} D_1 B_2 \left(\xi + u\right) & B_1 B_2 \left(\xi + v\right) \\ D_1 D_2 \left(\xi - v\right) & B_1 D_2 \left(\xi - u\right) \end{pmatrix} \end{aligned} \tag{2.45}$$

The resonator is stable if $0 < AD < 1$ [10]. Since M is a unitary matrix the condition for optical stability can be written also in the form [97]

$$ABCD < 0. \tag{2.46}$$

From Eq. 2.45 and Eq. 2.46 it follows that, as a function of the thermal lens dioptric power $1/f_T$, there are always two stability zones with the same width, given by

$$\begin{aligned} \Delta\xi = \Delta\frac{1}{f_T} &= \min(|u+v|, |u-v|) = \\ & \min\left(\left|\frac{1}{B_1 D_1}\right|, \left|\frac{1}{B_2 D_2}\right|\right) \end{aligned} \tag{2.47}$$

and stability limits $\xi = \pm u$ and $\xi = \pm v$.

The beam radius at the lens can be found using the matrix formalism and applying the criteria for self consistency of the fundamental laser mode after one roundtrip as described in Section 2.3 (see Eq. 2.32 and Eq. 2.19).

$$\omega_3^4 = -\left(\frac{2\lambda}{\pi}\right)^2 \frac{\xi^2}{(\xi^2-u^2)(\xi^2-v^2)}. \tag{2.48}$$

It is apparent that the beam radius approaches infinity in the stability limits and has a minimum in each stability zone. At this minimum the beam size is, in first approximation, insensitive to fluctuations of the thermal focal length and the resonator is dynamically stable. The condition for dynamical stability is a boundary condition for minimum of ω_3

$$\frac{d\,\omega_3^4}{d\,\xi^2} = 0\ , \tag{2.49}$$

which is fulfilled for

$$\xi = \pm\sqrt{|u\,v|}. \tag{2.50}$$

The minimum beam radius at the laser rod then becomes

$$\omega_{3,0}^2 = \frac{2\lambda}{\pi}\,\frac{1}{\Delta\frac{1}{f_T}}. \tag{2.51}$$

$\omega_{3,0}$ is inversely proportional to the range of thermal lens dioptric power independently of the resonator configuration and has the same value in both stability zones.

Another important design consideration is the beam size on each component in the cavity in order to avoid optical damage. The beam radius can be calculated in the same way as for ω_3, starting at the particular element. Here, the expressions for the beam radii on the resonator mirrors are obtained by using Eq. 2.45

$$\omega_1^4 = -\left(\frac{\lambda}{\pi}\right)^2 \frac{BD}{AC} = -\left(\frac{\lambda B_1}{\pi D_1}\right)^2 \frac{(\xi-u)(\xi+v)}{(\xi+u)(\xi-v)}, \tag{2.52}$$

and

$$\omega_2^4 = -\left(\frac{\lambda}{\pi}\right)^2 \frac{AB}{CD} = -\left(\frac{\lambda B_2}{\pi D_2}\right)^2 \frac{(\xi+u)(\xi+v)}{(\xi-u)(\xi-v)}. \tag{2.53}$$

for mirror 1 and 2, respectively.

2.5.2 Misalignment sensitivity

A dynamically stable resonator might be still very sensitive to misalignment of the cavity mirrors and other optical components which affects its efficiency and reliability [32, 96].The mechanical stability of the laser becomes a crucial parameter for lidar applications where the laser is operated on a mobile platform e.g. truck, airplane, ship.

A misaligned element causes displacement of the mode axis and as a consequence introduces additional energy losses at the limiting (mode-selecting) aperture, which for solid-state lasers with large mode volume is constituted by the rod cross-section. In one dimension a misaligned system can be described with a 2×2 matrix for the aligned system and a 2×1 misalignment vector, which accounts for additional shift and slope to the initial position of the beam. The position and the slope of the beam at each plane are measured with respect to the optical axis of the aligned system. After passing the misaligned optical system, the beam is transformed according to:

$$\begin{pmatrix} x_{out} \\ \theta_{out} \end{pmatrix} = \begin{pmatrix} a & b \\ c & d \end{pmatrix} \cdot \begin{pmatrix} x_{in} \\ \theta_{in} \end{pmatrix} + \begin{pmatrix} \delta \\ \alpha \end{pmatrix} \tag{2.54}$$

where the vectors $\binom{x_{in}}{\theta_{in}}$ and $\binom{x_{out}}{\theta_{out}}$ represent the position and the slope of the beam at the incident and exit planes of the system, respectively and $\binom{\delta}{\alpha}$ is the misalignment vector. For the opposite propagation direction the misalignment vector is

$$\begin{pmatrix} d & a \\ c & d \end{pmatrix} \cdot \begin{pmatrix} -\delta \\ \alpha \end{pmatrix}. \tag{2.55}$$

The overall misalignment vector for a cascade of optical components can be obtained by utilizing Eq. 2.54 and considering the output of each element as the input to the next one. As a result, the vector elements are a linear combination of tilting angles and displacements of the misaligned components.

This method can be implemented to calculate the position x_3 and the slope θ_3 of the laser mode at the rod (reference plane 3 on Fig: 2.3). The overall misalignment vector from the lens to mirror 1 is denoted by $\binom{\delta_1}{\alpha_1}$ and from the lens to the second mirror by $\binom{\delta_2}{\alpha_2}$. Starting at reference plane 3, and solving the equation for self-consistency after one roundtrip, the following expression is obtained

$$\begin{pmatrix} x_3 \\ \theta_3 \end{pmatrix} = -\frac{1}{C} \begin{pmatrix} D_2\alpha_1 + D_1\alpha_2 \\ -C_2\alpha_1 + (C_1 - D_1/f_T)\alpha_2 \end{pmatrix}, \tag{2.56}$$

where $C = -D_1D_2(\eta - v)$ is the 3,1 element of matrix M in Eq. 2.45. If we consider the case where only the cavity mirrors are misaligned, than the effect on the mode position is given by Eq. 2.56 with α_1 and α_2 being the angles, at which the mirrors are tilted. The energy loss introduced by the tilted mirrors depends on the mode area and the displacement of the mode axis at the plane of the rod, which is a function of the tilted angle the mirrors. Therefore, the misalignment sensitivity to each mirror can be defined according to [32, 54, 96] as

$$S_i = \frac{x_{3,i}(\alpha_i)}{\omega_{3,0}\alpha_i} \quad \text{with} \quad i = 1, 2. \tag{2.57}$$

and summed up for the sensitivity to the overall misalignment

$$S = \sqrt{S_1^2 + S_2^2}. \tag{2.58}$$

The value of $1/S_i$ is the tilt angle of the i-mirror, which gives rise to diffraction losses with approximately 10 % [54]. This is a considerably high additional energy loss for the case of low-gain laser medium and has big effect on the laser efficiency. The detailed expression for the misalignment sensitivity can be obtained from Eq. 2.56 with $\alpha_1 = 0$ and $\alpha_2 = 0$. This results in overall factor

$$S = \frac{1}{\omega_{3,0}|C|}\sqrt{D_1^2 + D_2^2}. \tag{2.59}$$

This formula indicates that the mechanical stability and thus the efficiency of the laser can be improved for given thermal lens by a suitable choice of cavity components and their position in respect to each other.

2.6 Properties of real laser beams

In Section 2.2 the parameters associated with the dimensions and propagation of an ideal Gaussian beam were described. The Gaussian beam is referred to as diffraction-limited, since it can be focused to the smallest (diffraction-limited) spot. Laser beams, in practice, are mostly multi-mode (except some low power lasers) with non Gaussian beam profile (Eq. 2.18) and these formulas are not applicable. In order to characterize non-Gaussian beams, a parameter has been developed that is based on a universally rigorous mathematical formulation of the beam width, namely the variance definition of beam size [66], discussed below.

2.6.1 Beam width

The beam radius W of an arbitrary beam is defined via the variance σ .

$$W = 2\sigma, \tag{2.60}$$

where $\sigma = \sqrt{\sigma^2}$ with σ^2 being the second moment of the beam intensity profile $I(x, y)$. For the x–direction

$$\sigma_x^2 = \frac{\int_{-\infty}^{+\infty}\int_{-\infty}^{+\infty}(x - x_0)^2\, I(x, y)\, dx\, dy}{\int_{-\infty}^{+\infty}\int_{-\infty}^{+\infty} I(x, y) dx\, dy}, \tag{2.61}$$

and analogous for the y–direction

$$\sigma_y^2 = \frac{\int_{-\infty}^{+\infty}\int_{-\infty}^{+\infty}(y - y_0)^2\, I(x, y)\, dx\, dy}{\int_{-\infty}^{+\infty}\int_{-\infty}^{+\infty} I(x, y) dx\, dy}. \tag{2.62}$$

Here, x_0 and y_0 are the center of gravity (centroid) of the beam, calculated as the first moment of the intensity profile. The second moment, and also the beam width, obeys quadratic free-space propagation dependence of z, which holds for any real laser beam [141]. This definition is consistent with definition of Gaussian beam radius given earlier in Section 2.2.

2.6.2 Beam propagation factor M^2

If an ideal Gaussian and a real non-Gaussian beam are focused with the same lens, their waist will appear at the same position after the lens and both beams will have the same Rayleigh range. The differences are that the real laser beam has larger beam waist and diverges more rapidly. Therefore, these parameters can be defined as a multiple of the equivalent parameters for an ideal Gaussian beam (see Fig: 2.2)

$$W_0 = M\,\omega_0\,, \tag{2.63}$$

$$\Theta = M\,\theta\,, \tag{2.64}$$

where $M \geq 1$. Thus substituting the above equations in Eq. 2.28 gives the beam parameter product of a real beam

$$\Theta W_0 = M^2\,\theta\,\omega_0 = M^2\,\frac{\lambda}{\pi}\,, \tag{2.65}$$

which is M^2 times the beam parameter product of a Gaussian beam. Furthermore, the beam size varies with the distance in free space in the same way as an ideal Gaussian beam except the factor M^4

$$W^2(z) = W_0^2 + M^4\left(\frac{\lambda}{\pi W_0}\right)^2 (z - z_0)^2\,. \tag{2.66}$$

Written in this form, the relation $W(z) = W_0$ for $z = z_0$ is preserved when the distance z is measured in respect to an arbitrary plane, so that $z_0 \neq 0$. The beam propagation through an arbitrary optical system can be calculated with the $ABCD$ law (Eq. 2.30).

"M-squared" is an indicator of how many times diffraction limited is a real laser beam. It is also a measure of how the beam propagates through free space or an arbitrary optical system and thus must be referred to as the propagation factor or propagation constant. Often M^2 is called "beam quality factor", which is inappropriate since it does not fully describe what is considered as beam quality [141]. Depending upon the application, different laser beam properties are required (beam profile etc.) and thus no universal definition of the term "beam quality" exists.

2.6.3 Measurement of M^2

In order to design an optical system with specified output parameters (i.e. focusing of the pump beam into the active laser material), one must know the characteristics of the input beam: M_x^2, M_y^2 values and the associated parameters waist and waist location in both x- and y-directions. Determination of M^2 can be accomplished by measuring the laser beam in a number of locations in the vicinity of the beam waist, one Rayleigh range and beyond two Rayleigh ranges on either side of the beam waist [66]. From the obtained caustic (see Fig. 2.2), the waist size and its location can be found and applied to calculate the beam propagation factor (see Eq. 2.29). To gain access to the beam on both sides of the waist, a focusing lens with known focal length must be used to produce an auxiliary waist. The measured constants are transformed back through the lens to obtain the input-beam's waist and waist location, most likely in respect to the laser output plane.

For an accurate M^2 measurement it is essential to consider the following factors [35]:
(i) Calibration of the beam profiler: If the intensity profile is measured with a CCD camera, the background noise and baseline settings must be adjusted properly. Background subtraction must be applied. The second moment definition for the beam width (also referred to as "4 Sigma method", since $2W = 4\sigma$ [66]) is very sensitive to the outer wings of the beam profile, where the intensity is very low. This can cause overestimating of the beam diameter. Therefore, it is recommended to maintain maximum intensity just below the saturation level of the camera.
(ii) Choice of focusing lens: The lens should be aberration free and aligned properly so that it does not change the M^2 value of the transmitted beam. The focal length should be chosen so that the produced beam waist is sufficiently large and illuminates enough number of pixels on the CCD array. Also, the beam should not overfill the active area for the region of interest. Longer focal length lenses afford more precise Rayleigh range determination, which, in turn, enhance the quality of M^2 measurement.

There are commercially available instruments for automated M^2 measurement (i.e. Spiricon, beam propagation analyzer M2-200). The measurements within this thesis, however, were performed manually. The beam profiles after a lens were sampled with a CCD camera. They were imported into a beam analyzing software (Beam Analyzer v.1.5 developed by Dr. B. Eppich, Technical University Berlin, Germany), which plots the caustic and calculates the beam parameters after the lens. The input beam characteristics were obtained and applied to the design of various optical systems with a program, written by the author in Mathematica.

Chapter 3

Pump configuration

3.1 Pump laser

Two different Nd:YAG pump lasers were used within this project: IBL laser DiNY pq 400/SHG and Continuum Surelite III. DiNY pq 400/SHG was developed by the University of Potsdam together with the Institute of Physics and Meteorology (IPM) at the University of Hohenheim (UHOH) [115] and manufactured by the company IB Laser GmbH, Berlin, Germany. The Surelite III is a commercially available laser from Continuum. An overview comparison of both lasers is given in Table 3.1.

Table 3.1: Specifications of the Nd:YAG lasers used to pump the Cr^{4+}:YAG crystal

Parameter	IBL laser	Continuum laser
Pulse energy, mJ	200	800
Pulse repetition rate, Hz	250	10
Pulse duration, ns	20–24	6–8
Configuration	MOPA	unstable resonator
Q-switching	yes	yes
Injection seeding	yes	no
Excitation	pulsed laser diodes	flash-lamps
Transversal mode structure	TEM_{00}	multimode
Beam profile	near Gaussian	top-hat
Beam propagation factor, M^2	2.5–2.8	2.1
Half angle divergence, mrad	0.2–0.3	0.2–0.3
Polarization	97% p-polarized	70% p-polarized

3.1.1 IBL pump laser

A photograph of the IBL Nd:YAG laser with the cover removed is shown in Fig. 3.1.1. It is diode-pumped laser, based on a MOPA (Master Oscillator Power

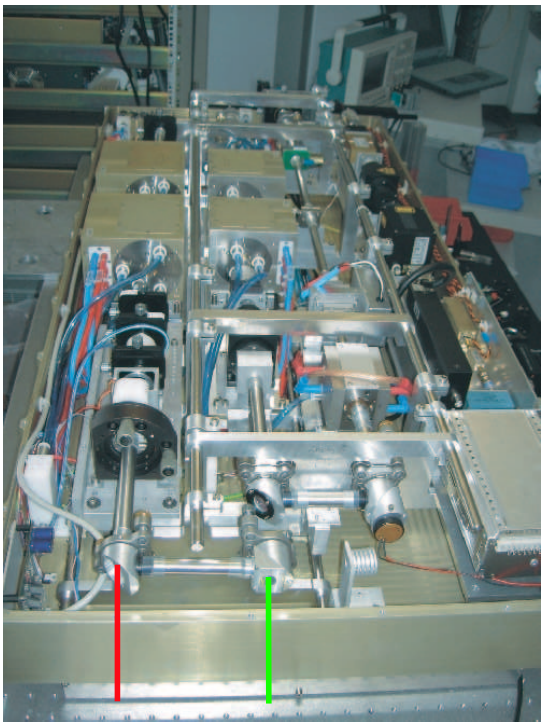

Figure 3.1: IBL Nd:YAG pump laser. The lines represent the laser beams at the fundamental wavelength 1064 nm (red) and at the doubled frequency 532 nm (green).

Amplifier) configuration that allows generation of high pulse energy. The fundamental wavelength is doubled by a second harmonic generation (SHG) crystal. The green wavelength at 532 nm was used for pumping a Ti:Sapphire laser, which has been developed in parallel with the Cr^{4+}:YAG development. The pump laser is capable of delivering up to 200 mJ at 1064 nm in 20-ns pulses at 250 Hz repetition rate and is injection-seeded. The beam is 97 % horizontally polarized.

The intensity distribution is nearly Gaussian and the beam propagation factor $M^2 < 2.5-2.8$ with a full angle divergence of 0.5–0.6 mrad. When the beam is focused with a single lens or combination of two lenses the beam profile remains Gaussian until the waist. Some distortions after the waist were observed indicating remaining phase distortions in the laser beam. The smooth beam profile is an important feature of this pump laser. It allows pumping laser crystals with high energy without the necessity of additional beam shaping devices. Therefore, a compact design of the frequency converter is possible.

Some important measurements were conducted with this pump laser. The absorp-

tion behavior of the available Cr^{4+}:YAG crystal was investigated and new crystals with optimized parameters were purchased. Also, the thermal lensing of the new crystals was measured for repetition rates 125 Hz and 250 Hz, which to the authors knowledge, is a new result about this crystal, and can be considered by the design of such high repetition rate Cr^{4+}:YAG lasers.

Due to the failure of one of the key components at the end of the third year of this project, the development of the Cr^{4+}:YAG laser was carried out and completed in the lidar laboratory of the Earth Observing Laboratory (EOL) at the National Center for Atmospheric Research (NCAR) in Boulder, Colorado as part of a collaboration with the IPM. The experiments were performed using one of EOL's Continuum Nd:YAG pump lasers.

3.1.2 Continuum pump laser

The Continuum pump laser (Fig. 3.2) is a flash-lamp-pumped Q-switched Nd:YAG laser, producing 800 mJ pulse energy at 10 Hz at 1064 nm wavelength. The whole energy is extracted from a single laser rod in unstable resonator with Gaussian output coupler. The pulse duration at FWHM is 6–8 ns. The pointing stability is sufficiently good and the pulse-to-pulse energy variation is about 10 %. The beam is 70 % horizontally polarized.

Figure 3.2: Continuum Surelite III Nd:YAG pump laser.

The Cr^{4+}:YAG crystal must be pumped with a linearly polarized beam in order to achieve maximum conversion efficiency [85] (see Section 4.1.2). Therefore a thin film polarizer (TFP_1) at the Brewster angle was used to transmit the horizontal polarization and reflect the vertical to a beam dump (Fig. 3.3).

The output power of the Nd:YAG laser can be changed by varying the flash-lamp voltage, which corresponds to lower pump energy. As it was shown in Section 2.4, different pump energy levels will introduce different thermal lensing in the laser rod,

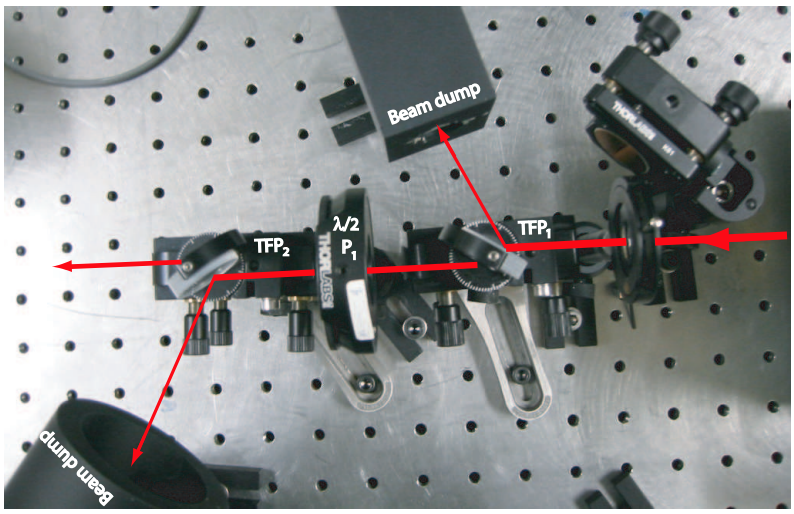

Figure 3.3: Set up for achieving horizontal polarization (with a thin film polarizer TFP_1) and external energy attenuation (with a half waveplate $\lambda/2$ P_1 and TFP_2).

which leads to changes in the beam propagation. To be able to investigate Cr^{4+}:YAG laser characteristics for different pump pulse energies and to keep the pump beam propagation parameters constant, an external energy attenuator was built. It is composed of a half waveplate in a rotary mount $\lambda/2$ P_1 and a thin-film polarizer TFP_2 (Fig. 3.3). The pulse energy was adjusted by changing the transmission of the polarizer when the polarization of the beam is rotated with the half waveplate. The second TFP was placed at minus the Brewster angle, so that no additional astigmatism was introduced.

After cleaning up the polarization and building the external energy attenuator the beam profile was observed at full power with a CCD camera (DataRay, model TaperCamD20/15). The beam was flat-topped and multimode (Fig 3.4).

The beam propagation parameter was measured using a plano-convex lens (PLCX) with nominal focal length of 500 mm (see Section 2.6.3 for the description of the measurement). The lens was placed 673 mm from the laser output. The caustic of the beam propagation and beam profiles at different distances from the focusing lens are presented in Fig. 3.5. The beam is slightly astigmatic with a waist separation of 15.2 mm. The astigmatism is caused most likely by tilted elements in the laser resonator (tilted dielectric polarizer of the Q-switch).

Localized high energies, known as hot spots, are present in the beam (see Figs. 3.4 and 3.5). Their position and intensity changes randomly when the beam propagates away from the lens (see the beam profiles on Fig. 3.5). The energy density in the hot spots can exceed the damage threshold of the optical components even at low pulse energy, due to their small size. The beam has smooth profile only at the waist. This

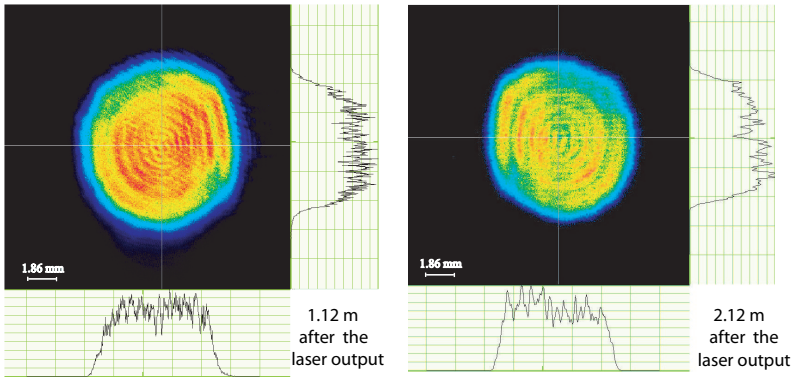

Figure 3.4: Beam profile at distances 1.12 m (left) and 2.12 m (right) after the laser output. The beam profile on the right hand side was taken after a 45° folding mirror and is therefore a mirror image of the profile at this distance.

would be a good place for the laser rod, if the beam size is larger. However, all other components along the beam path would be at positions with bad beam profile.

In order to insure maximum safety for the optical components and the laser rod at high pulse energies, a vacuum spatial filter was built, which transformed the pump beam profile to a clean near Gaussian shaped beam.

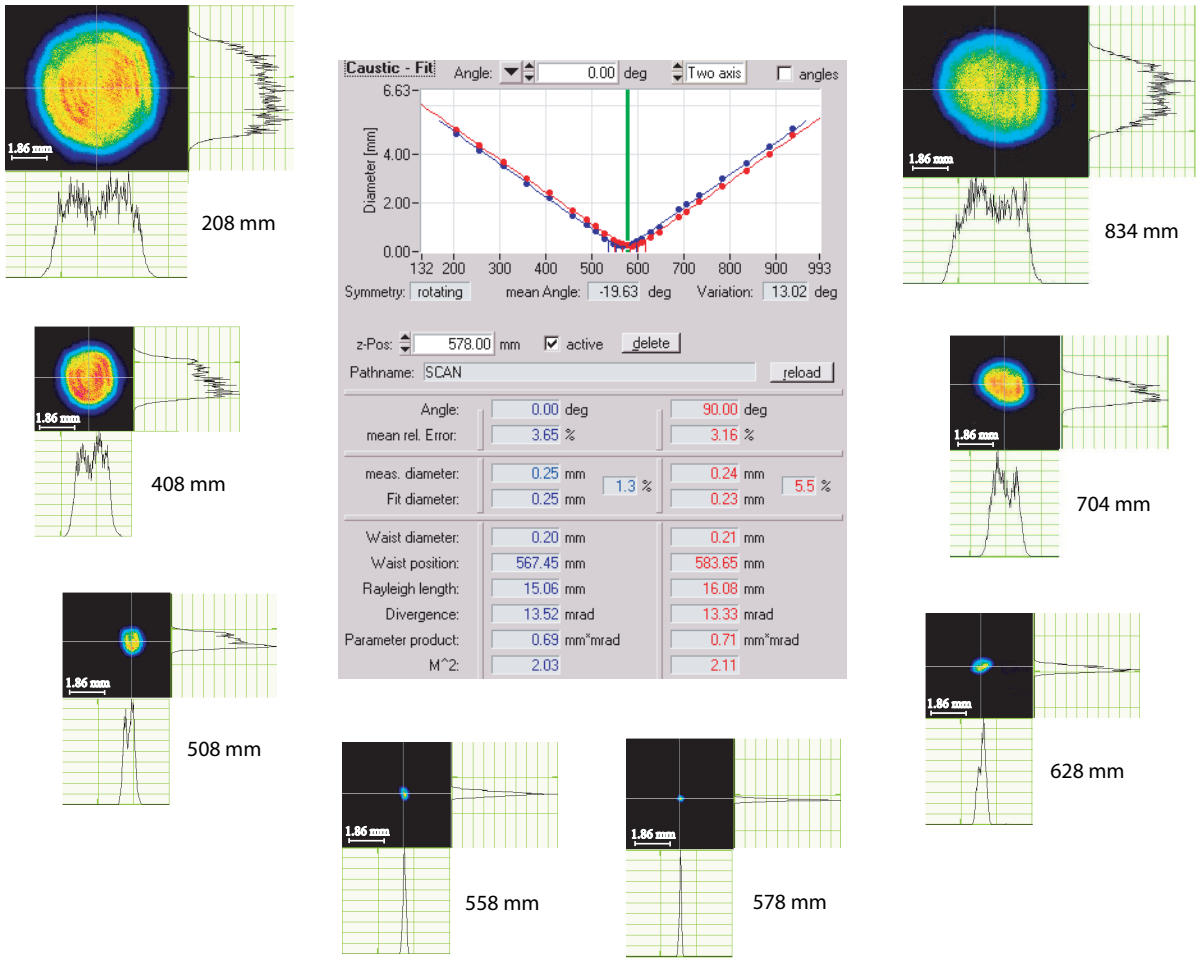

Figure 3.5: M^2 measurement of the Surelite Nd:YAG laser beam using a PLCX lens with a focal length of 572.7 mm at 1064 nm. In the center is shown the beam propagation caustic measured after the lens. The beam profiles are taken after the lens at a distance as indicated in the low right corner of each image.

3.2 Vacuum spatial filter

Vacuum spatial filters (VSF) are an important component in high-peak power lasers [11, 26, 63]. They are used to remove abberations from laser beams and produce an improved beam containing only a single transverse mode of the laser's optical resonator.

3.2.1 Theory of operation

The spatial filter is comprised of two positive lenses and a pinhole placed in their common focus as illustrated in Fig. 3.6 [55, 69].

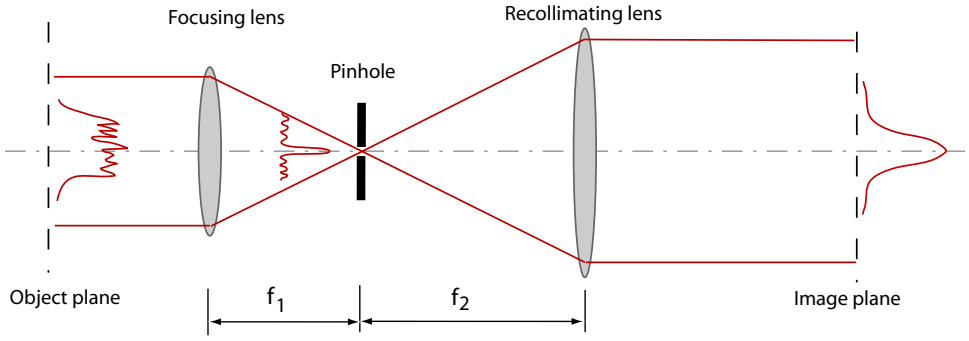

Figure 3.6: Principal of spatial filtering.

The first focusing lens produces a diffraction pattern at the focal plane, which represents the spatial Fourier-mode spectrum of the intensity distribution of the beam at the object plane. Higher spatial frequencies, corresponding to fine structures in the initial intensity distribution, appear farther from the optical axes of the system and are blocked by the surface surrounding the pinhole. Only the low-frequency components of the Fourier spectrum, constituting the smooth transverse intensity profile, are passed through the pinhole. The second lens performs the inverse Fourier transform and projects the filtered beam onto the image plane. The selection of the pinhole diameter is based on maximizing the amount of energy passed while blocking the undesired noise and minimizing the diffraction effects on the edge of the aperture.

3.2.2 Design

When used for high peak power lasers, high energy density in the focal spot is reached which can cause optical air breakdown. Therefore the spatial filter must be in a vacuum. Also, the design of the pinhole must be considered. The intensity of the clipped unwanted light is sufficient to ablate plasma at the edge of the aperture. The plasma causes distortion of the wave-front of the transmitted light and eventually closure of the pinhole. The operation of a conventional washer-type pinhole for

spatial filtering has been investigated and new pinholes with conical profile proposed in [23, 111]. The conical profile provides larger surface area for the blocked energy to dissipate thus reducing the local fluence on the structure. Consequently the plasma formation is minimized. Furthermore, part of the rejected light is reflected rather than absorbed.

In order to find a compact and reliable design, different spatial filters were tested first with low pump pulse energy and no vacuum. Short spatial filters were set up with an input focusing lens with a nominal focal length of 300 mm. The lens produced very small focal spots in the x- and y-plane with too high energy density in the wings which would destroy the pinhole in a short time period. Therefore, an additional beam reducer 2:1 was placed before the input lens. As a result, the focal spots were increased by almost a factor of two and thus the energy density reduced by factor of four. The pinholes were diamond wire dies from Woodburn Diamond Die, Inc. with diameters 157.5 μm, 215.9 μm and 285.7 μm. The pinhole was mounted on an XYZ translation stage for fine alignment.

The beam was successfully filtered when the pinhole was placed in either focal plane (x and y). But the beam spots in the foci were elliptic and therefore causing strong burning at the surface of the pinhole along the long axis of the ellipse. Also, the exit beam after the pinhole remained elliptical. Best results, in terms of beam shape, were obtained with the 285 μm pinhole when placed in the medial focus, where the beam was circular. However, high energy density caused burning of the pinhole for pump pulse energy as low as 30–35 mJ. Further experiments showed that the burning and also deformation of the pinhole can be avoided, or sufficiently decreased, if the focus has a diameter bigger than 2 mm. This automatically excluded the possibility of building a short spatial filter.

The final pumping configuration with the vacuum spatial filter is depicted in Fig. 3.7. The desired large beam diameter at the waist was produced by a 2:1 beam reducer $L_2 - L_3$ (L_2: plan convex lens with f=150 mm, L_3: plan concave lens with f=–75 mm, separation: 85 mm) and a weak focusing lens L_4 with 2-m focal length. The separation between the foci in the x- and y- plane was reduced by a cylindrical lens L_1 (f_x=10 m).

Before building the vacuum system, beam profiles were taken after the focusing lens L_4 and the maximum energy density was calculated, in order to determine the safe positions for the Brewster windows and folding mirrors. The results are plotted in Fig. 3.8 for pulse energy of 100 mJ. The final location of the optical components is indicated on the plot.

A target with different bore diameters was used to optimize experimentally the performance of the spatial filter. Best results for the filtered beam were achieved with a 1.9 mm in diameter pinhole, placed in the medial focus where the spot was approximately circular. The medial focus was 2.65 m after the focusing lens and had diameters of 2.68 mm and 2.60 mm in x- and y- plane, respectively. The transmission of the filter was 80 %.

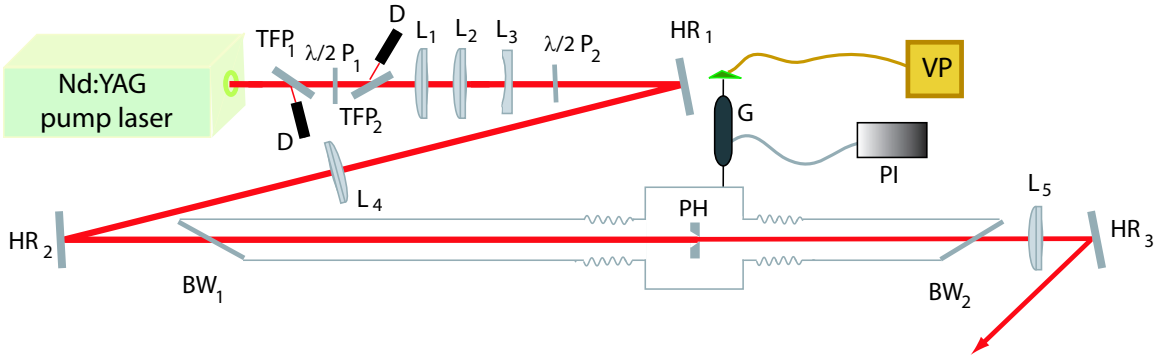

Figure 3.7: Pump configuration. TFP_1, TFP_2: Thin film polarizers at Brewster angle, $\lambda/2P_1, \lambda/2P_2$-half-waveplates, D: beam dump, L_1: cylindrical lens, L_2: plano-convex lens, L_3: plano-concave lens, $HR_1 - HR_3$: high reflectivity mirrors for 1064 nm,L_4: focusing lens for the spatial filter, BW_1, BW_2: fused silica windows at Brewster angle, PH: pinhole, L_5: recollimating lens, G: Gauge, PI: pressure indicator, VP: vacuum pump.

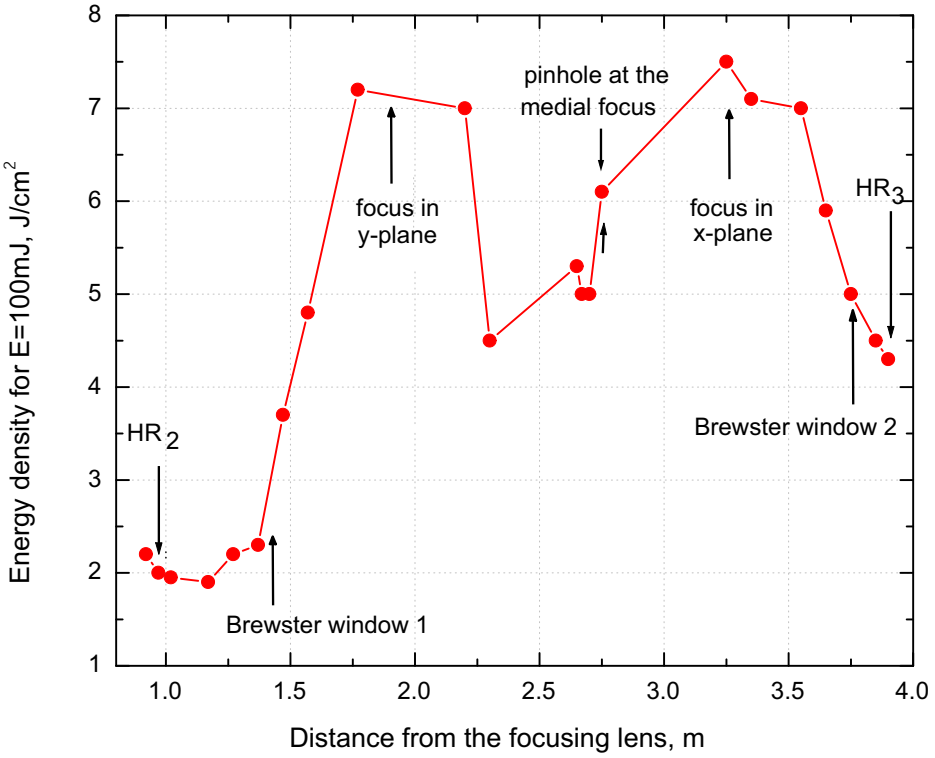

Figure 3.8: Variation of the maximum energy density of the beam propagating after the VSF's input focusing lens for 100 mJ pulse energy. The position of the optical elements and the pinhole are marked on the plot.

The transmitted beam was further shaped with the recollimating lens L_5 with a focal length 1 m placed at 1.1 m after the pinhole.

The actual vacuum spatial filter is shown on the photograph below.

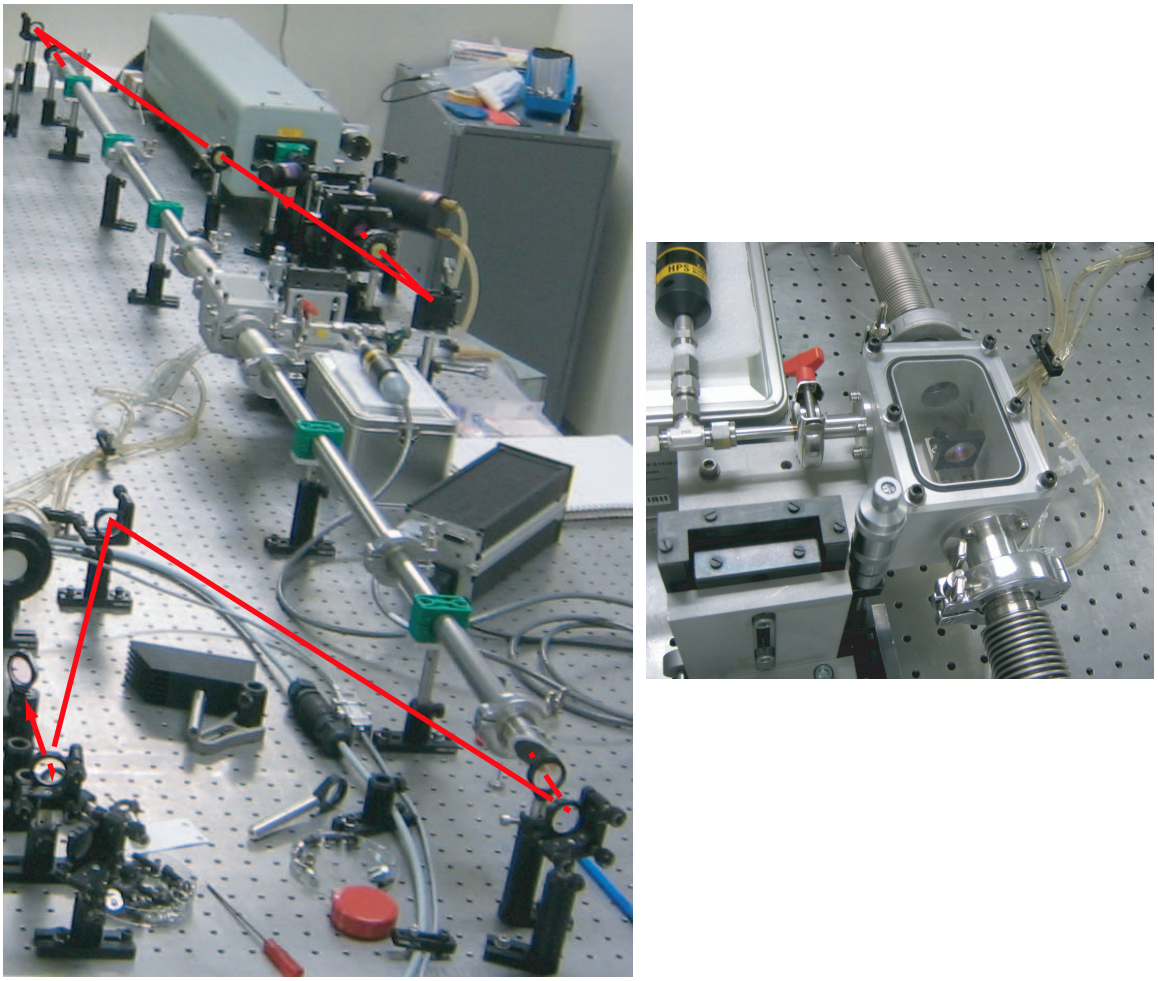

Figure 3.9: Photograph of the vacuum spatial filter in the lab. Left: the entire system. Right: the vacuum chamber with the pinhole.

The pinhole was manufactured by the Design and Fabrication Services (DFS) at NCAR. It was made of stainless steel and had a fine polished reflective conical profile. It was placed in a small vacuum chamber and the chamber was mounted on a XYZ translation stage. Flexible bellow sections allowed movements of the vacuum chamber during alignment. The rigid tubes were standard 1" KF straight sections from HPS Products. The spatial filter was sealed with a 2" uncoated plane windows from CVI Laser, LLC. Its overall length was 2.6 m. The filter was evacuated down to 133 Pa with a vacuum pump from Welch Scientific, model 1402. The pressure in the vacuum system was monitored with an HPS Pirani gauge. A leak detector was used to check

the seals. The pressure of the vacuum spatial filter was maintained once every couple weeks.

3.2.3 Improvement of the pump beam characteristics

The vacuum spatial filter improved the pump beam profile and made it possible to investigate the Cr^{4+}:YAG laser properties at high pump energies.

The improved beam profiles after the VSF are shown on Fig. 3.10 (compare with Fig. 3.5). The beam was rather converging than collimated. The aim with using 1-m recollimating lens was to provide a large and circular beam at the position of the crystal. Later the rod was placed at the medial focus (about 1.6 m after the recollimating lens), where the beam was fitted to 94 % Gaussian shaped.

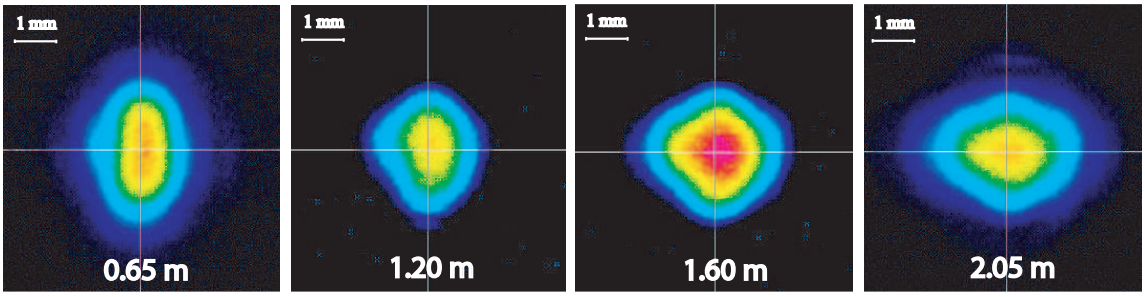

Figure 3.10: Beam profiles after the vacuum spatial filter. The distance from the recollimating lens is marked on each image.

The use of this filter is only required as long as the pump laser has a poor beam profile. The experiments presented hereafter can be used as a baseline of the expected performance of Cr^{4+}:YAG pumped with laser exhibiting better beam characteristics.

3.3 Cooling of the laser crystal

In any solid-state laser material operating at high average power, a significant part of the absorbed pump energy is converted to heat in the crystal. The increase of temperature causes shortening of the fluorescence lifetime and induces thermal lensing in the laser rod. As a result, the overall laser efficiency is usually reduced. In order to minimize these effects, the laser material was actively cooled.

The laser rod was clamped between two aluminum shells (C in Fig. 3.11). In order to determine the optimum bore diameter of the shell two factors were taken into account: first, the accuracy of the measurement of the crystal's diameter, provided by the polisher. Second, the variations induces by thermal expansion and contraction of the rod by a temperature change of $\pm 20\,C^{o}$. In addition, the bore surface was coated

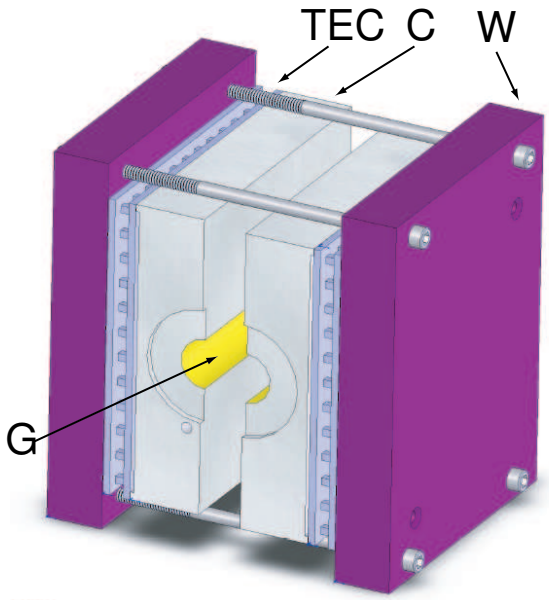

Figure 3.11: Solid model of the crystal cooler. C: clamp shells, G: gold coating, TEC: Peltier thermoelectric cooler, W: block with circulating water.

with $9\,\mu m$ thick gold layer. It ensures good mechanical contact, needed for effective heat transfer. Gold was chosen due to its high thermal conductivity.

The temperature of the crystal was measured by an RTD element (Omega, part. nr. 1PT100GX0518) and stabilized with a Peltier module controller (AMS Technologies, AMS 2410) to the set value with an accuracy of $\pm 2C^o$. According to the difference between the actual and set temperature of the crystal the controller provides current to Peltier thermoelectric coolers TEC (Melcor), mounted on the clamp shells. The hot side of the Peltier elements was cooled by circulating water in another aluminum block W and a recirculating chiller (Melcor, part. nr. MCR300). Thermal transfer compound was applied to the RTD and Peltiers elements.

The crystal cooler was designed by J. Fox from DFS at NCAR and fabricated at the machine shop at IPM. The clamp shells were coated at the IPM using Technics-Hummer sputtering coater.

Chapter 4

Chromium YAG laser

4.1 Laser crystal

Cr^{4+}:YAG is widely used as a passive Q-switch for Nd:YAG laser [67, 109, 133, 144]. In 1988 Angert et al. [2] reported the capability of the crystal as a wavelength converter of wavelengths around 1000 nm to wavelengths in the mid-IR spectral range of $\approx 1300 - 1500$ nm. Since then a lot of research has been conducted with different pump lasers and in a variety of mode operation [130]. Possible pump sources include InGaAs laser diodes at around 970 nm [1, 143], Yb-fiber lasers at 1064 nm [90] and most commonly used Nd:YAG laser at the fundamental wavelength [87, 113]. Quasi-CW and pulsed regime operation has been investigated in [38, 85, 101, 106, 184]. CW operation has been achieved by [1, 81, 131, 170]. Mode-locked Cr^{4+}:YAG laser have been demonstrated in [44, 90]. Best conversion efficiency of 22 % in quasi-CW [85] and 12 % for pulsed regime [15] have been reported.

4.1.1 Physical properties

Cr^{4+}:YAG crystal consists of the well known and widely used yttrium aluminum garnet (YAG, $Y_3Al_5O_{12}$) in which some of the trivalent aluminum ions are substituted by the laser active tetravalent chromium ions (Cr^{4+}). The difference in charge site is compensated by additional co-doping with Ca^{2+} or Mg^{2+} ions [83, 86]. The crystal can be grown in good optical quality by the Czochralski method [31, 82]. The concentration of active ions can be increased by a post growth annealing [84, 143].

Cr^{4+}:YAG exhibits characteristics of its host crystal (the YAG) such as high thermal conductivity, hardness and good optical quality [85]. Some of the important physical parameters are listed in Tab. 4.1 according to [75, 129].

Table 4.1: Physical parameters of Cr^{4+}:YAG crystal

Parameter	Value	Unit
Refractive index	1.81	1
Density	4.56	g/cm^3
Mohr's hardness	8.5	1
Heat conductivity	0.13	W/(cm.°C)
Thermo-optic coefficient	9.8×10^{-6}	/°C
Melting point	1970	°C

4.1.2 Laser properties

Active research has yielded an understanding of the configuration of the active Cr^{4+} ions in the host crystal [84, 113]. The fluorescence in the 1400 nm region, caused by pumping with light at 1000-nm wavelength, is attributed to tetrahedrally coordinated Cr^{4+} ions. According to [38, 85, 184] part of the chromium ions may also occupy octahedral sites but do not contribute to the near-infrared fluorescence. In addition, a large number of trivalent chromium ions exist in octahedral sites in the crystal [39, 85]. This makes it difficult to estimate the concentration of the tetrahedrally coordinated ions in order to determine parameters such as the absorption cross-section.

Researchers have inferred the presence of octahedrally coordinated Cr^{4+} ions from the absorption spectrum. Three broad absorption bands around 480 nm, 640 nm, and 1000 nm have been observed [38, 83]. Only the absorption around 640 nm, and 1000 nm is attributed to the tetrahedrally coordinated chromium ions.

Energy-level diagram

The optical transitions of the tetrahedrally coordinated Cr^{4+} ions in YAG can be described by a four-level system [83, 86]. The energy diagram is depicted in Fig. 4.1. Cr^{4+} ions on the ground state $|g\rangle$ absorb the pump photons at wavelength λ_P and are excited to the first excited state $|3\rangle$. The probability of this transition is the ground-state absorption cross-section σ_{GSA}. Fast (few ps) non-radiative decay occurs to the upper laser level $|2\rangle$. The laser transition takes place between the energy levels $|2\rangle$ and $|1\rangle$ (with probability the stimulated emission cross-section σ_{SE}) and results in emission of photons at the laser wavelength λ_L. The lifetime of the upper laser level $|2\rangle$ at 300 K is $\tau_2 = 3.4 - 4.7\,\mu$s (3.4 μs in [184], 4.1 μs in [86], 4.7 μs in [101]). A fast (few ps) non-radiative decay to the ground-state level follows. The ions from the upper laser level can be further excited to higher lying energy levels $|4\rangle$ and $|5\rangle$ due to absorption of the lasing and pump wavelengths, respectively. These transitions are known as excited-state absorption (ESA). They are additional losses which give a rise of the laser threshold pump power and reduce the slope efficiency (see Section 2.1).

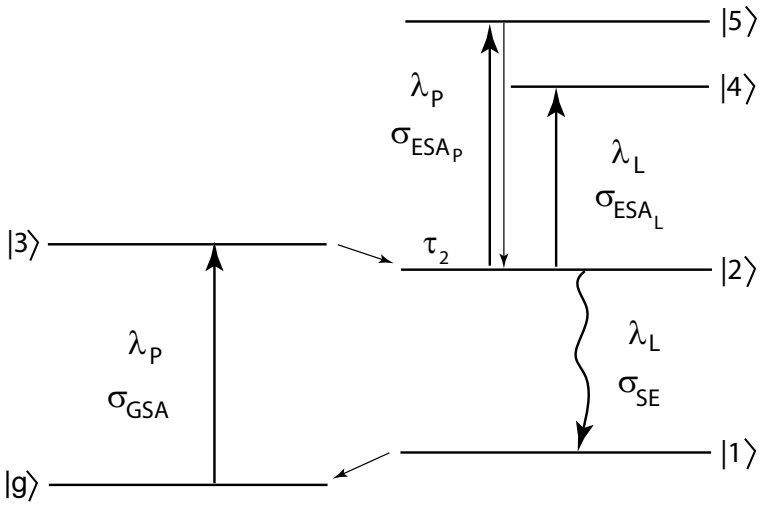

Figure 4.1: Energy level diagram of Cr^{4+} ions. $|g\rangle$: ground state, λ_P and λ_L: pump and laser wavelength, respectively, σ_{GSA}: ground-state absorption cross-section, σ_{SE}: stimulated emission cross-section, σ_{ESA_P} and σ_{ESA_L}: excited-state absorption cross-section of the pump and laser wavelengths, respectively, τ_2: lifetime of the upper laser level $|2\rangle$.

Suda et al. [153] suggested a 5-level diagram where the excited ions from levels $|4\rangle$ and $|5\rangle$ decay to an additional level with relaxation time about 120 ns. However, in the case of gain switching, one can assume that the ions from this level return to the upper laser level during laser pulse build-up and thus the initial inversion population is not affected (see Section 2.1). Therefore, the 4-level approach is considered here.

A summary of the published values of the pump absorption, stimulated emission, and the ESA cross-sections are given in Tab. 4.2. It has to be noted that some of these parameters vary by an order of magnitude which makes it difficult to model the performance of this laser (see Section 2.1). In the first column of Tab. 4.2 are listed the values of the small-signal (or initial) absorption coefficient α. α with unit of cm^{-1} is the linear attenuation of the incident pump intensity I_0 by propagating through the crystal, described by the Lambert-Beer law

$$I = I_0\, e^{-\alpha\, l_{cr}}. \tag{4.1}$$

From α and σ_{GSA} the total number density of the active ions can be estimated

$$n_T = \alpha/\sigma_{GSA}. \tag{4.2}$$

Table 4.2: Published values of the initial absorption coefficient and the cross-section of the transitions in Cr^{4+}:YAG crystal

α cm^{-1}	σ_{GSA} $\times 10^{-18}, cm^2$	σ_{SE} $\times 10^{-19}, cm^2$	σ_{ESA_P} $\times 10^{-19}, cm^2$	σ_{ESA_L} $\times 10^{-19}, cm^2$	Reference
1.6	7	3	5		[184]
2.6	5.7±2		8±2		[39]
1	5±1	7–8	5±2	4–5	[15]
	3.9	3.3	5.3	1.8	[107]
		3.3			[86]
2.7	3±0.5		2±0.5		[144]
2.5	2.9		2.3		[101]
	2.5		3		[21]
2.1	1.4	0.91	1.2–1.7	0.6	[153]
1.5	1.2	0.75		0.29	[131]
	0.87±0.08		2.2±0.2		[133]
	0.36				[109]
2.2	5		8		this work
3.2	5	2.65	4.8	1.75	this work

Tunability

Eilers et al. [38] have demonstrated a broad emission spectrum between 1100 nm and 1700 nm that of Cr^{4+}:YAG at room temperature. Tunability of this laser in the range of 1340–1570 nm [15] and 1350–1550 nm has been obtained using a birefringent filter [1, 38, 85]. The peak wavelength is at 1420–1430 nm.

Polarization effects

It has been found that the absorption and the laser efficiency depend strongly on the pump polarization [38, 39, 83, 85]. This behavior is explained by the fact that the Cr^{4+} ions occupy distorted tetrahedral sites. The tetrahedrons are trigonally distorted along one of the three orthogonal crystallographic axes $\langle 100 \rangle$, $\langle 010 \rangle$ and $\langle 001 \rangle$ of YAG [83, 86]. As a result there are three equivalent groups of Cr^{4+} ions oriented along those axes and the crystal is optically anisotropic [39, 83] (in contrast to YAG). Each of these groups can be selectively excited by linear polarized light at 1064 nm. Best results in terms of conversion efficiency are obtained when the pump beam propagates along the $\langle 100 \rangle$ crystallographic axis and is linear polarized parallel to $\langle 010 \rangle$ [38, 85].

4.2 Measurement of the pump absorption

The absorption of the pump wavelength at 1064 nm saturates at low ($0.033\,\mathrm{J/cm^2}$) [39] to moderate ($0.155\,\mathrm{J/cm^2}$) [131] pump energy density. The saturation energy fluence is calculated as $U_{sat} = h\nu_P/\sigma_{GSA}$ [153]. As a result of the ground-state bleaching, part of the pump energy is transmitted through the crystal and can not be used for the wavelength conversion. In addition, some of the pump photons are lost due to the absorption to higher excited state $|5\rangle$ (see Fig. 4.1). The decay time of level $|5\rangle$ is estimated at $50(\pm5)\,\mathrm{ps}$ in [184] and 100 ps in [153] so the population of the upper laser level remains almost constant.

The attenuation of the pump energy fluence $U_P(z)$ with distance z through the crystal can be calculated as [8, 15]

$$\frac{d\,U_P}{dz} = -\alpha\frac{h\nu_P}{\sigma_{GSA}}\left\{\left[1-\frac{\sigma_{ESA_P}}{\sigma_{GSA}}\right].\left[1-\exp\left(-\sigma_{GSA}\frac{U_P}{h\nu_P}\right)\right]+\sigma_{ESA_P}\frac{U_P}{h\nu_P}\right\}. \qquad (4.3)$$

In the saturation regime, the transmission remains constant by further increase of the pump energy. This effect is attributed to the unsaturated ESA at the pump wavelength. The maximum transmission is therefore a function of the σ_{ESA_P}, the total number density of the active ions n_T and the length of the crystal l_{cr} and it can be estimated according to [39] as

$$T_{max} = \frac{U_P}{U_{P,0}} = \exp\left[-\sigma_{ESA_P} n_T\, l_{cr}\right]. \qquad (4.4)$$

The laser crystal, used at the beginning of this study has been grown at the University of Hamburg [82]. This crystal had an initial absorption coefficient $\alpha = 2.2\,\mathrm{cm^{-1}}$. It was cut into two 20 mm long and 5 mm diameter crystals (Fig. 4.2(a)). The end surfaces were polished by the company FEE GmbH, Germany and antireflection (AR) coated for both pump and laser wavelengths by DS-Technik Tafelmaier, Germany. The AR coating had a damage threshold of $10\,\mathrm{J/cm^2}$.

The absorption of the pump wavelength was measured with the IBL pump laser. The pump beam diameter at the rod was 2 mm and the temperature of the crystal was stabilized to 15 °C. At 100 mJ pump energy the transmission of the crystal was almost 50 % (see Fig. 4.3). This result in terms of pump energy density was confirmed again with 3 mm and 4 mm pump beam diameters. The energy density was calculated for a spot with the measured diameters using 4-Sigma method (see Section 2.6.1) and homogeneously distributed energy.

For more effective pumping and wavelength conversion, the absorption of the crystal should be increased. According to Eq. 4.3 this is possible for longer crystals with higher concentration of the active ions. The maximum doping level for a good optical quality Cr^{4+}:YAG corresponds to maximum small-signal absorption coefficient $\alpha = (3.5-4.0)\,\mathrm{cm^{-1}}$ (according to Dr. A. Shestakov from IRE Polys, Moscow). In order to calculate the optimal length of the crystal, the experimental transmission

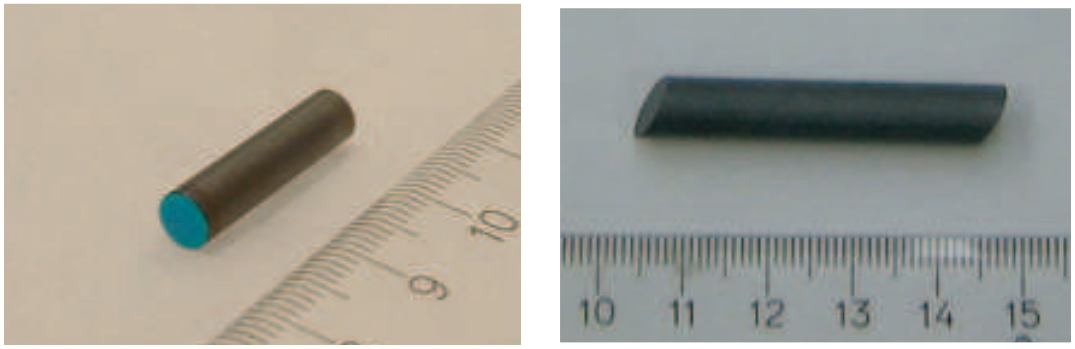

(a) (b)

Figure 4.2: Cr^{4+}:YAG laser crystal. (a) 20×5 mm rod with AR coated end surfaces, (b) 40×7 mm rod with Brewster-cut end faces

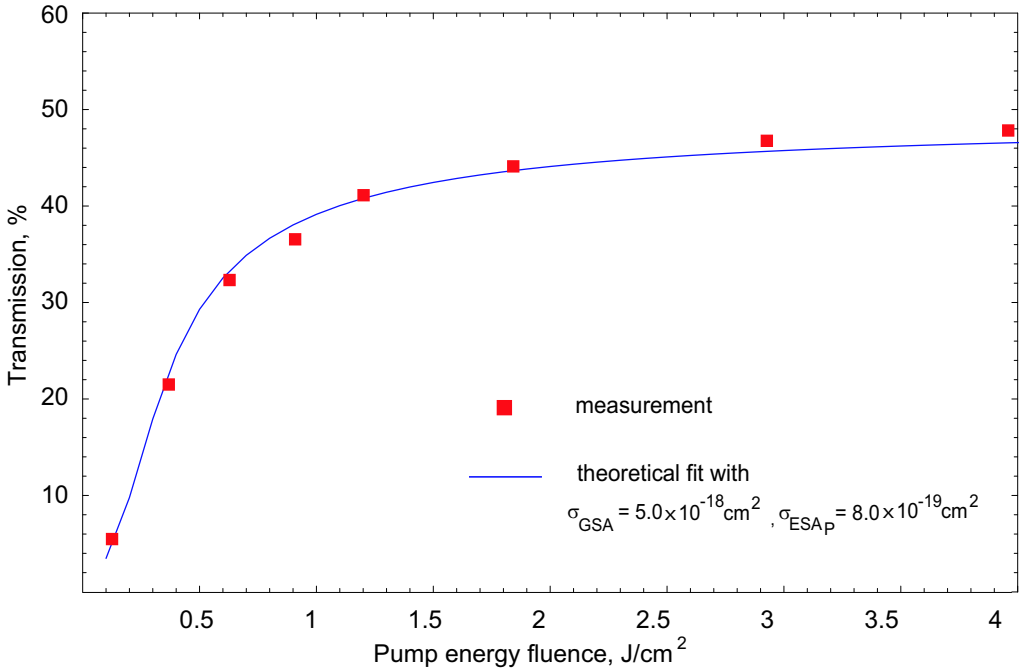

Figure 4.3: Theoretical fit of the experimental data obtained with a 20 mm long laser rod with a small-signal absorption coefficient $\alpha = 2.2\,\mathrm{cm}^{-1}$. The crystal temperature was stabilized to 15 °C. The pump beam diameter was 2 mm.

curve was fitted with the aid of Eq. 4.3, which yielded $\sigma_{GSA} = 5 \times 10^{-18}\,\mathrm{cm}^2$ and $\sigma_{ESA_P} = 8 \times 10^{-19}\,\mathrm{cm}^2$ (see Fig. 4.3). These values are in a good agreement with those reported in [39].

Using these parameters, a set of transmission curves was calculated for different crystal lengths (Fig. 4.4). The calculations showed that sufficiently low transmission can be expected in a rod at least 40-mm long. Due to mechanical difficulties of producing very long clamp shells with accurate bore diameter, which is critical for good thermal contact, the 40 mm length of the crystal was chosen.

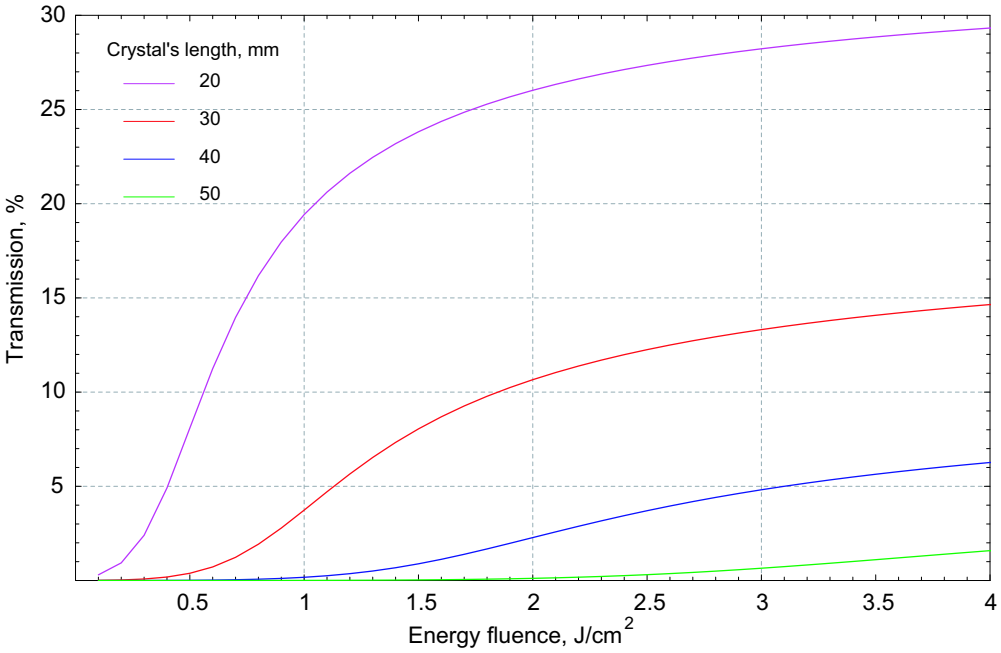

Figure 4.4: Theoretical transmission of the pump energy at 1064 nm as a function of the pump energy density for Cr^{4+}:YAG crystal with various lengths. The parameters used for this calculations are $\alpha = 3.5\,\mathrm{cm}^{-1}$, $\sigma_{GSA} = 5 \times 10^{-18}\,\mathrm{cm}^2$ and $\sigma_{ESA_P} = 8 \times 10^{-19}\,\mathrm{cm}^2$.

New crystals were purchased from IRE Polys. They were 40×7 mm highly doped Cr^{4+}:YAG cylindrical rods with a specified initial absorption coefficient of 3.5–4.0 cm^{-1}. A photograph of the new crystal is shown in Fig. 4.2(b). The new rod had Brewster-cut end faces with specified damage threshold of more than 700 $\mathrm{MW/cm}^2$ (Dr. A. Shestakov).

The absorption behavior of the new crystal was measured with the IBL and Continuum Surelite pump lasers and compared to the theoretical predictions. The experimental transmission was a lot higher than calculated. Please note, that the energy fluence in the crystal was corrected for the Brewster angle geometry. Due to the Brewster incident angle, the pump beam diameter is elliptical in the crystal (larger

in the tangential plane) and thus the energy density is lower compared to normal incidence. Also, the overall length of the rod was 40 mm, but along the propagation axis in the middle of the crystal was 36.2 mm. The transmission curve of this crystal is presented in Fig. 4.5. It can be well fit with α= 3.2 cm^{-1}, σ_{GSA}= 5 × 10^{-18} cm^2 and σ_{ESA_P}= 4.8 × 10^{-19} cm^2. The initial absorption coefficient was lower than specified. Consequently, a different fitting value of the ESA cross-section was used, which agrees well with [15].

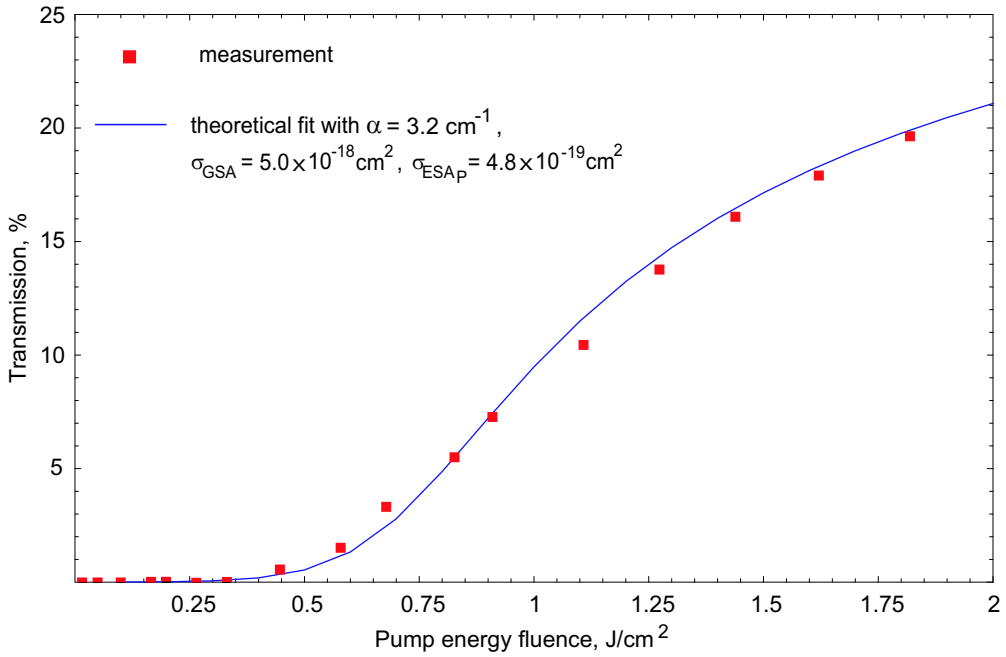

Figure 4.5: Theoretical fit to the experimentally measured transmission of the 40-mm long Cr^{4+}:YAG crystal. The crystal temperature was stabilized to 15 °C. The pump beam diameter was 2 mm. The best fit parameters are as indicated in the legend.

This study emphasized on the experimental optimization of the performance of Cr^{4+}:YAG in terms of conversion efficiency at high pump energy. The laser performance was investigated using 2-mm and 3-mm pump beams. The maximum pump energy in both cases was 130 mJ and the transmission changed corresponding to the pump energy density. The transmission as a function of the pump energy for different pump beam size is shown in Fig. 4.6 for future reference.

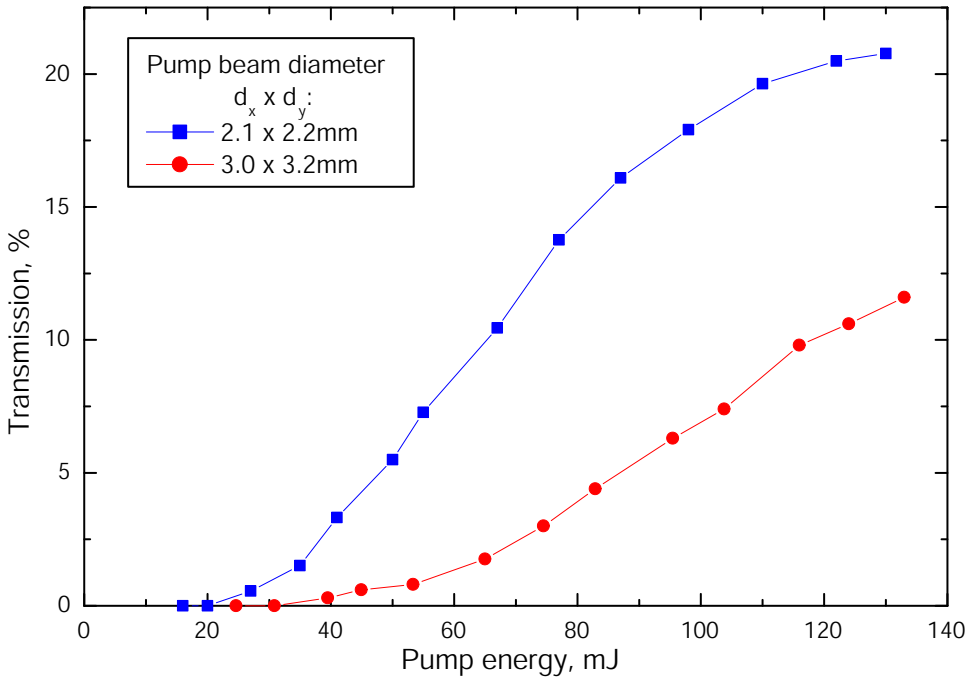

Figure 4.6: Experimental transmission of the new crystal vs. pump pulse energy for two pump beam sizes as indicated in the legend.

4.3 Measurement of thermal lensing

The thermal lensing focal length was measured using the pump-probe technique [71]. Figure 4.7 schematically shows the experimental arrangement. A linear polarized CW beam at 1310 nm was used as the probe beam. It was produced by a fiber coupled laser diode (LD) (NTT Electronics, model NLL1B5G1AA) and collimated with a fiber collimator package from Thorlabs (F220FC-C). It is worth pointing out, that the commonly used He:Ne laser as a source for the probe beam at 532 nm or 632.8 nm can not be applied for Cr^{4+}:YAG due to the strong absorption of chromium ions in the visible wavelength region. Indeed, the crystal is dark in color and not transparent to the eye.

The probe beam was coupled into the crystal through the high-reflectivity folding mirror HR. In order to ensure good overlap in the rod between the probe and pump beam, alignment apertures with bore diameter of 1 mm were used. They were mounted directly on the clamp shells 3 mm from the crystal end surfaces. The probe beam diameter was slightly smaller than the pump beam spot. In the presence of thermally induced lens in the laser rod, the probe beam focuses after the rod. Its diameter was measured after the crystal as a function of the distance from the second principal plane P_2 with an infrared pyroelectric camera from Spiricon, model PyroCamIII. Due to the Brewster-cut geometry two focal points were observed. The thermal focal

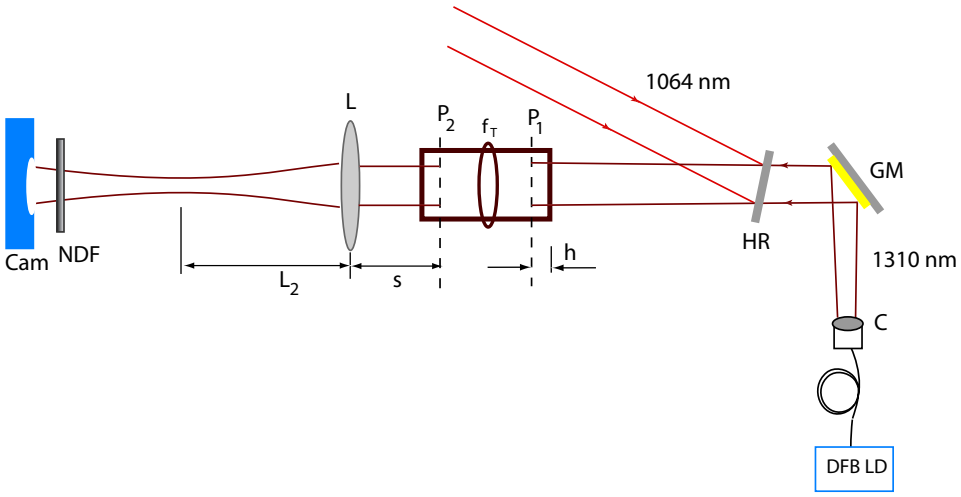

Figure 4.7: Experimental setup for measuring the thermal focal length with the pump-probe technique. The crystal is illustrated in the sagittal plane. The lens in the rod center represents the thermally induced lens. The optical components are as follows: DFB LD: distributed feedback laser diode, C: collimating optics, GM: gold coated mirror, HR: high reflectivity mirror at 1064 nm, h: distance between the principal plane and the end face of the crystal, P_1, P_2: principal planes, L: focusing lens, s: separation between the rod and the focusing lens, L_2: beam waist location, NDF: neutral density filters, Cam: IR camera.

length was determined independently in the tangential and sagittal plane by back propagation of the obtained values for waist location and Rayleigh length considering the location of the principal planes from the end of the crystal. For incident angle of 61.4° the principal planes were located at h_{tan}= 3 mm and h_{sag}= 10 mm from the end surface.

The thermal lensing of Cr^{4+}:YAG was investigated for different pump pulse energies and pulse repetition frequencies (PRF): 10 Hz with Surelite and 125 Hz and 250 Hz with the IBL pump laser. In all experiments the crystal temperature was set to 15 °C. The results obtained with the IBL pump laser have not been applied in the resonator calculations. However, these measurements are valuable for future design of chromium lasers, operating at high PRFs and are therefore presented in Appendix C.

Matrix methods were applied in order to calculate the thermal focal length. When the crystal was pumped with the Continuum laser at 10 Hz, weak thermal lensing was expected due to the low average pump power of 1.3 W. In order to bring the thermal focal points closer to the crystal, an additional focusing lens was placed immediately after the rod (lens L with focal length 700 mm in Fig. 4.7). The beam propagation after the system of rod–focusing lens was measured when the crystal was not pumped and again when it was pumped. If the crystal was not pumped, it was described by

a ray transfer matrix of medium with thickness l_{cr} and index of refraction n_0. In the presence of thermal lensing, the rod was viewed as a thick lens with focal length f_T and principle planes h_{sag} (or h_{tan}).

This method is illustrated in Fig. 4.8.

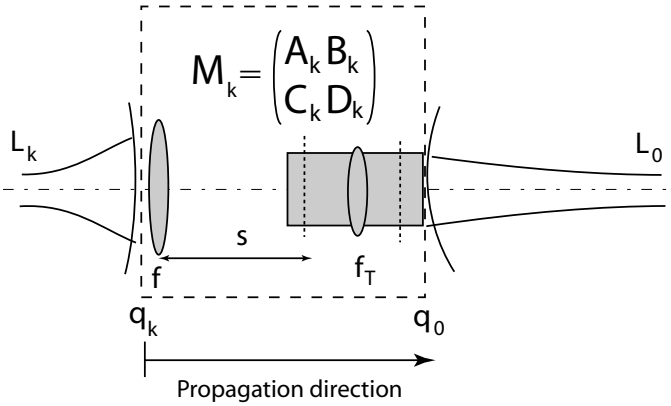

Figure 4.8: Matrix method for calculation of the thermal focal length. M_k: ray transfer matrix of the system lens-crystal, f and f_T: focal length of the lens and the thermal lens, respectively, s: separation, L_k and L_0: waist position of the incident and output beam, respectively, q_k and q_0: complex beam parameter of the incident and output beam, respectively.

For simplicity, the propagation direction is reversed and the incident beam becomes the output beam with parameter $q_0 = -L_0 + i\, z_0$. The measured beam after propagation through the crystal and the lens will be viewed as the incident beam with the parameter $q_k = L_k + i\, z_k$, $k = 1, 2$ (index 1 indicates "cold" crystal and 2 the pumped crystal). The ray transfer matrix of the system is

$$M_1 = \begin{pmatrix} 1 - s + l_{cr}/(n_0\, f) & s + l_{cr}/n_0 \\ 1/f & 1 \end{pmatrix} \tag{4.5}$$

for the unpumped case and

$$M_2 = \begin{pmatrix} 1 - s/f & s \\ -1/f - (1 - s/f)(1/f_T) & 1 - s/f \end{pmatrix} \tag{4.6}$$

in the presence of thermal lensing. The complex beam parameters q_k are transformed as

$$q_{0k} = \frac{A_k q_k + B_k}{C_k q_k + D_k},\ k = 1, 2. \tag{4.7}$$

The beam at the exit of the system M_1 and M_2 is the same also, $q_{01} = q_{02} = q_0$. The equations for the real and imaginary part of the complex parameter q_0 are solved for the thermal focal length.

The calculated thermal focal length was f_{sag}= 15 m and f_{tan}= 4.5 m. The relative error was estimated to 20 %. The ratio f_{sag}/f_{tan}=3.33 is less than the value 4.36 obtained with the tilted slab approximation (Eq. 2.41). Nonetheless, the experimental value is consistent with the approach used by Wagner et al. [160]. They have shown that f_{sag}/f_{tan} is smaller than the value predicted by the tilted slab approximation due to the non symmetrical temperature profile around the axis.

4.4 Resonator design

In order to design a dynamically stable resonator, the following parameters must be determined: radii of curvature R_1 , R_2 of the rear mirror and the output coupler, respectively, and their position L_1, L_2 with respect to the laser rod.

The calculations of a dynamically stable linear resonator are based on the formulae presented in Section 2.5. The mirror 1 on Fig. 2.3 is set to be the rear mirror and mirror 2 the output coupler. Here, only one laser rod is considered (for two-rod-resonator see Appendix D). Therefore, the matrix elements of M_1 and M_2 contain the set of parameters R_1 , L_1 and R_2 , L_2, respectively. By setting up the experiment one should remember that L_1 and L_2 are measured from the principal planes of the thermal lens (the rod) to the mirrors (see Section 2.5). Hereafter the values assigned to L_1 and L_2 are the distances from the principal planes in the tangential plane to the resonator mirrors. For all experiments, the laser rod was placed close to the rear mirror in order to better exploit the low-gain active medium [93] and reduce the effect of spatial hole burning [136]. Thus the fixed parameters were the laser wavelength in the center of the gain spectrum at 1450 nm, the measured thermal lens focal length f_T, and the desired mode radius at the rod $w_{3,0}$. Also, the back mirror was chosen to be flat ($R_1 \to \infty$). The possible resonator configurations can than be determined by varying the distance L_1 between the crystal and the rear mirror and calculating R_2 and L_2 of the output coupler so that the condition for dynamic stability is fulfilled. From this geometry, and from Eqs. 2.47 and 2.51 follows for the beam radius at the rod

$$\omega_{3,0}^2 = \frac{2\lambda}{\pi}|B_2 D_2|. \tag{4.8}$$

This result is inserted into Eqs. 2.42 and 2.50 and an expression for the product A_2D_2 is obtained. A_2D_2 is a function of the unknowns R_2 and L_2 just like the product $|B_2D_2|$ from Eq. 4.8. Thus, they can be solved as coupled equations for R_2 and L_2. There are four cases that must be investigated: two for $B_2D_2 > 0$ together with $\xi = \pm\sqrt{|uv|}$ and another two for $B_2D_2 < 0$ together with $\xi = \pm\sqrt{|uv|}$. The same calculations were performed independently for the thermal focal length in the other orthogonal plane.

The next step was to select the appropriate of all possible resonator configurations. This evaluation was based on the following requirements:

(i) The overall length of the resonator should not exceed 1.5 m.
(ii) The beam radii at the mirrors should be large enough to prevent optical damage at high pump energy.
(iii) The stability zones for both sagittal and tangential planes should have a common region where they overlap.
(iiii) The resonator should have low misalignment sensitivity.

If the result of the calculated configuration requires, for example, radius of curvature of the output coupler, which is in practice not acceptable, it can be substituted with the nearest commercially available standard curved mirror and the other resonator parameters adjusted in order to maintain dynamic stability of the resonator with sufficiently low misalignment sensitivity.

The laser rod used in these experiments had a radius of 3.5 mm. The laser beam, incident at the Brewster angle can thus have maximum radius of 2 mm. In order to keep the diffraction losses at the crystal's end surface low, the pump beam and the laser mode radii were limited to 1.6 mm (80 % of the maximum pump beam size) [54, 79].

By examining the possible resonators for a given mode size and thermal lensing the following relations were determined:
(i) Mode radius larger than 0.8 mm can be achieved with a very long dynamically stable resonator (longer than 2 m). Therefore, the experiments were performed with mode radius ranging from 0.5 mm to 0.8 mm and a maximum resonator length of 1.5 m.
(ii) Due to the long thermal lens focal length, the stability zones in the tangential and sagittal plane fully overlap. The mode radius in the sagittal plane was 0.01–0.05 mm larger than in the tangential plane and consequently the misalignment sensitivity was about 10–30 % higher.
(iii) A given mode size can be achieved in a short stable resonator with an output coupler of long focal length. Often these configurations are stable (see Eq. 2.46) but not dynamically stable in terms of Eq. 2.49 and have high misalignment sensitivity.

Suitable resonators, however, employing output couplers with standard radius of curvature (1 m, 2 m and 3 m) and sufficiently low misalignment sensitivity were found. The rear mirror was placed 0.1 m from the tangential reference plane of the crystal and the position of the output coupler was varied in order to obtain different mode sizes in the crystal.

The theoretical calculations for the mode radii at the crystal and the overall misalignment sensitivity in the tangential plane are plotted as a function of the distance L_2 in Fig. 4.9. Examples of stable but not dynamically stable resonators are the configurations represented with circled points in Fig. 4.9(a). It is apparent that, for a given output coupler, the mode size is proportional to the resonator length and the opposite is true for the misalignment sensitivity.

The stability zones and the misalignment sensitivity as a function of the thermal lens are shown in the next Fig. 4.10. The mode radius remains almost constant for

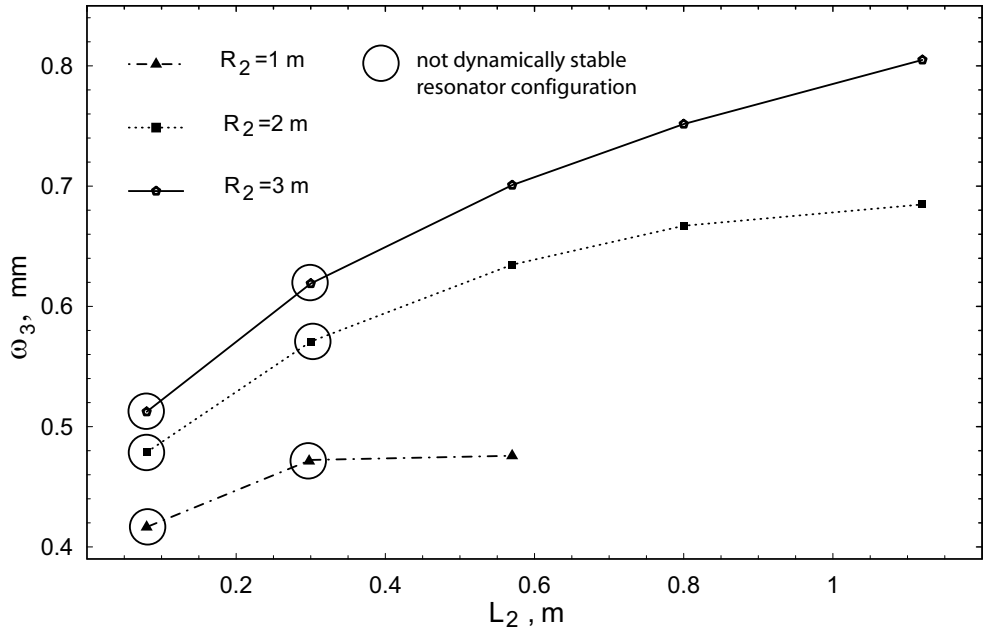

(a) Mode radius

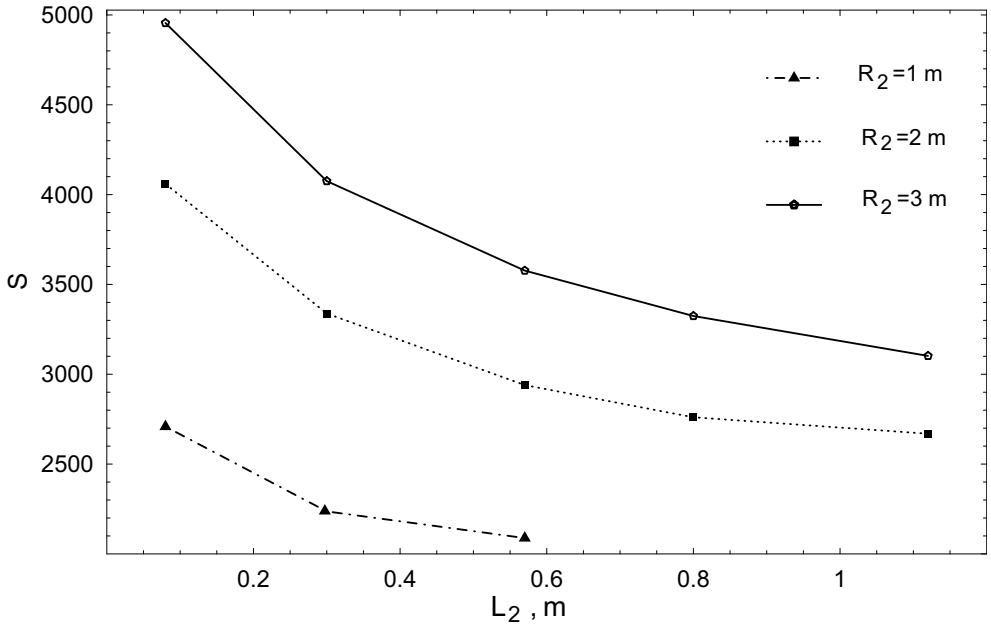

(b) Overall misalignment sensitivity

Figure 4.9: Mode radius and overall misalignment sensitivity in the tangential plane vs. the distance between the crystal and the output coupler, for output couplers with different radius of curvature R_2. The back mirror is flat and is placed at L_1=0.1 m from the crystal. The thermal lens has a focal length f_{tan}= 4.5 m.

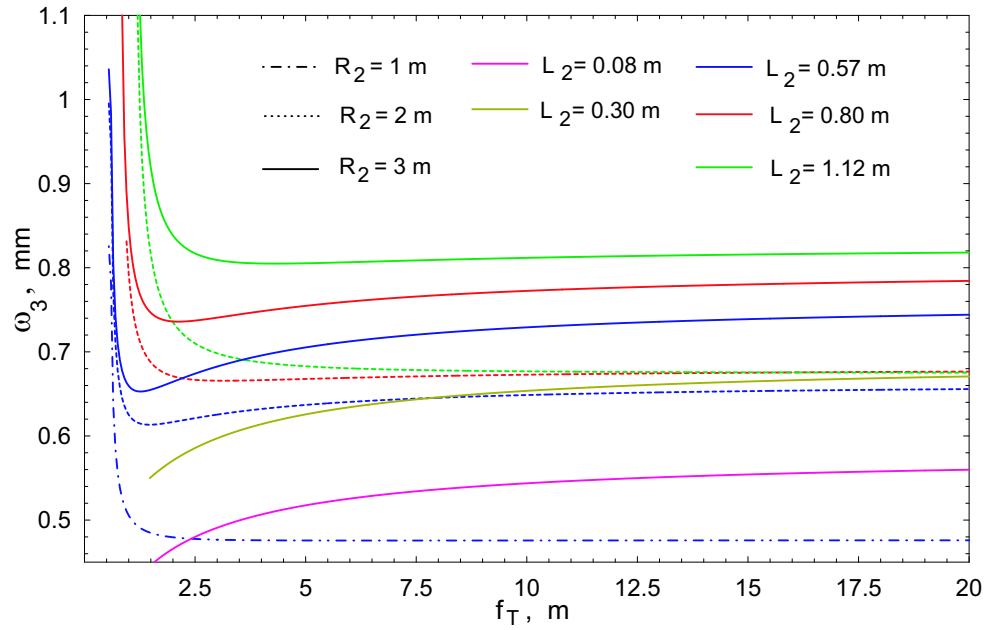

(a) Stability zones

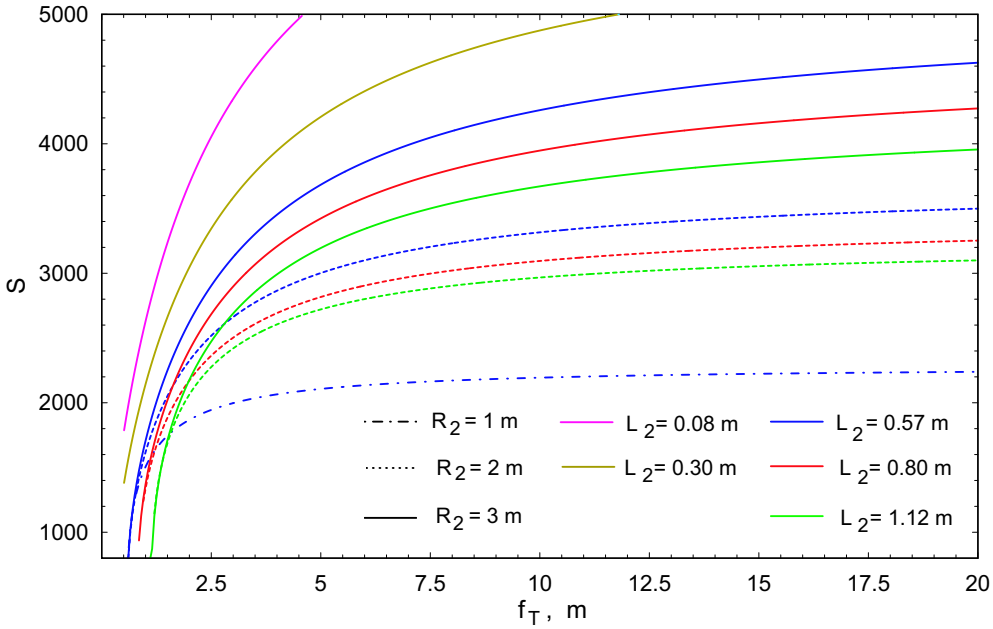

(b) Overall misalignment sensitivity

Figure 4.10: Mode radius and overall misalignment sensitivity as a function of the thermal focal length for different resonator configurations. For all cavities the rear mirror is flat and is placed at $L_1 = 0.1\,\mathrm{m}$ from the crystal. The radius of curvature R_2 and the position of the output coupler L_2 with respect to the crystal are indicated in the legend.

a large range of thermal focal lengths. For certain configurations, i.e R_2= 3 m, and L_2= 0.57 m, it is more sensitive to focal length fluctuations in the tangential plane. The perturbation of the mode size is relatively small and it is not expected to have significant impact on the laser performance.

For comparison, the stability zone and the misalignment sensitivity of the dynamically unstable resonators with output coupler R_2= 3 m, placed at 0.08 m and 0.3 m after the crystal, are also shown on these figures. Despite the fact that the mode radius is not at its minimum (see Eq. 2.49) it remains relatively insensitive to thermal length fluctuations in both tangential and sagittal planes. The sensitivity to mirror misalignment, on the other hand, is considerably higher and increases rapidly with increasing thermal focal length (Fig. 4.10(b)). These configurations deliver mode sizes at the rod, comparable to the dynamically stable resonator with R_2 = 1 m, L_2= 0.57 m and R_2 = 2 m, L_2= 0.57 m, respectively (see Fig. 4.9(a)). Therefore, their performances were compared experimentally (see Section 4.5).

The beam propagation of the fundamental mode in the resonator was calculated with the aid of ray transfer matrices as described in Section 2.3. The results are illustrated on Figs. 4.11–4.13. The origin of the x-axis is set at the rear mirror. The crystal is at position 0.1 m. It is assumed that the beam does not change by propagating through the crystal. For all resonators the beam waist in the sagittal plane is located at the rear mirror. In the tangential plane the waist is after the laser rod (except in the resonator L_2= 0.08 m, R_2= 2 m and 3 m). The half angle divergence for all configurations is under 1 mrad.

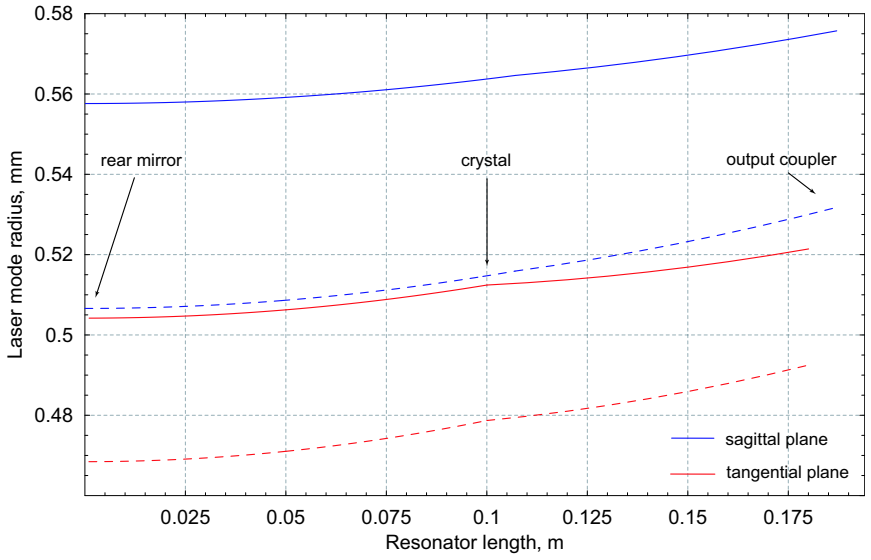

Figure 4.11: Propagation of the fundamental laser mode in a resonator with $R_1 \to \infty$, L_1= 0.1 m, L_2= 0.08 m. Dashed line: R_2= 2 m, solid line: R_2= 3 m. The position of the crystal and the resonator mirrors is indicated in the plot.

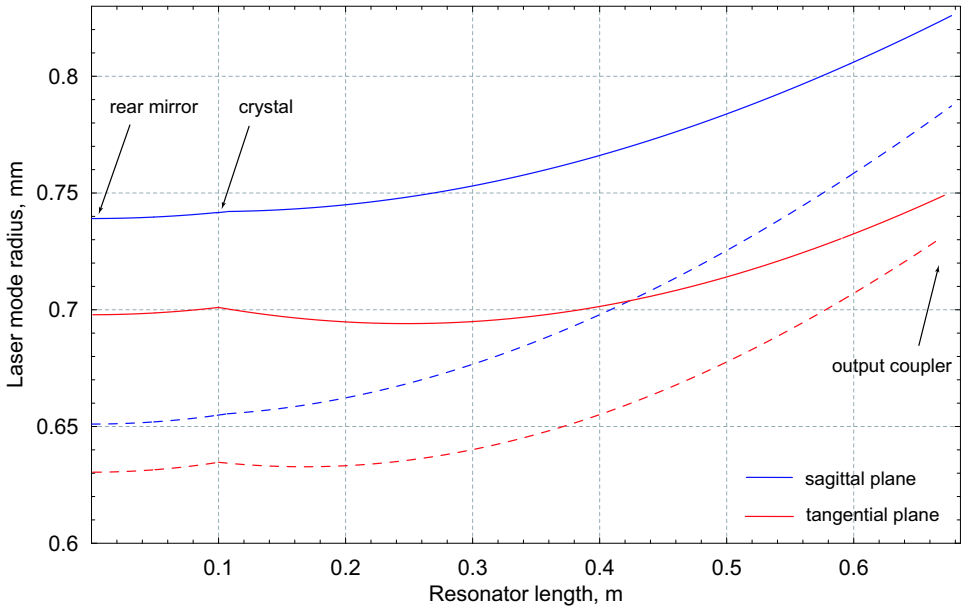

Figure 4.12: Propagation of the fundamental laser mode in a resonator with $R_1 \to \infty$, $L_1 = 0.1\,\mathrm{m}$, $L_2 = 0.57\,\mathrm{m}$. Dashed line: $R_2 = 2\,\mathrm{m}$, solid line: $R_2 = 3\,\mathrm{m}$. The position of the crystal and the resonator mirrors is indicated in the plot.

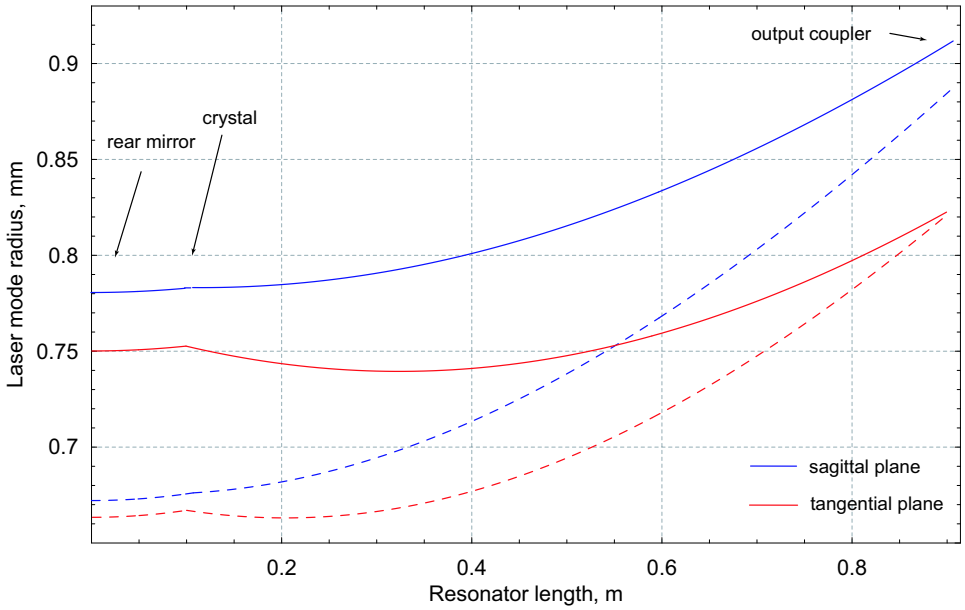

Figure 4.13: Propagation of the fundamental laser mode in a resonator with $R_1 \to \infty$, $L_1 = 0.1\,\mathrm{m}$, $L_2 = 0.8\,\mathrm{m}$. Dashed line: $R_2 = 2\,\mathrm{m}$, solid line: $R_2 = 3\,\mathrm{m}$. The position of the crystal and the resonator mirrors is indicated in the plot.

4.5 Experimental optimization of the laser performance

This section presents the experimental data obtained with a one-rod resonator. The influence of the pump beam diameter, laser mode size and temperature of the crystal on the output pulse energy was investigated. These parameters were optimized experimentally for maximum output energy at the maximum pump level of 130 mJ. A discussion of the experimental results is provided at the end of the section.

The experimental set up is illustrated in Fig. 4.14. The crystal was pumped through the rear resonator mirror DC with high transmission at the pump wavelength and high reflectivity (>99.8 %) for the emission wavelength region 1400–1500 nm. The transmitted pump radiation exited the resonator at a slightly different angle than the generated laser beam (due to dispersion) and it was blocked with a beam dump. The output energy was measured with an Ophir energy meter (PE50BB-DIF). The pulse width and the build up time were measured with a high-speed Silicon (Si) photo detector (Thorlabs, DET410). An interference filter with transmission maximum at 1450 nm was placed in front of one detector in order to separate the laser from the pump pulse. The pulse duration is defined as the full width at half maximum (FWHM). The build up time is determined as the time from the leading edge of the pump pulse at level 50 % of the maximum to the leading edge at 50 % level of the laser pulse.

As it was shown in Section 4.2, the pump efficiency is reduced due to the saturation of the absorption, which is pump power dependent (Fig. 4.6). In order to avoid the nonlinear behavior of absorbed versus pump energy, all power curves are plotted as a function of the absorbed energy and not the incident energy. Also, the conversion efficiency is defined as the ratio of output energy to the absorbed pump energy.

4.5.1 Optimization of the mode size

All measurements presented in this subsection were performed with a pump beam radius 1.05×1.1 mm at the surface of the crystal. This radius was obtained with the recollimating lens L_5 with focal length of 1 m (Fig. 4.14). The temperature of the crystal was stabilized to 15 °C. The resonators were aligned to provide maximum output energy for the highest pump energy of 130 mJ. The experimental results are summarized in Figs. 4.15– 4.16(b) for increasing radius of the fundamental laser mode from 0.45 mm up to 0.8 mm.

In Fig. 4.15 are shown the output curves of two resonator configurations with mode radii 0.48×0.5 mm and 0.51×0.56 mm (tangential × sagittal plane) for output couplers with radii of curvature 1 m and 3 m, respectively. Both performed very similarly: the output energy increased linearly with the pump energy (up to 60–65 mJ absorbed energy) and then saturated. As it was pointed out earlier, the shorter res-

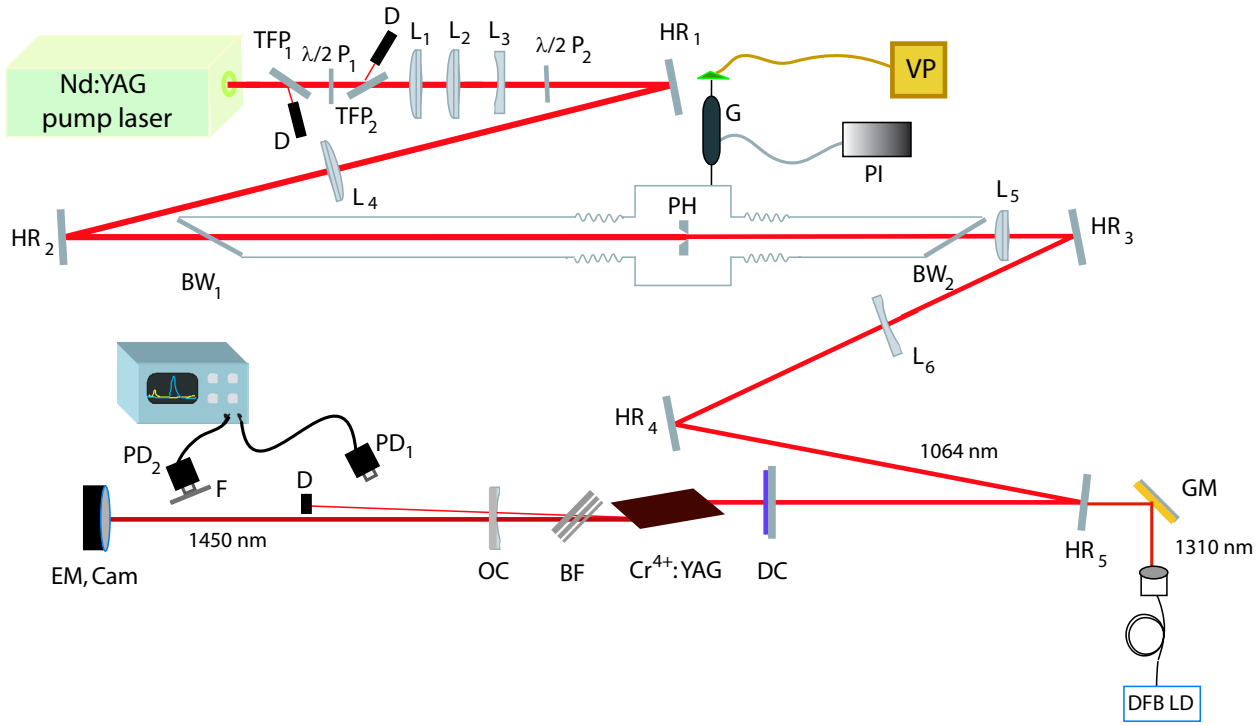

Figure 4.14: Experimental setup of Cr^{4+}:YAG laser. TFP_1, TFP_2: Thin film polarizers at Brewster angle, $\lambda/2P_1, \lambda/2P_2$-half-waveplates, D: beam dump, L_1: cylindrical lens, L_2: plano-convex lens, L_3: plano-concave lens, $HR_1 - HR_5$: high reflectivity mirrors for 1064 nm,L_4: focusing lens for the spatial filter, BW_1, BW_2: fused silica windows at Brewster angle, PH: pinhole, G: Gauge, PI: pressure indicator, VP: vacuum pump, L_5: recollimating lens,L_6: plano-concave lens, GM: gold coated mirror, DFB LD: distributed feedback laser diode, DC: dichroic mirror, BF: birefringent filter, OC: output coupler, EM: energy meter, F: interference filter, PD_1, PD_2: photo detectors.

onator does not satisfy the condition for dynamical stability (Eq. 2.49). Nevertheless, the resonator was easy to align and had stable operation. This behavior is attributed to the fact that the thermal focal length was sufficiently stable and consequently the mode size.

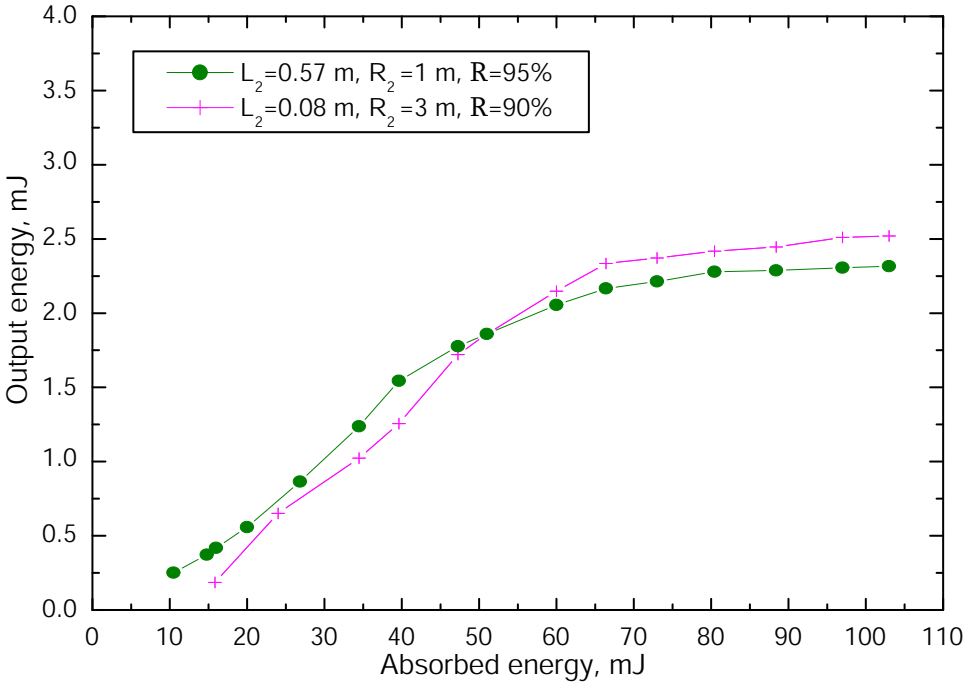

Figure 4.15: Output energy vs. absorbed pump energy obtained with resonators with radius of the fundamental mode in the range 0.45 mm to 0.56 mm. The resonators were comprised of a flat rear mirror placed at $L_1 = 0.1$ m from the crystal and an output coupler as indicated in the legend. The temperature of the crystal was 15 °C. The pump beam diameter was 2.0×2.1 mm.

The output energy was increased by using resonators with larger mode radii from 0.63×0.65 mm ($R_2 = 2$ m and $L_2 = 0.57$ m) to 0.7×0.74 mm ($R_2 = 3$ m and $L_2 = 0.57$ m) (see Fig 4.16(a)). For output coupling of 10 %, two maxima in the output energy were observed followed by saturation. This behavior can be explained with the mode structure of the laser beam. The beam profile was not observed during these experiments but later investigations with larger pump beam size showed that higher order modes start to oscillate from absorbed pump energy around 60–70 mJ depending on the resonator configuration (see Subsection 4.6.3). This is $0.8 - 0.9$ J/cm^2 which corresponds to 30–40 mJ absorbed energy in the case of 2-mm-pump beam. It is possible to align the resonator for operation at the fundamental mode only at the expense of output energy (see Figs. 4.41 and 4.42). Again, the dynamically unstable resonator ($R_2 = 3$ m, $L_2 = 0.3$ m) performed just as well as the stable configuration with equiv-

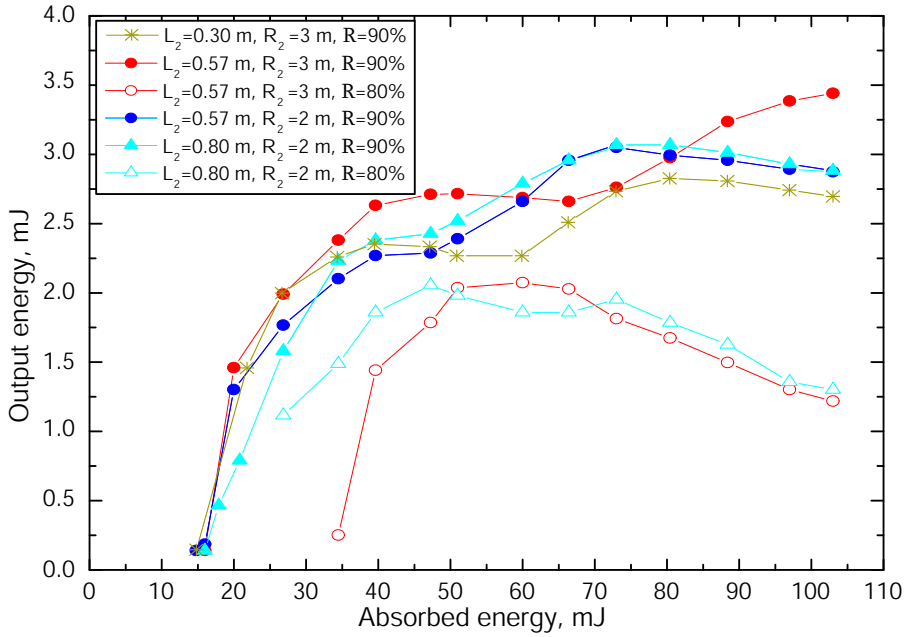

(a) Fundamental mode radius in the range 0.6 mm to 0.7 mm

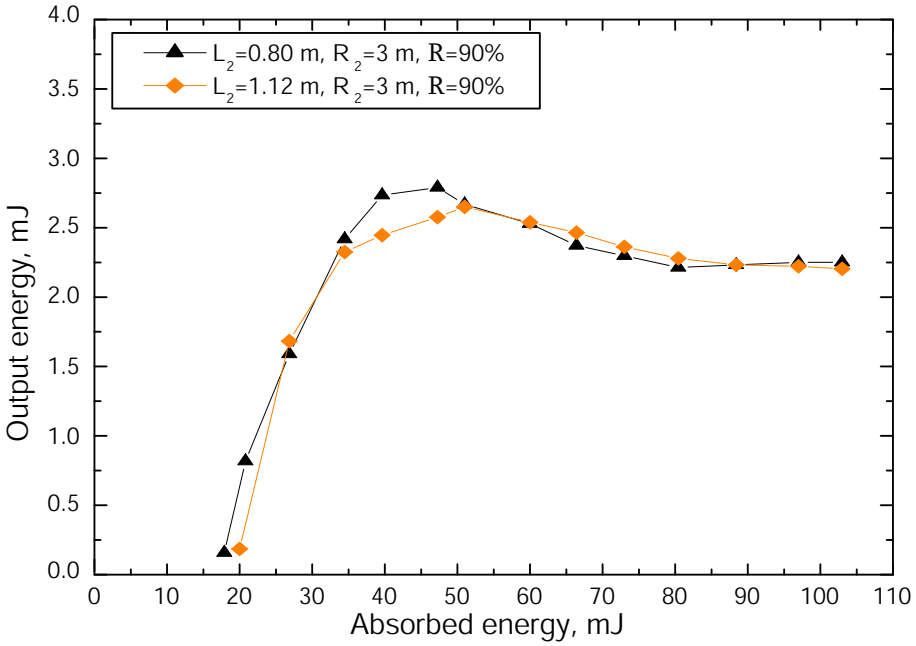

(b) Fundamental mode radius in the range 0.7 mm to 0.82 mm

Figure 4.16: Output energy vs. absorbed pump energy obtained with resonators with radius of the fundamental mode in the range 0.6 mm to 0.82 mm. The resonators were comprised of a flat rear mirror placed at $L_1 = 0.1$ m from the crystal and an output coupler as indicated in the legend. The temperature of the crystal was 15 °C. The pump beam diameter was 2.0×2.1 mm.

alent mode size (R_2= 2 m, L_2= 0.57 m). Fig. 4.16(a) also indicates that 20 % output coupling was too high and as a consequence the efficiency of the laser decreased.

In Fig. 4.16(b) are plotted the power curves for two configurations with mode radius 0.75×0.78 mm and 0.80×0.82 mm. Despite the larger mode size, the laser performance was not improved.

The best conversion efficiency of 7.5 % was obtained for low pump energy with the resonator L_2= 0.57 m, and R_2= 3 m (Fig. 4.17). For the maximum pump energy, the conversion efficiency decreased by more than a factor of two.

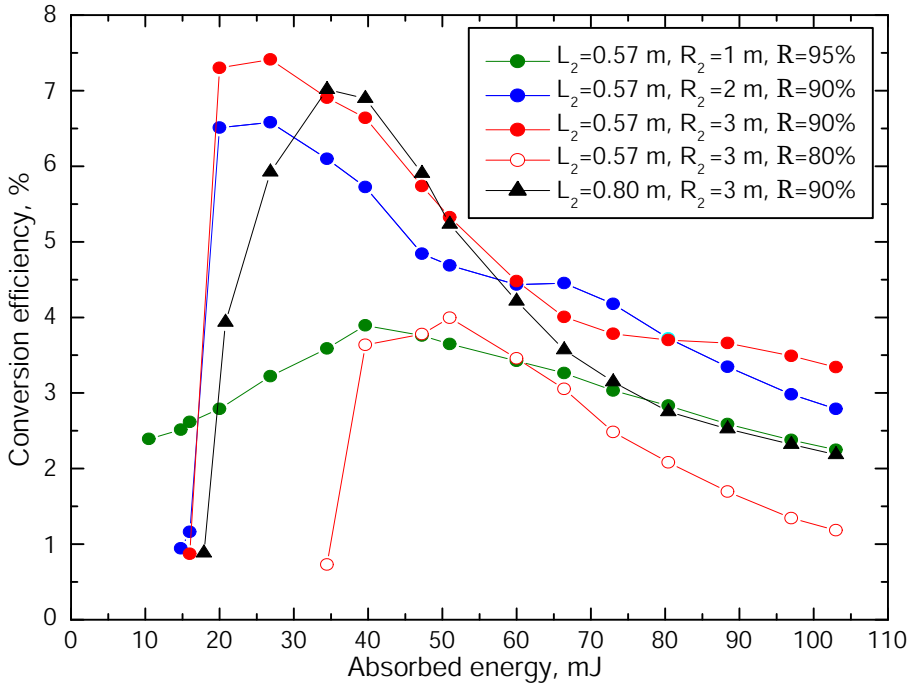

Figure 4.17: Conversion efficiency for various resonator configurations using flat rear mirror placed at L_1= 0.1 m from the crystal and an output coupler as indicated in the legend. The temperature of the crystal was 15 °C. The pump beam diameter was 2.0×2.1 mm.

The laser pulse duration and the build up time were measured simultaneously with the output power. As expected (see Eq. 2.13), shorter laser pulses were obtained with the shorter cavities (see Fig. 4.18). Also, resonators with the same length, only different radius of curvature of the output coupler, had approximately the same build up time and pulse duration (see Fig. 4.19). Both parameters increased when the transmission of the output coupler was changed to 20 % (Fig. 4.20).

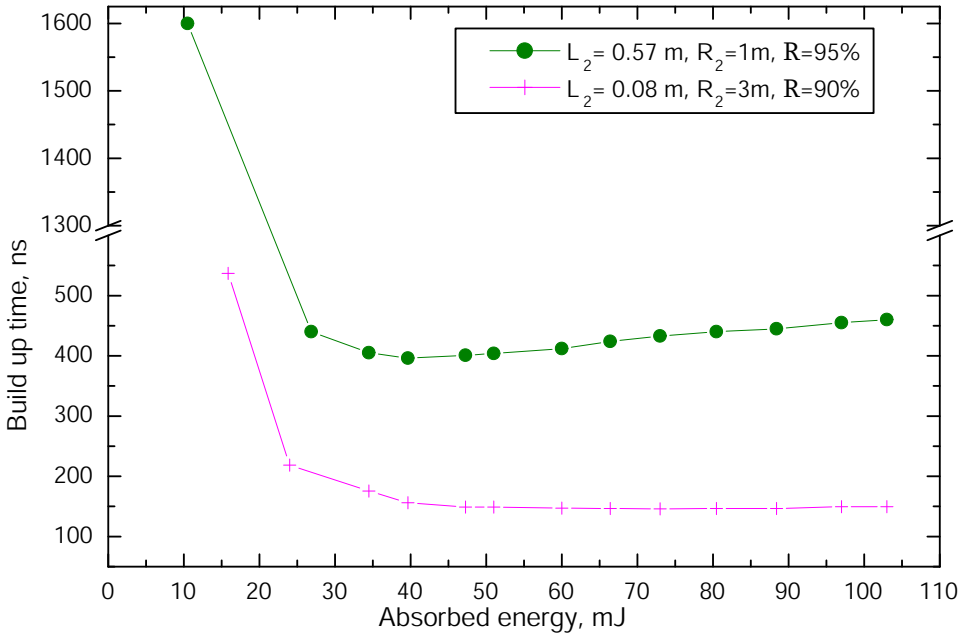

(a) Build up time

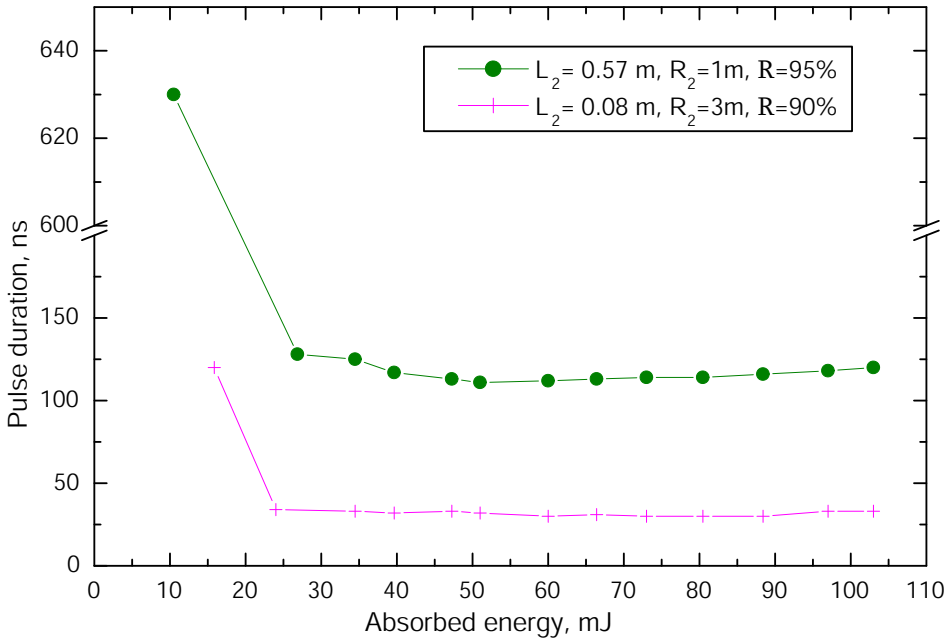

(b) Pulse width

Figure 4.18: Build up time and pulse width obtained with resonators with radius of the fundamental mode in the range 0.45 mm to 0.56 mm. The resonators were comprised of a flat rear mirror placed at $L_1 = 0.1$ m from the crystal and an output coupler as indicated in the legend. The temperature of the crystal was 15 °C. The pump beam diameter was 2.0×2.1 mm.

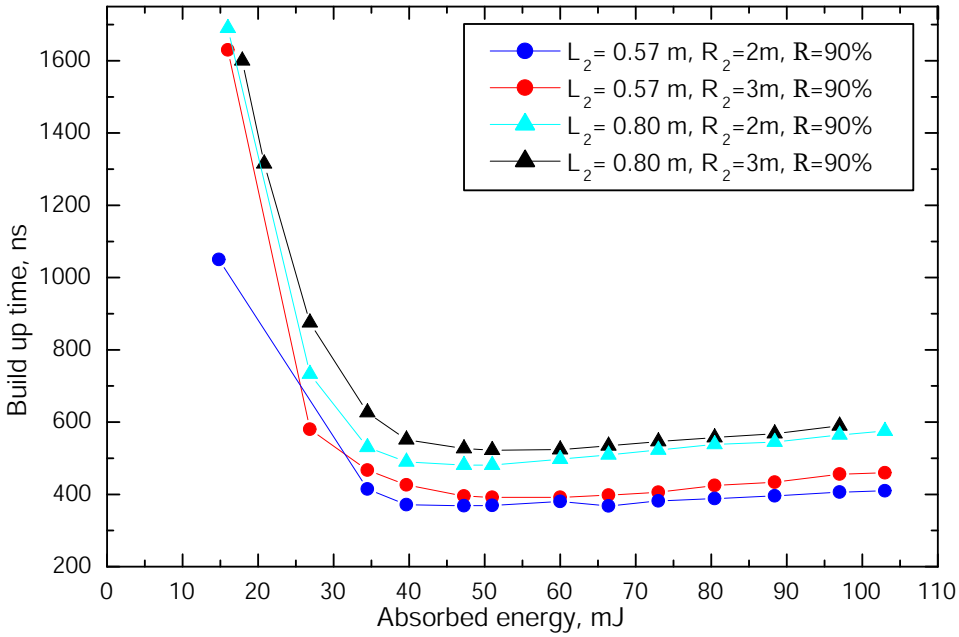

(a) Build up time

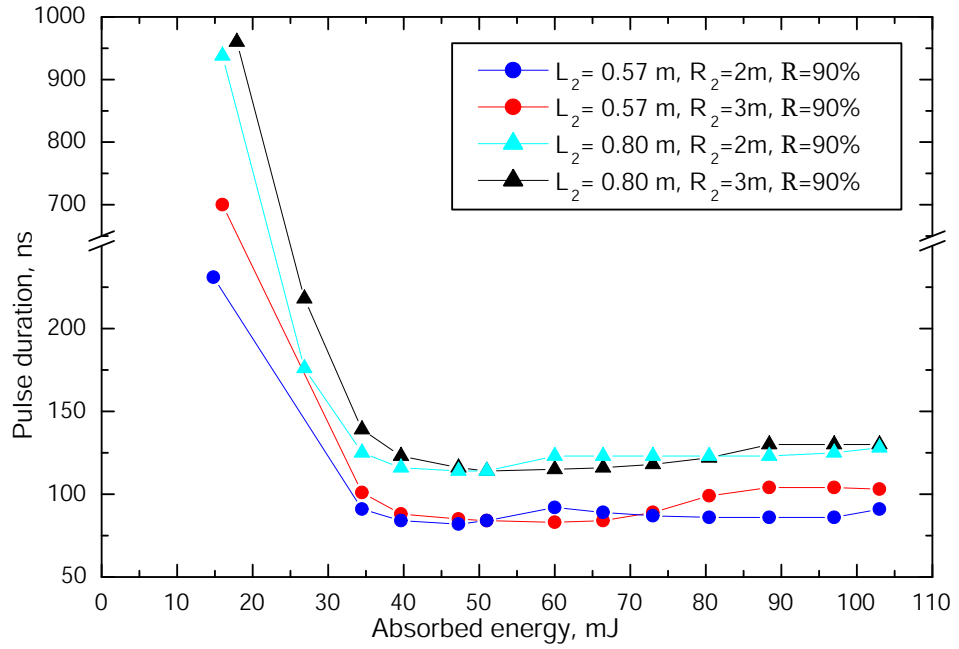

(b) Pulse width

Figure 4.19: Build up time and pulse width obtained with resonators with radius of the fundamental mode in the range 0.6 mm to 0.82 mm. The resonators were comprised of a flat rear mirror placed at $L_1 = 0.1$ m from the crystal and an output coupler as indicated in the legend. The temperature of the crystal was 15 °C. The pump beam diameter was 2.0×2.1 mm.

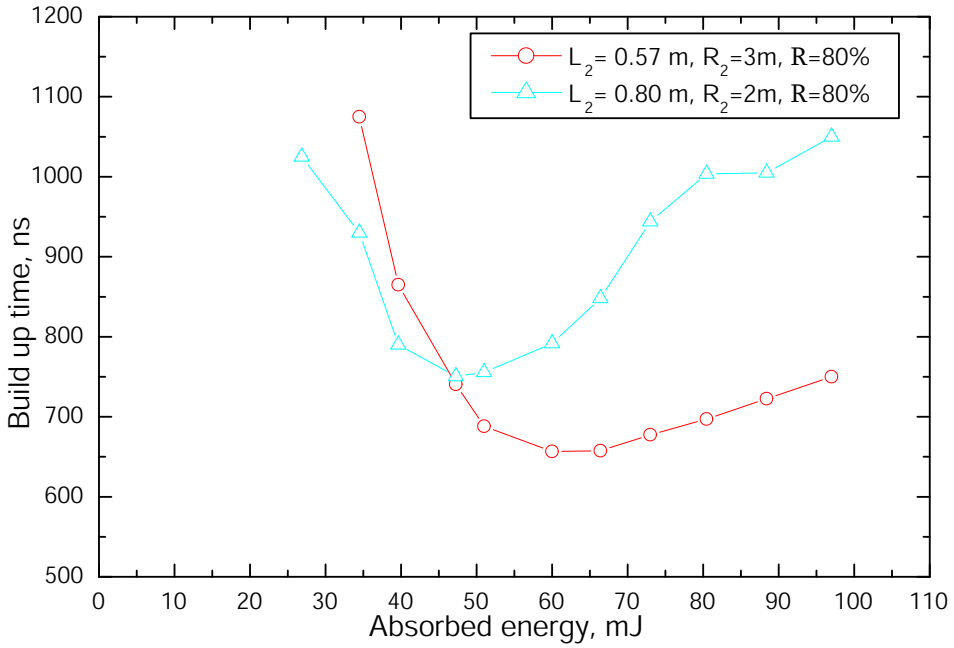

(a) Build up time

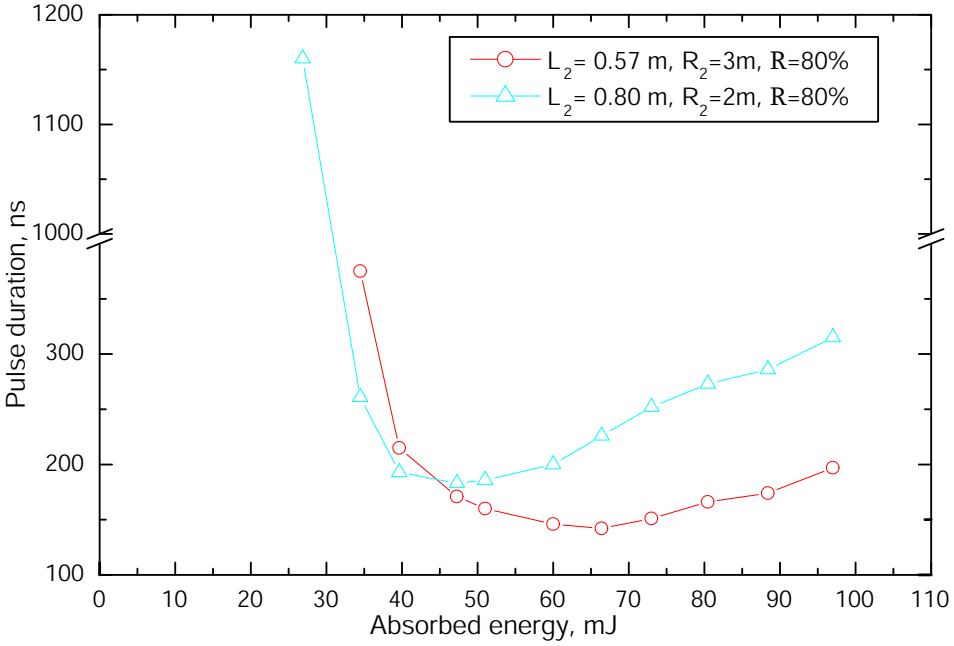

(b) Pulse width

Figure 4.20: Build up time and pulse width obtained with resonators with radius of the fundamental mode in the range 0.75 mm to 0.82 mm. The resonators were comprised of a flat rear mirror placed at $L_1 = 0.1$ m from the crystal and an output coupler as indicated in the legend. The temperature of the crystal was 15 °C. The pump beam diameter was 2.0×2.1 mm.

4.5.2 Optimization of the pump beam diameter

Further optimization of the laser performance was achieved by enlarging the pump beam radius at the crystal to 1.5×1.6 mm in x- and y-plane, respectively. This size was obtained with a new recollimating lens of the vacuum spatial filter L_5 with focal length 0.7 m and an additional plano-concave lens L_6 with f=–1 m placed at 0.33 m after L_5 (see Fig. 4.14). The beam in the crystal was almost collimated. Due to the lower pump energy density the transmission of the pump wavelength was reduced to 12 % at 130 mJ pump energy (see Fig. 4.6).

Resonators from each group with similar mode size and performance presented in the previous subsection (Figs. 4.15 and 4.16) were tested again with the new pump beam size. The experimental results are presented in Fig. 4.21. The output coupling in all resonator configurations was 10 %.

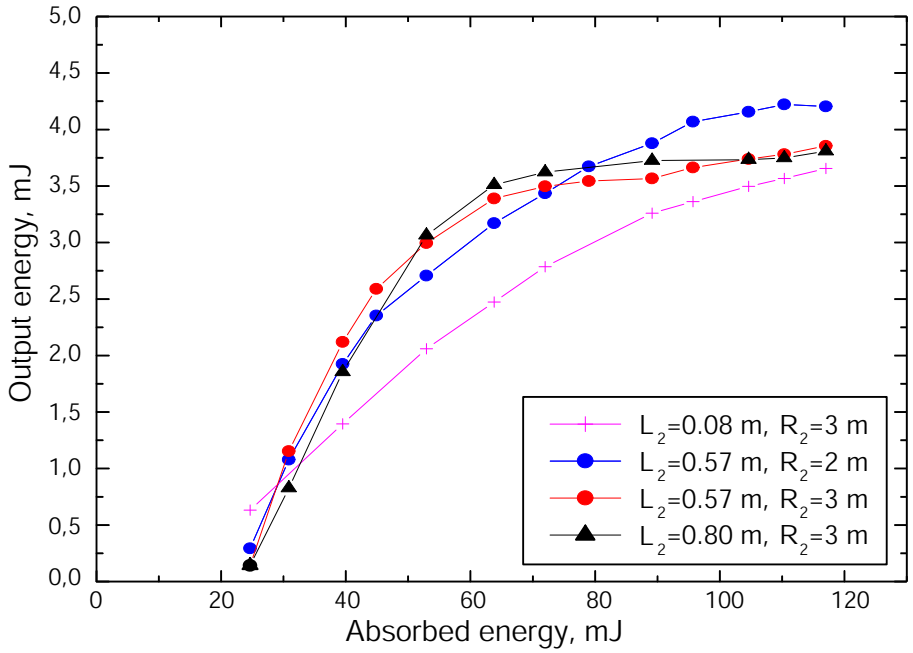

Figure 4.21: Power curves obtained with resonators with radius of the fundamental mode in the range 0.45 mm to 0.8 mm. The resonators were comprised of a flat rear mirror placed at $L_1 = 0.1$ m from the crystal and an output coupler as indicated in the legend and $\mathcal{R} = 90$ %. The temperature of the crystal was 15 °C. The pump beam diameter was 3.0×3.2 mm.

Compared to the case with smaller pump beam radius, the laser threshold slightly increased approaching 25 mJ. Again, full saturation of the output energy was observed but for higher pump energy. Maximum output energy of 4.2 mJ was achieved with a resonator with output coupler $R_2 = 2$ m and $L_2 = 0.57$ m. The configurations with output coupler $R_2 = 3$ m and lengths $L_2 = 0.57$ m and $L_2 = 0.8$ m performed the same

and unlike when pumped with a 2 mm diameter beam (see. Fig. 4.16). The reason for the difference is most likely due to the generation of different order modes with the resonator with $L_2 = 0.57$ m.

The conversion efficiency was improved for the entire range of pump energies for the shortest resonator ($L_2 = 0.08$ m) (Fig. 4.22). In the longer resonators, better conversion efficiency was obtained only for high pump energies.

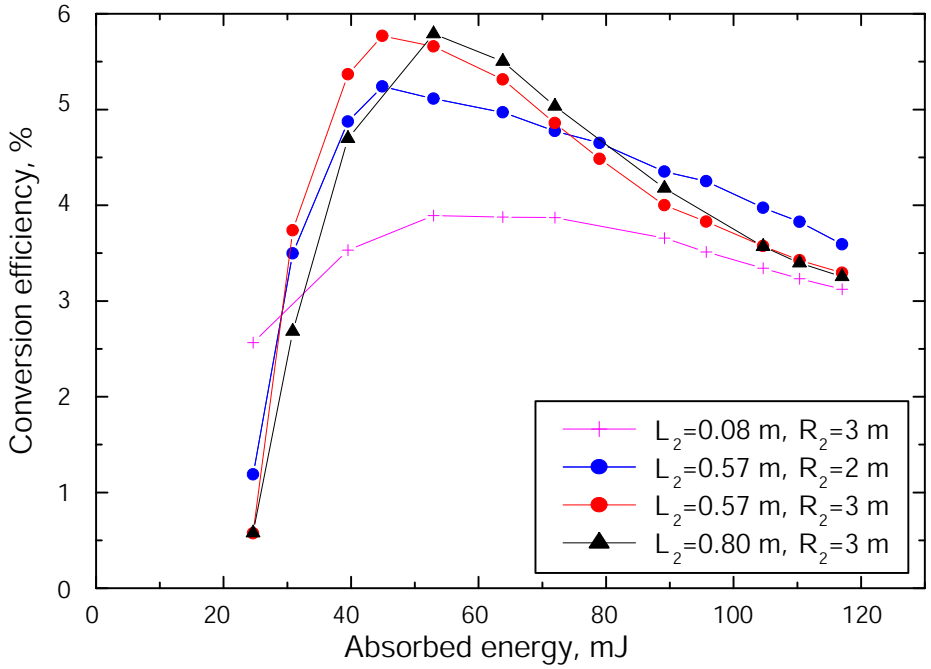

Figure 4.22: Conversion efficiency obtained with resonators with radius of the fundamental mode in the range 0.45 mm to 0.8 mm. The resonators were comprised of a flat rear mirror placed at $L_1 = 0.1$ m from the crystal and an output coupler as indicated in the legend and $\mathcal{R} = 90\,\%$. The temperature of the crystal was 15 °C. The pump beam diameter was 3.0×3.2 mm.

The pulse width and the build up time were also measured (Fig. 4.23). Compared to the case with 2-mm pump beam, the build up time and the pulse duration decreased by about 18 % and 12 % in average, respectively. This pulse duration and the absence of after pulses make this laser suitable as a laser transmitter for a lidar.

The laser performance was improved with the 3-mm pump beam. Therefore, all experiments that follow were performed with this pump beam size.

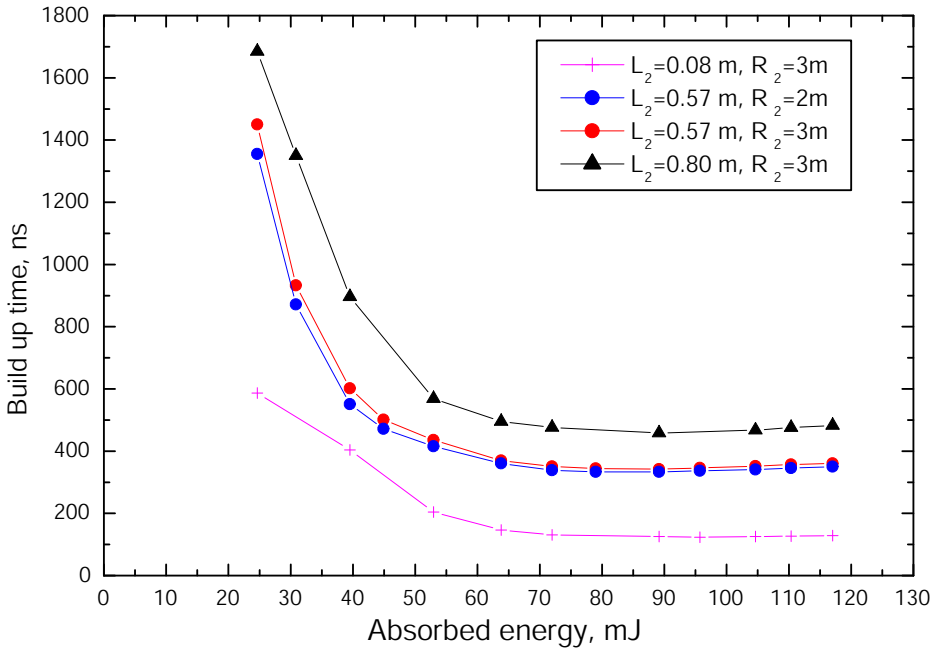

(a) Build up time

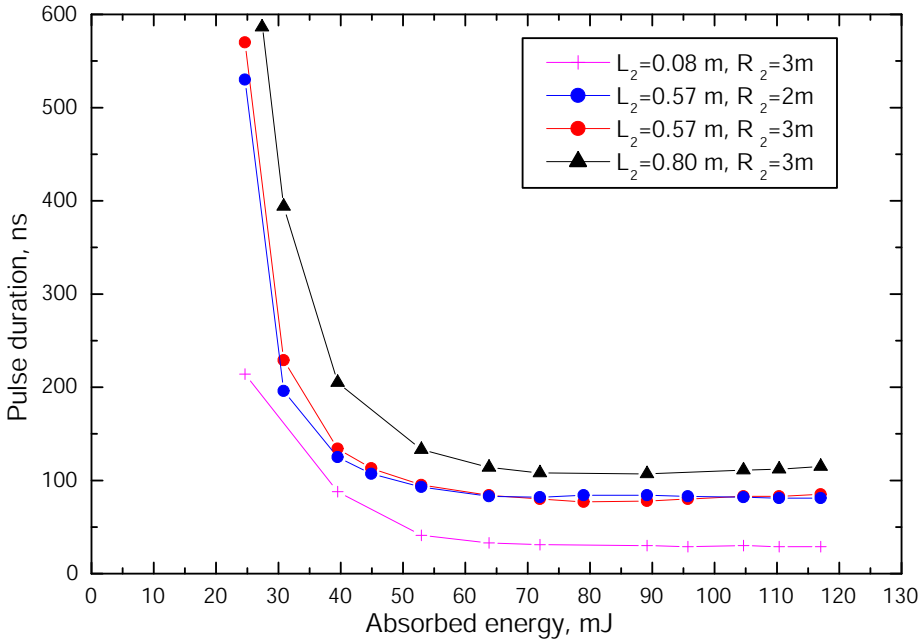

(b) Pulse width

Figure 4.23: Build up time and pulse width obtained with resonators with radius of the fundamental mode in the range 0.45 mm to 0.8 mm. The resonators were comprised of a flat rear mirror placed at $L_1 = 0.1$ m from the crystal and an output coupler as indicated in the legend and $\mathcal{R} = 90\,\%$. The temperature of the crystal was 15 °C. The pump beam diameter was 3.0×3.2 mm.

4.5.3 Optimization of the temperature of the crystal

In the next set of experiments the impact of the temperature of the crystal T on the laser efficiency was investigated.

First, the transmission of the pump radiation was measured for the temperature interval of 5 °C to 40 °C (see Fig. 4.24). The pump energy was kept constant while the temperature of the crystal was changed. The transmission variation was $\leq 2\,\%$ for the entire range of pump pulse energy. Okhrimchuk and Shestakov [113] have also demonstrated that the integrated absorption over the spectral region of 770–1250 nm is constant for temperatures of the crystal between 0 °C and 27 °C.

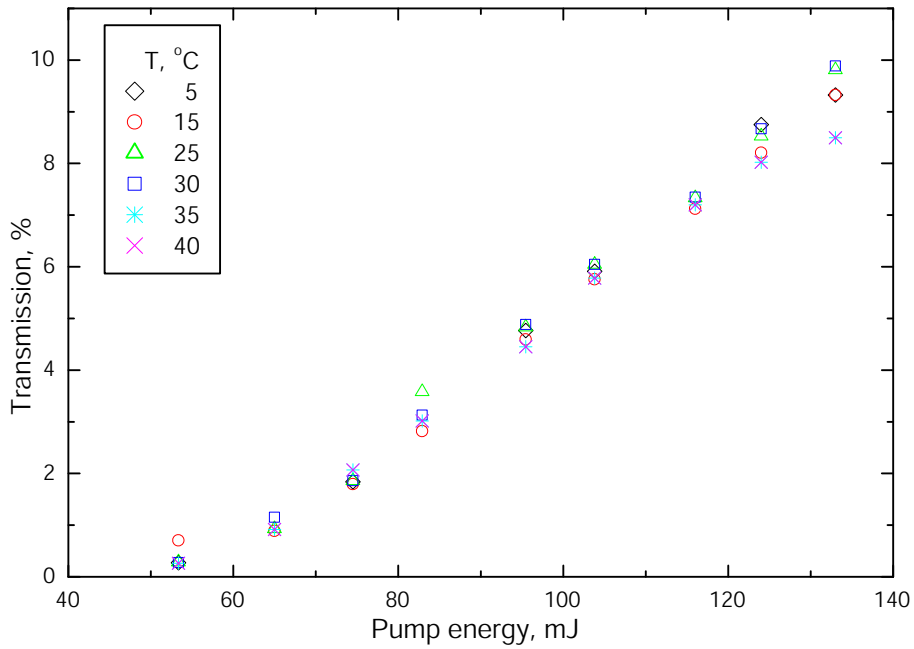

Figure 4.24: Transmission of the pump radiation as a function of the pump energy for different temperature of the crystal. The pump beam size was 3.0×3.2 mm.

The influence of T on the laser output energy was investigated for different pump levels in the resonator configuration $L_2 = 0.57$ m, $R_2 = 3$ m, $\mathcal{R}$=90 % . The resonator was aligned for maximum output energy at $T = 15$ °C. The alignment was not adjusted during the measurement. The output energy was measured for a given pump energy and a set of controlled temperatures of the crystal. When a new T was set on the temperature controller, a sudden change of the output energy was observed due to transient variations of the temperature profile in the crystal. In a few seconds the temperature of the crystal stabilized and the output energy reached a stationary value. The experimental results were reproducible in both directions of temperature change– increase and decrease. In order to evaluate if the alignment was temperature sensitive, the same measurement was repeated for the maximum pump energy and

this time the resonator mirrors were adjusted for every setting of T. The resonator mirror mounts had micrometer screws for fine-tuning and positioning readout (see Fig. 4.37) which permitted returning the mirrors to the original position. It was found that the same alignment of the resonator was optimal for all temperatures.

Fig. 4.25 shows the output energy as a function of the temperature of the crystal T for absorbed energy 54, 72, 89, and 115 mJ. It is evident that the optimal temperature is a function of the incident energy. For low pump energies, the laser efficiency can be improved by cooling the crystal. For high pump energy, on the other hand, keeping the crystal at or above room temperature results in a higher output energy.

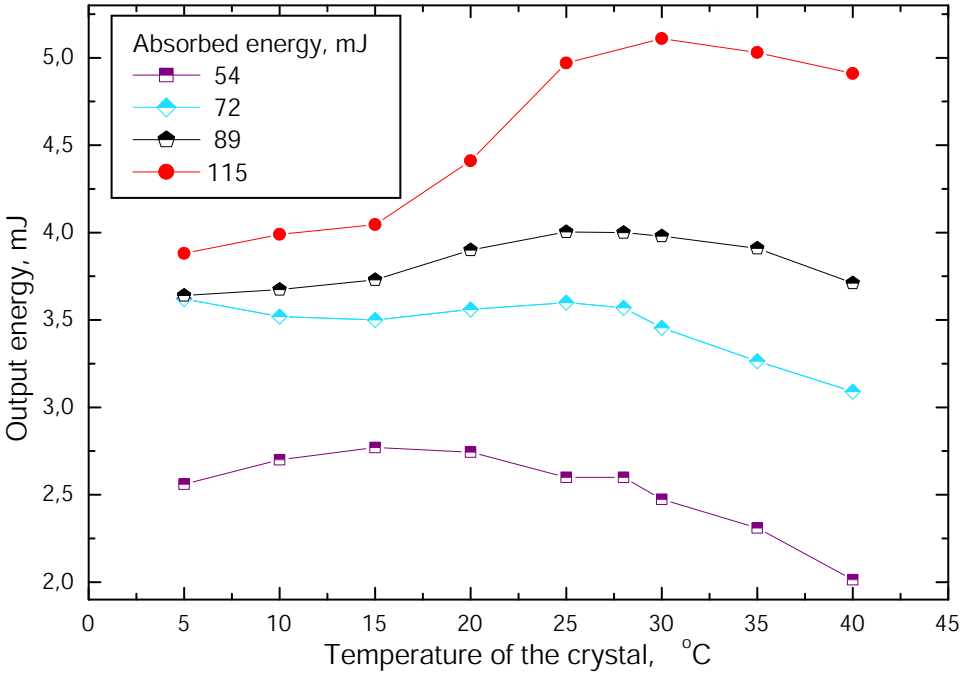

Figure 4.25: Output energy vs. temperature of the crystal for different absorbed pump energies. The resonator had a flat rear mirror placed at distance $L_1 = 0.1$ m and an output coupler $R_2 = 3$ m, $\mathcal{R}$=90 % at $L_2 = 0.57$ m from the crystal. The pump beam diameter was 3.0×3.2 mm.

The laser pulse duration and the build-up time for this arrangement are presented in Figs. 4.26 and 4.27. The pulse length variation was 2–6 ns for absorbed energies of 72–115 mJ and 30 ns for 54 mJ. For the maximum absorbed energy the pulse length decreased with the temperature. The build up time for absorbed energy 72–115 mJ decreased about 25 ns by increasing the temperature of the crystal from 5 °C to 40 °C. For the lowest absorbed energy, the build up time had a different behavior: it decreased when the temperature changed from 5 °C to 20 °C and increased again for $T = 30 - 40$ °C.

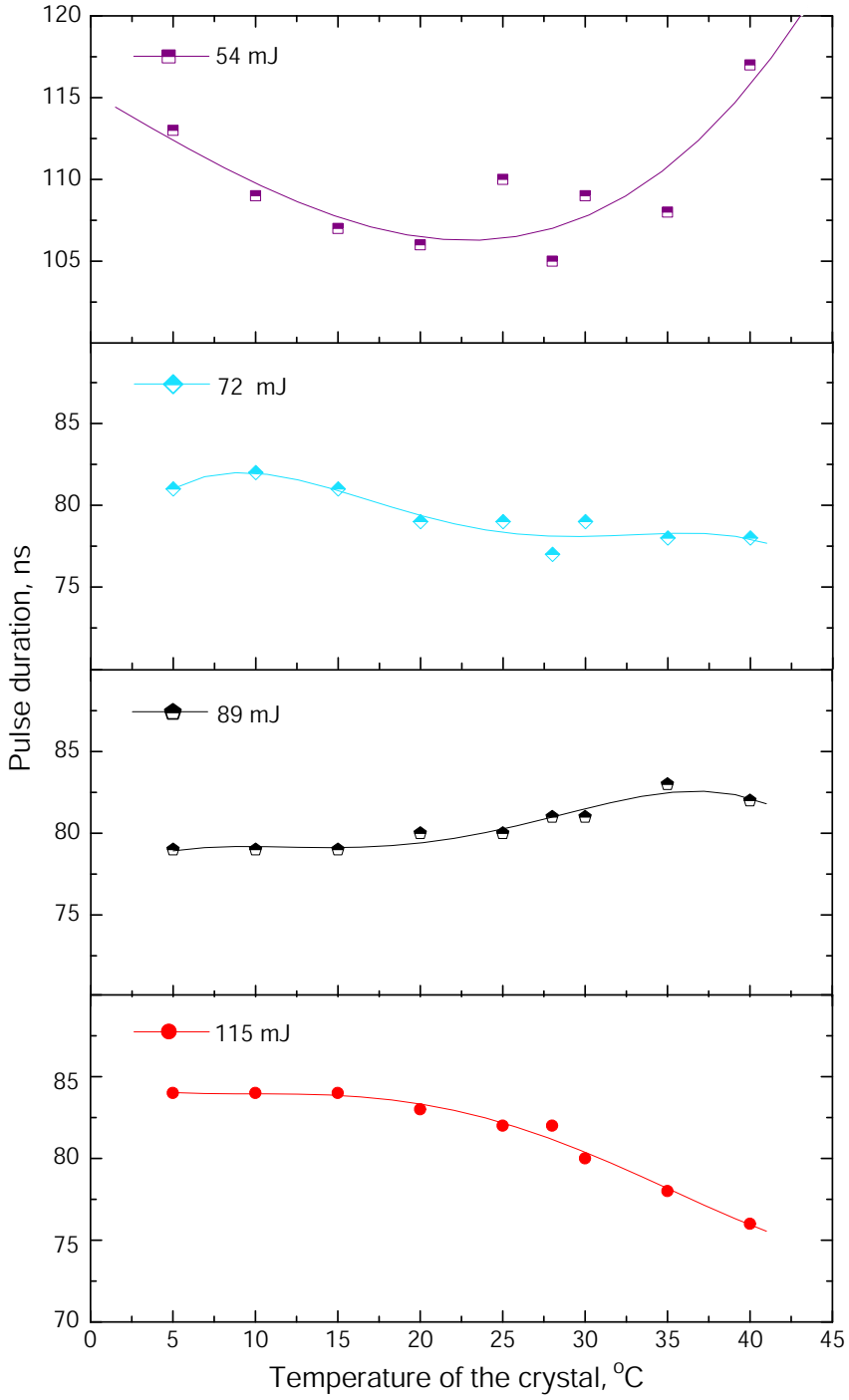

Figure 4.26: Laser pulse duration vs. temperature of the crystal for different absorbed pump energies. The resonator had a flat rear mirror placed at distance $L_1 = 0.1\,\mathrm{m}$ and an output coupler $R_2 = 3\,\mathrm{m}$, $\mathcal{R}$=90 % at $L_2 = 0.57\,\mathrm{m}$ from the crystal. The pump beam diameter was $3.0 \times 3.2\,\mathrm{mm}$. The symbols represent the measured values and the solid line the polynomial fit to the experimental data.

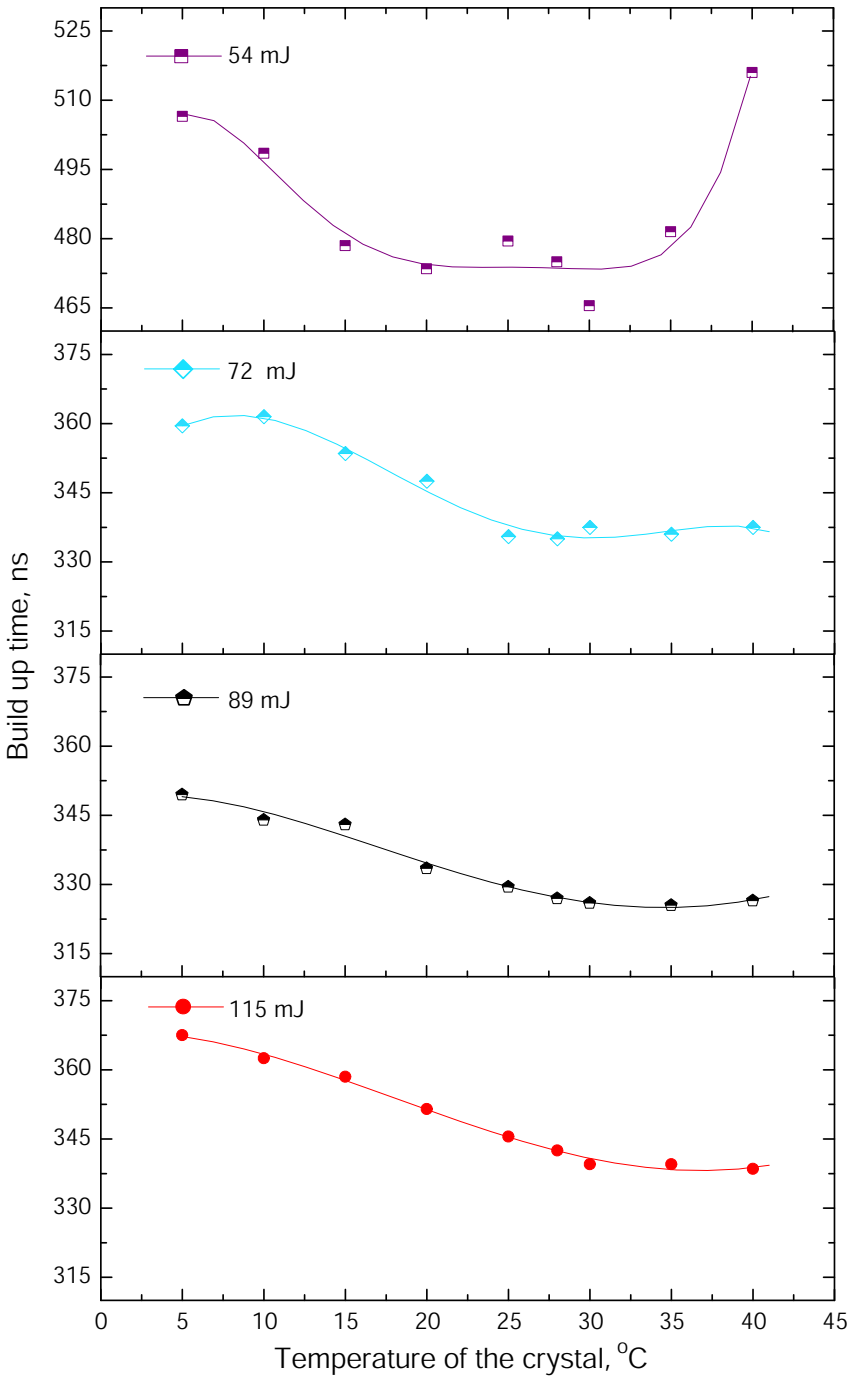

Figure 4.27: Build up time vs. temperature of the crystal for different absorbed pump energies. The resonator had a flat rear mirror placed at distance $L_1 = 0.1\,\mathrm{m}$ and an output coupler $R_2 = 3\,\mathrm{m}$, $\mathcal{R}$=90 % at $L_2 = 0.57\,\mathrm{m}$ from the crystal. The pump beam diameter was $3.0 \times 3.2\,\mathrm{mm}$. The symbols represent the measured values and the solid line the polynomial fit to the experimental data.

In order to obtain more laser output energy, the temperature of the crystal was optimized for the maximum pump energy of 130 mJ. The optimal T was different for the different resonator configurations (Fig. 4.28).

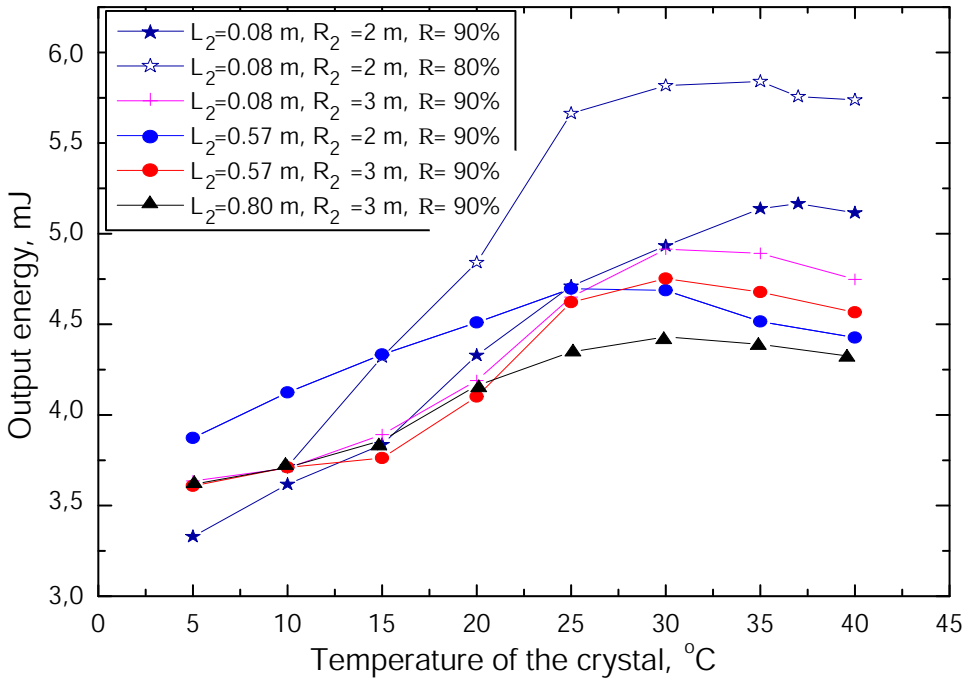

Figure 4.28: Output energy vs. temperature of the crystal for absorbed pump energy of 115 mJ and different resonator configurations. The resonators were comprised of a flat rear mirror placed at L_1= 0.1 m from the crystal and output coupler as indicated in the legend. The pump beam diameter was 3.0 × 3.2 mm.

In Fig. 4.29(a) are shown the power curves obtained from the selected resonators each with optimal temperature of the crystal. The highest output energy of 5.9 mJ was extracted from a resonator with L_2= 0.08 m, R_2= 2 m, $\mathcal{R}$=80 % and T= 34 °C . The conversion efficiency at the maximum pump energy was inversely proportional to the length of the resonator (Fig. 4.29(b)).

For the optimal temperature of the crystal a decrease of the build up time and the pulse width with about 5 % from the case with T= 15 °C was measured (Fig. 4.30). Using an output coupler with higher transmission did not result in a much longer pulse and delay.

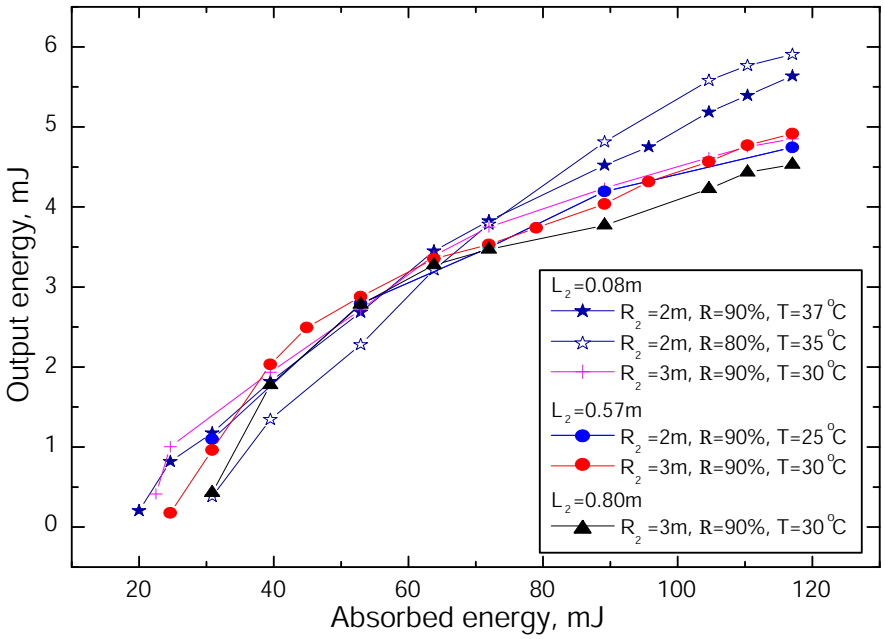

(a) Power curves

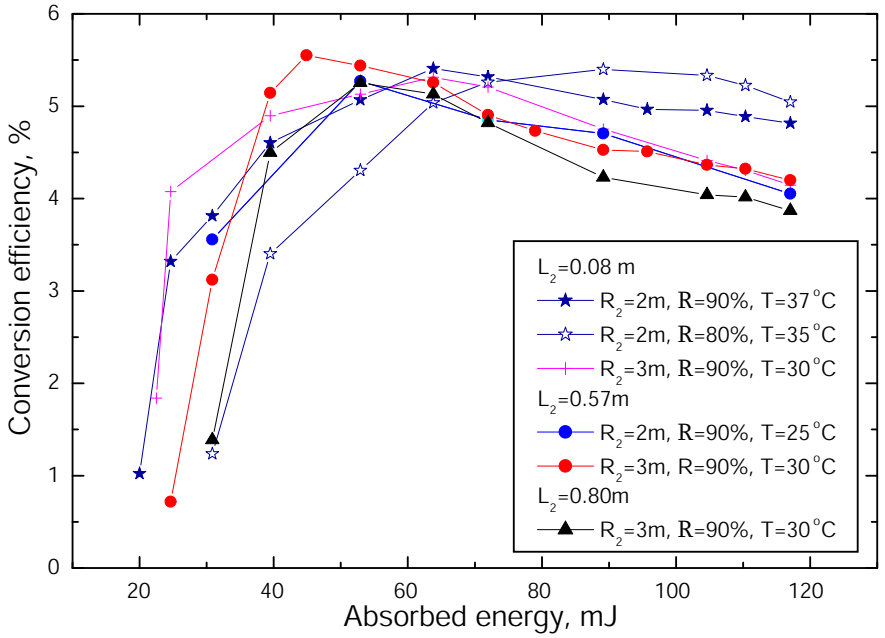

(b) Conversion efficiency

Figure 4.29: Output energy and conversion efficiency as a function of the absorbed energy for different resonator configurations using a flat rear mirror placed at $L_1 = 0.1$ m from the crystal and output couplers as indicated in the legend. The crystal temperature was optimal temperature for the maximum pump energy of 130 mJ. The pump beam diameter was 3.0×3.2 mm.

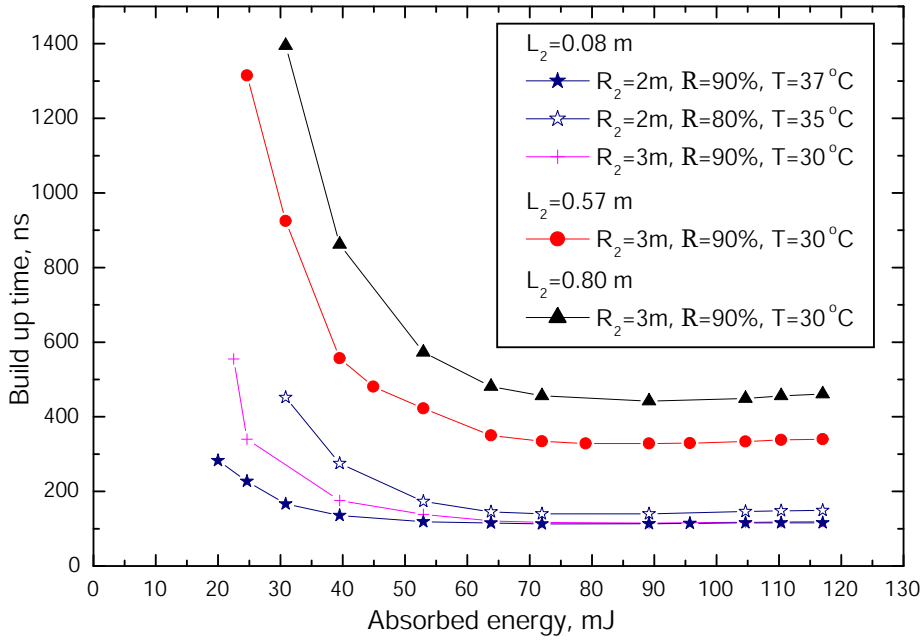

(a) Build up time

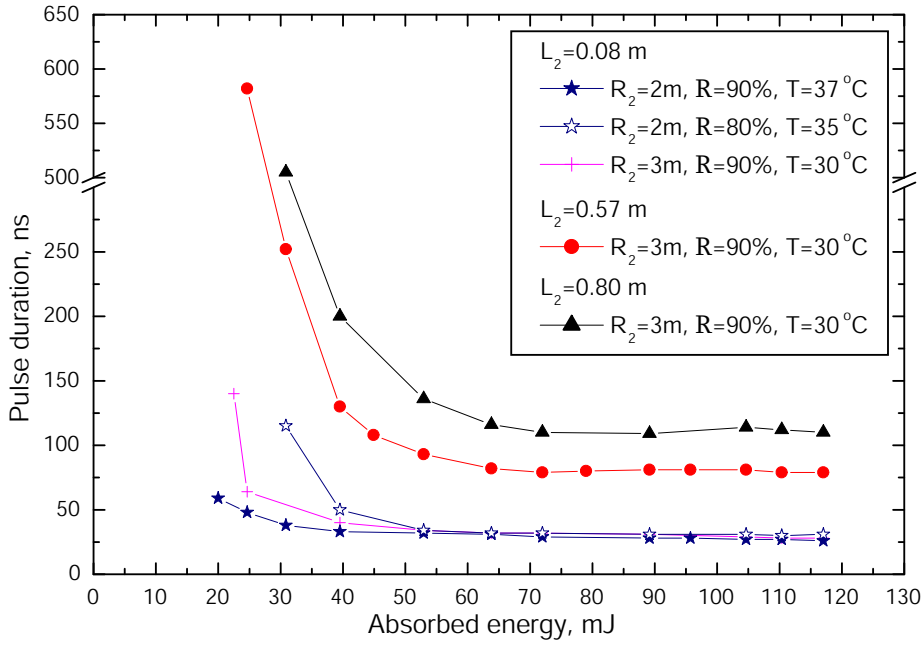

(b) Pulse width

Figure 4.30: Build up time and pulse width vs. absorbed pump energy for various resonators with a flat rear mirror placed at L_1= 0.1 m from the crystal and output couplers as indicated in the legend. The crystal temperature was optimal temperature for the maximum pump energy of 130 mJ. The pump beam diameter was 3.0×3.2 mm.

4.5.4 Discussion of the experimental results

The experimental results presented in this section are summarized on Fig. 4.31. In order to compare the laser performance for different pump beam sizes, the output energy is plotted versus the incident pump fluence. It is assumed a homogeneous energy distribution in the beam cross-sectional area with beam size as defined earlier in Section 2.6.1. For all resonator configurations low laser threshold at about 0.15 J/cm^2 was obtained. An increase of the output energy was observed for the larger pump beam size. Optimal temperature of the crystal T_{opt} was found for every resonator configuration at the maximum pump energy of 130 mJ. Full saturation of the output energy appeared at a pump energy density around 1 J/cm^2.

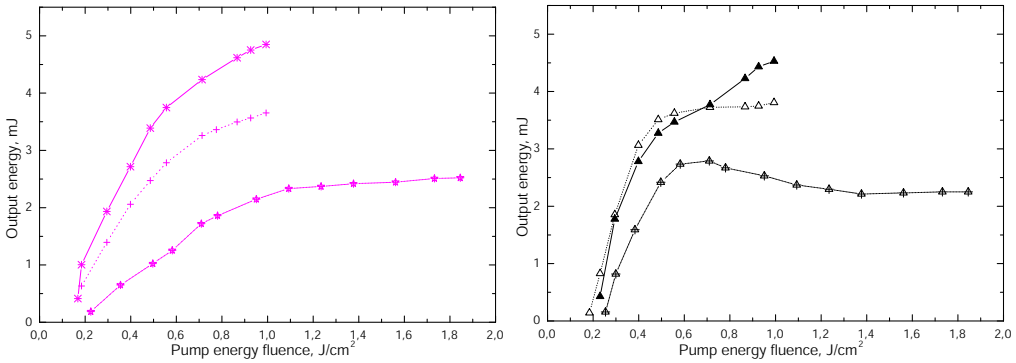

(a) L_2= 0.08 m, R_2= 3 m, $\mathcal{R}$=90 %, T_{opt}= 30 °C (b) L_2= 0.80 m, R_2= 3 m, $\mathcal{R}$=90 %, T_{opt}= 30 °C

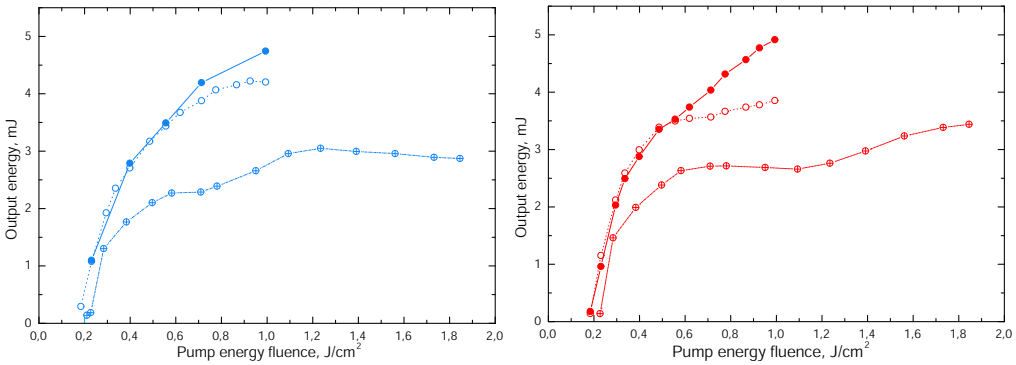

(c) L_2= 0.57 m, R_2= 2 m, $\mathcal{R}$=90 %, T_{opt}= 25 °C (d) L_2= 0.57 m, R_2= 3 m, $\mathcal{R}$=90 %, T_{opt}= 30 °C

Figure 4.31: Optimization of the laser performance for various resonator configurations with a flat rear mirror placed at L_1= 0.1 m and output coupler as indicated under each image. The pump diameter and the temperature of the crystal T are as follows: Dashed line: 2.0 × 2.1 mm, T= 15 °C. Dot line: 3.0 × 3.2 mm, T= 15 °C. Solid line: 3.0 × 3.2 mm and optimal temperature $T = T_{opt}$ for 130 mJ pump energy.

The experimental results can be explained with the rate equation model presented in Section 2.1. The calculations are performed for the values of σ_{GSA}, σ_{ESA_P}, and the total active ion concentration obtained from the fit of the pump power transmission curve (see Fig. 4.5).

Saturation of the output energy

Fig. 4.32 shows the inversion population $(n_i - n_f)/n_T$ averaged over the crystal length as a function of the pump fluence (see Eq. 2.7). The inversion population increases rapidly to 95 % for incident pump fluence of 0.75 J/cm^2. After that it increases slowly to 100 % at 1.1 J/cm^2. At this pump level full saturation of the output energy is reached and further increase of the pump energy does not result in an increase of the output energy. Moreover, a decrease of the output energy was observed in the full saturation region (see Figs. 4.31(b) and 4.31(c)). This effect is attributed to the existence of ESA of the laser photons [38, 82].

The behavior of the inversion population also explains the saturation of the absorption of the pump photons. The transmission of the pump energy through the crystal is half of its maximum when $(n_i - n_f)/n_T$=1.

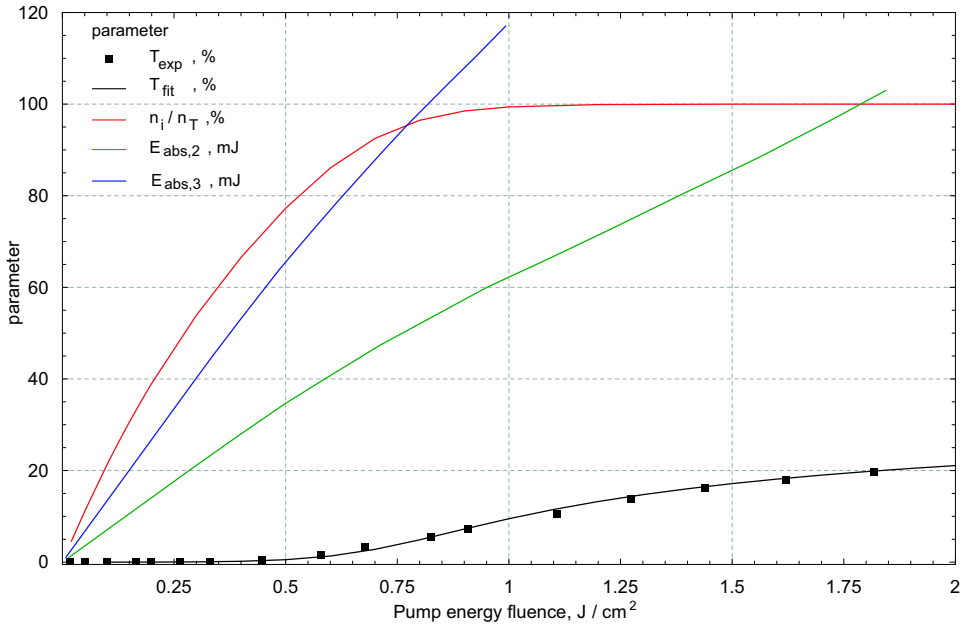

Figure 4.32: Theoretical inversion population ratio $(n_i - n_f)/n_T$, experimental transmission T_{exp} and its fit T_{fit} vs. pump energy fluence. Shown are also the absorbed energy for 2 mm ($E_{abs,2}$) and 3 mm pump beam ($E_{abs,3}$).

Laser threshold and power curves

In order to calculate the laser threshold, a knowledge of the dissipative losses in the resonator, the stimulated emission cross-section, and the ESA cross-section of the laser photons are needed (see Eq. 2.9). However, measurement of these parameters is outside of the scope of this project. The published values of the cross-sections differ by an order of magnitude (see Tab. 4.2). Therefore, the experimental threshold will be used as a fixed parameter in the equation for the output energy (Eq. 2.12) to fit the experimental power curves. From Fig. 4.32 it follows that the experimental laser threshold at $0.15\,\mathrm{J/cm^2}$ corresponds to 30 % inversion population.

The influence of the losses of the resonator $\mathcal{L}$ and the ratio $r_s = \sigma_{ESA_L}/\sigma_{SE}$ are investigated for mode radius of $0.51 \times 0.55\,\mathrm{mm}$. This is the exact mode size of TEM_{00} for the resonator with L_2= 0.08 m and R_2= 3 m (Fig. 4.31(a)). It is worth reminding the reader that due to the Brewster cut of the laser crystal, the beam in the crystal is elliptical. The beam radius in the tangential plane is enlarged by factor of $\tan\theta_B$=1.834. The output coupling is set to 90 %. Fig. 4.33 shows the dependence of the output energy of the ratio $\sigma_{ESA_L}/\sigma_{SE}$ for $\mathcal{L}$=2 %. The maximum possible extracted energy in the fundamental mode for this arrangement is 4 mJ in the absence of ESA. For $\sigma_{ESA_L} \neq 0$ the output energy decreases linearly with $(1-rs)$.

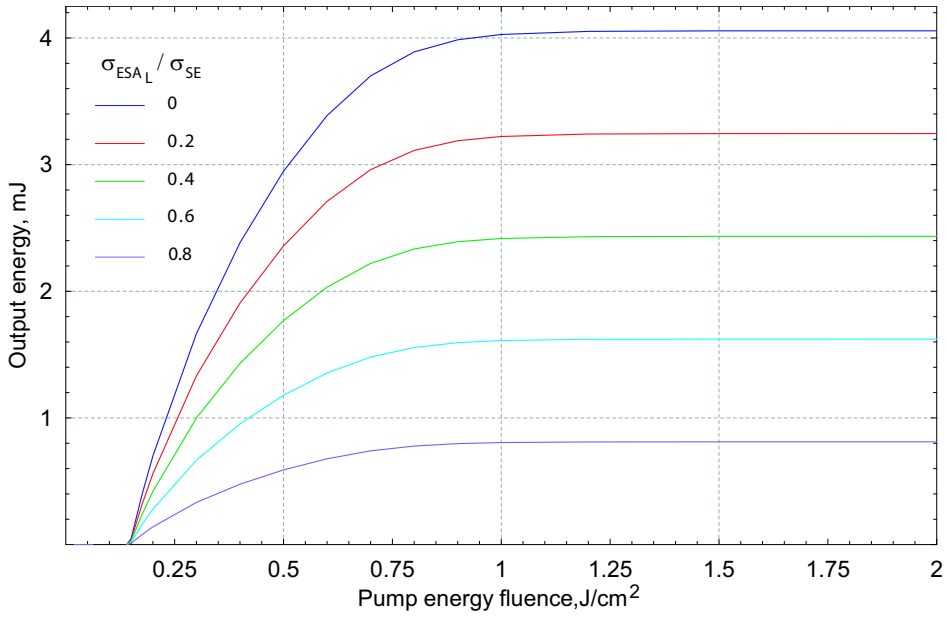

Figure 4.33: Theoretical laser output energy as a function of the pump energy fluence for different values of the ratio $\sigma_{ESA_L}/\sigma_{SE}$. The laser threshold is n_t= 0.3 $\mathrm{n_T}$, the mode radius is $0.51 \times 0.55\,\mathrm{mm}$, the dissipative losses in the resonator are $\mathcal{L}$=2 % and the output coupling is 10 %.

The output energy as a function of the resonator losses for an arbitrary r_s=0.5 is plotted on Fig. 4.34.

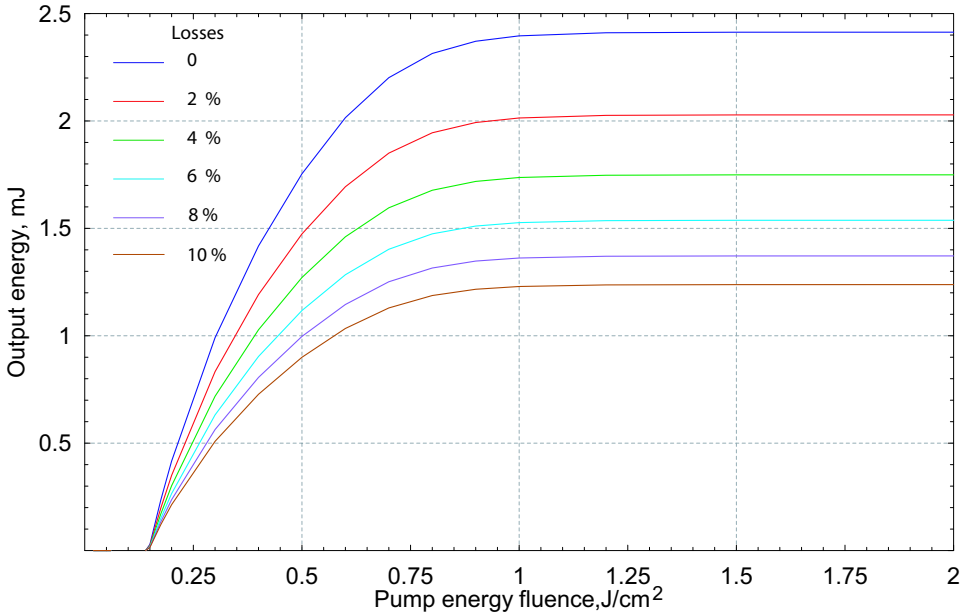

Figure 4.34: Theoretical output energy as a function of the pump energy fluence for different values of the dissipative losses in the resonator. The laser threshold is n_t=0.3 n_T, the mode radius is 0.51 × 0.55 mm, the ratio $\sigma_{ESA_L}/\sigma_{SE}$=0.5, and the output coupling is 90 %.

An increase of the resonator losses from 2 % to 10 % causes a decrease of the maximum output energy of 40 %. In the case of low gain laser medium, the losses are more critical for the laser performance. Therefore, high quality optics were used for the resonator. The rear mirror had a high reflectivity coating $\mathcal{R}$ >99.8 % and the rod was Brewster cut, for theoretically no reflection loss at the surface.

Dependence of the output energy on the pump beam size

According to Fig. 4.32, the inversion population and thus the output energy of the fundamental mode depend on the incident pump fluence. However, the experiments showed that for the same pump fluence more output energy can be achieved by enlarging the pump beam size in the crystal. This effect can be explained with the mode structure of the laser beam. If a larger volume of the active medium is excited, higher order modes are more likely to start oscillating which results in a rise of the extracted laser energy. In order to show that, the experimental power curves were fitted with Eq. 2.12. Later observations of the laser beam profile also confirmed this statement (see Section 4.6.3).

Here, the performance of the shortest resonator for a given temperature of the crystal 15 °C is modeled (Fig. 4.31(a)). The fitting parameters are the ratio $\sigma_{ESA_L}/\sigma_{SE}$ and the losses in the resonator $\mathcal{L}$. It is assumed a constant loss factor regardless of the size and the order of the modes. The best fit to the power curves was obtained with $\sigma_{ESA_L}/\sigma_{SE}$=0.66 and $\mathcal{L}$=2 %. Fig. 4.35 shows the output energy for different mode sizes. The experimental data, obtained with 2 mm pump beam are fitted with different mode sizes at different pump energy densities. First only the TEM_{00} mode oscillates with the mode size of 0.51 × 0.55 mm as predicted by the resonator design calculations. With increasing the pump energy, higher order modes are generated which occupy larger areas of the laser rod. The experimental data points obtained with a 3 mm pump beam depart on the theoretical curve for mode size 0.84 × 0.84 mm. As a result, higher output energy is achieved.

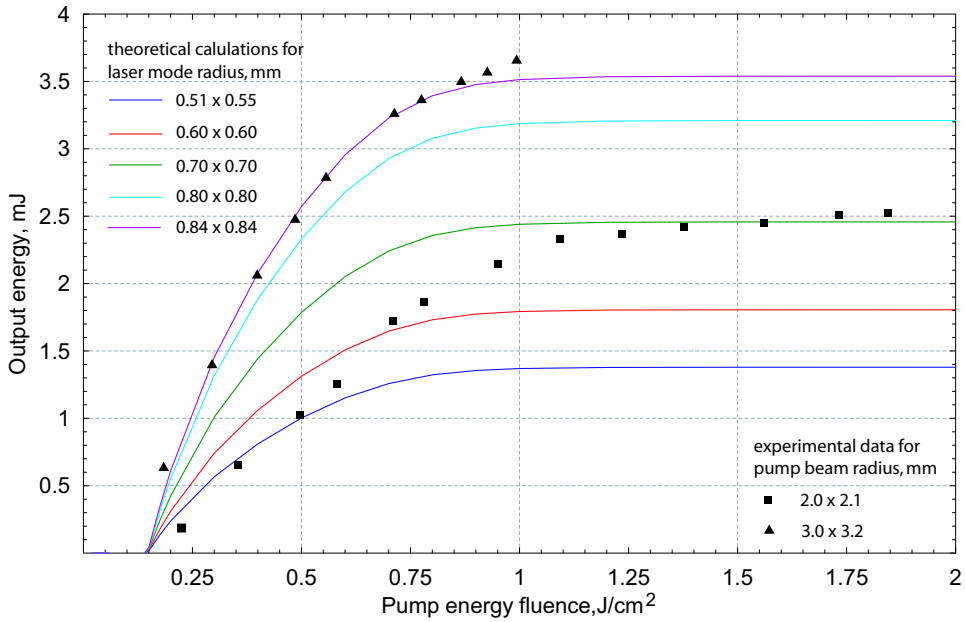

Figure 4.35: Theoretical fit of the experimental results obtained with resonator with a flat rear mirror placed at L_1= 0.1 m and an output coupler R_2= 3 m, $\mathcal{R}$=90 %, and L_2= 0.08 m. The temperature of the crystal was T= 15 °C. The losses in the resonator are set to $\mathcal{L}$=2 % and the ratio $\sigma_{ESA_L}/\sigma_{SE}$=0.66.

The fitting parameter r_s=0.66 is as reported in [153] and is within the range of the published values 0.39 in [107] to 0.71 in [15] (see Tab. 4.2). Utilizing the best-fit parameters and the experimental threshold in Eq. 2.9, the σ_{SE} and σ_{ESA_L} were estimated to 2.65 × 10^{-19} cm^2 and 1.75 × 10^{-19} cm^2, respectively. These values are in good agreement with the values obtained in [107]. The difference in σ_{SE} is 20 % and in σ_{ESA_L} only 3 %. However, after precise measurements of the laser threshold and the resonator losses these values can deviate (see Eq. 2.9).

The single pass gain of the crystal can be estimated according to

$$G = \exp^{(\sigma_{SE} - \sigma_{ESA_L})\, n_2 l_{cr}}, \tag{4.9}$$

where $g = (\sigma_{SE} - \sigma_{ESA_L})\, n_2$ is the linear gain coefficient in cm^{-1}. For $n_2 = n_T = 6.4 \times 10^{17}\,\mathrm{cm}^{-3}$ and the fit values of the cross-sections follows that g= $0.06\,\mathrm{cm}^{-1}$ and the single pass gain coefficient G=1.22. Mathieu et al. [101] have reported a gain coefficient of $0.05\,\mathrm{cm}^{-1}$ for higher inversion population of $\approx 8 \times 10^{17}\,\mathrm{cm}^{-3}$.

The rest of the measurements (see Fig. 4.31(b)–4.31(d)) show more rapid increase of the emitted energy for low pump fluence, which is a sign for generation of higher order modes close to the laser threshold.

Dependence of the output energy on the temperature of the crystal

In Section 4.5.3 was demonstrated the impact of the crystal temperature on the laser performance. Approximately the same output energy was obtained for incident energy fluence $< 0.5\,\mathrm{J/cm}^2$ for operation at 15 °C and optimal crystal temperature T_{opt} for 130 mJ pump energy (see Figs. 4.31(b), 4.31(c), and 4.31(d)). As illustrated in Fig. 4.25, the output energy was almost a constant for those temperatures and absorbed energy less than 115 mJ ($1\,\mathrm{J/cm}^2$). In the shortest resonator, on the other hand, the output energy was higher for the entire range of pump fluence (see Fig. 4.31(a)). The rise in output energy at the maximum pump fluence was between 13 % and 33 % for the resonators with L_2= 0.57 m, R_2= 2 m and L_2= 0.0.08 m, R_2= 3 m, respectively. It is worth to point out that the optimal temperature was not constant for all resonator configurations (see Fig. 4.28).

Parameters which may be responsible for the dependence of the output energy on the crystal temperature are: (i) absorption of the pump energy, (ii) fluorescence life time, (iii) thermal lensing, and (iv) losses due to ESA of the photons at the emission wavelength.

(i) Measurement of the absorption of the pump photons for temperature of the crystal ranging from 5 °C to 40 °C indicated that the absorption is not temperature dependent (see Fig. 4.24).

(ii) The fluorescence lifetime decreases by increasing the temperature [86]. For the temperature interval of interest, the lifetime is a few μs which, as described in Section 2.1, is very long compared to the pump pulse duration and is therefore neglected in the rate equations.

(iii) The thermal lensing was measured only for crystal temperature of 15 °C and 2-mm pump beam diameter. The pump energy was 130 mJ. For larger pump beam size the intensity is reduced and as a result the thermal focusing power is expected to decrease. In order to estimate the thermal focusing power for crystal temperatures other than 15 °C one has to know the temperature dependence of the refractive index (see Eqs. 2.37 and 2.38). In general, stronger thermal lens is expected for higher temperatures.

All tested resonators have very broad stability zone (see Fig. 4.10(a)). Possible shortening of the thermal focal length (even down to f_{tan}=3 m) for higher crystal temperatures or increase due to larger pump beam sizes leads to a slight change of the mode size and the laser remains stable. However, the beam propagation in the cavity and the divergence change as a function of the thermal focal length (compare the beam propagation in the tangential and sagittal planes in Figs. 4.11–4.13). This will affect the higher order modes stronger than the fundamental mode. The beam divergence of the mode of order m is proportional to the divergence of the fundamental mode as $\theta_m = \sqrt{m}\,\theta_0$ [140]. Therefore for certain temperature of the crystal the thermal focal lens is optimal in terms of beam divergence in the cavity and thus low diffraction losses. In this case higher order modes are generated and higher output energy is achieved (see Fig. 4.31). This temperature may not be optimal for other pump energies due to different induced thermal lensing (see Fig. 4.25). As it was shown in Fig. 4.28, for the same pump level the optimal temperature varies with the resonator configuration. This effect can be attributed to the optimal mode matching which occurs for different thermal lensing or respectively temperature of the crystal.

(iv) The remaining and very important parameter for the laser performance is the ratio of the stimulated emission and ESA cross-sections $r_s = \sigma_{ESA_L}/\sigma_{SE}$ (see Fig. 4.33). Since the mode size and the cavity losses are not constant with crystal temperature variations, it is hard to make any conclusions about the temperature dependence of r_s based only on the laser output characteristics from Figs. 4.25–4.27. Spectroscopic measurements of both cross-sections as a function of the crystal temperature are required. However, it is possible that r_s has a minimum at certain crystal temperature T_{opt} as a result of thermally induced transitions in the crystal. For instance, for alexandrite laser crystal σ_{SE} and σ_{ESA_L} are temperature dependent due to interaction between the upper laser level and the storage level. Shand and Jenssen [132] have reported an increase of both cross-sections with temperature ($28 - 290\,^{\circ}\mathrm{C}$) at approximately the same rate. However, the ratio $\sigma_{ESA_L}/\sigma_{SE}$ increased at $250\,^{\circ}\mathrm{C}$, which is consistent with the experimental results obtained by Guch and Jones [50]. From the investigations of the performance of alexandrite laser for the temperature interval $34 - 310\,^{\circ}\mathrm{C}$ they have found that the optimal temperature of the crystal is $225\,^{\circ}\mathrm{C}$.

Dependence of the output energy on the resonator configuration for the optimal temperature of the crystal

In the regime of multiple transverse mode operation and optimal temperature of the crystal for 130 mJ pump energy the conversion efficiency at this pump level increased for shorter cavities (see Fig. 4.25). High order modes have large divergence and experience large diffraction losses. Short resonators are, geometrically, less sensitive to divergence. This makes it possible for higher (compared to the modes in a longer cavity) order modes to oscillate and extract more laser energy (see Fig. 4.46).

The regime of single transverse modes operation was investigated later and the reader is referred to Section 4.6.1.

Pulse length

The laser pulse duration for various resonator configurations was calculated with the aid of Eq. 2.13 using the experimental threshold (see Fig. 4.36). The theoretical values are in good agreement with the experimental results (see Figs.4.18–4.20, 4.23, 4.30).

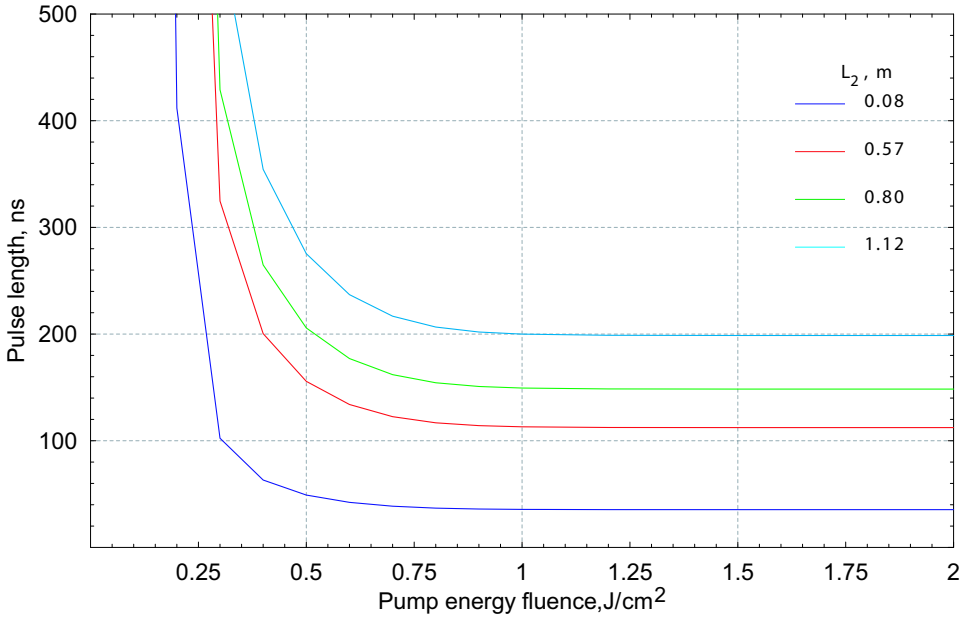

Figure 4.36: Theoretical pulse duration for the tested resonators with a flat rear mirror placed at distance L_1= 0.1 m and an output coupler R_2= 3 m, $\mathcal{R}$=90 %. The position of the output coupler with respect to the crystal is as indicated in the legend.

In order to understand the discrepancies in pulse duration and the build-up time for different pump size and temperature of the crystal, precise measurements of the laser threshold and more comprehensive analysis are required, which is beyond the scope of this work.

4.6 Tunable Cr^{4+}:YAG laser

The tunability of Cr^{4+}:YAG was investigated with two main configurations: L_1= 0.065 m for both and L_2=0.135 m and L_2= 0.57 m. The output coupler had a radius of curvature R_2=2 m and its transmission was varied. The temperature of the crystal was optimized for maximum output energy at the peak wavelength of the tuning curve. The tuning and power curves were compared to the case with crystal's temperature set to 20 °C. The experimental set up of the shorter resonator with the wavelength selective element, the birefringent filter (BF), is shown in Fig. 4.37.

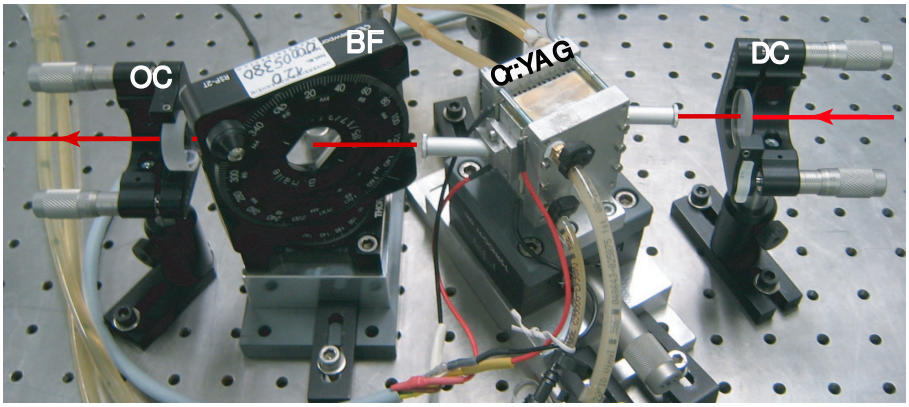

Figure 4.37: Laser resonator with a 3-stage birefringent filter at the Brewster angle. DC: dichroic rear mirror, BF: birefringent filter, OC: output coupler.

4.6.1 Tuning element

The tuning of the laser wavelength was performed with a birefringent filter (see Fig.4.37). The filter was composed of three parallel plates of the uniaxial crystal crystalline quartz. They were cut so that the optical axes lies in the plane of the plate. The assembly was placed in the cavity at the Brewster angle with respect to the incident beam for a minimum losses at the surfaces of the plates.

In a birefringent plate the incoming beam splits into two beams called ordinary (o-beam) and extraordinary (e-beam) whose polarizations are 90 ° to each other. The o- and e- beams propagate at different speeds due to different indices of refraction n_o and n_e, respectively, and overlap when they emerge from the crystal. The transmission of the filter depends on the resulting polarization which is a function of the path difference of the emerging o- and e-beams. Maximum transmission of the filter is obtained for a wavelength λ, which corresponds to a path difference $m\lambda$ (m–integer) and unchanged polarization state. At any other wavelength, the output beam has elliptical polarization and suffer losses at the Brewster surfaces. By rotating the birefringent plate around an axis perpendicular to the surface of the plate

the condition for maximum transmission is fulfilled for different wavelengths and the laser wavelength is changed.

A birefringent plate is described with the Jones matrix [13, 46, 59, 62, 121].

$$J = \begin{pmatrix} a\,(\cos^2\gamma + \sin^2\gamma\, e^{i\delta}) & a\sin\gamma\cos\gamma\,(1 - e^{i\delta}) \\ a\sin\gamma\cos\gamma\,(1 - e^{i\delta}) & \sin^2\gamma + \cos^2\gamma\, e^{i\delta} \end{pmatrix} \tag{4.10}$$

Here, $a = 2\,n_o/(1 + n_o^2)$ and γ is the angle between the incident plane and the plane which contains the optic axis and the refracted rays. δ is the phase difference between the o- and e-beams after passing the plate with thickness d_{BF} [62]

$$\delta = \frac{2\pi}{\lambda}\,\zeta\, d_{BF}, \quad \text{with} \quad \zeta = n_e\cos\beta_e - n_o\cos\beta_o, \tag{4.11}$$

where β_o and β_e are the angles of refraction of the ordinary and extraordinary beams, respectively.

The incident beam can be represented by the Jones vector (E_σ, E_π), where E_σ and E_π are the scalar components of the electric field corresponding to perpendicular (σ-polarization or transverse-electric wave) and parallel polarization (π-polarization or transverse-magnetic wave). As the polarization of the incident beam is π and it remains unaffected after passing the filter, the transmitted field vector is [121]

$$\begin{pmatrix} 0 \\ E'_\pi \end{pmatrix} = J. \begin{pmatrix} 0 \\ E_\pi \end{pmatrix}. \tag{4.12}$$

This equation is satisfied if the (1, 2) element of the Jones matrix is 0 (hence $J_{12} = J_{21} = 0$). Then $E'_\pi = J_{22}E_\pi$ and $|J_{22}|^2$ is the intensity fraction transmitted through the plate ($I = EE^*$). The transmission maxima are at wavelengths [62]

$$\lambda = k/\zeta\, d_{BF},\ k > 0. \tag{4.13}$$

The factor $(1/\zeta\, d_{BF})$ is the free spectral range (FSR). It has been shown that the transmission of unwanted wavelengths is suppressed most efficiently if the plate is oriented at angle $\gamma = 45^o$ [62]. The linewidth of the selected wavelength reduces at every transit through the filter and the side peaks are suppressed more.

For a multiple-stage filter the overall transmission is a product of the transmissions of all components. The thickness of each element is a multiple integral of the thickness of the thinnest plate, which determines the FSR. The thickest plate determines the linewidth of the transmitted maxima.

In order to demonstrate tunability of Cr:YAG laser a 3-stage "off the shelf" BF was used (Bernard Halle Nachfl. GmbH, Germany). The thickness of the plates was in a ratio of 1:2:4 with thinnest plate of 0.85 mm which corresponds to a FSR of 290 nm. The filter had 100 % transmission at 1450 nm with FWHM after one passage of 32 nm (4566 GHz) for an angle $\gamma = 29.5^o$. The side band transmission for this particular

setting was between 20 % and 30 % for wavelengths in the region 1355–1420 nm and 1475–1530 nm, respectively. The birefringent filter was mounted in a rotational stage (Newport, RSP-2T) with scale graduated in 2° increments for angular positioning. This mount was placed on top of a rotation platform (Thorlabs RP01) for setting the Brewster angle of incidence (see Fig.4.37). Rotation of the BF by 2° resulted in tuning the laser by 15.5 nm [161]. More optimal design in terms of narrow linewidth is proposed in Appendix E. Fine tuning can be performed with a motorized rotational mount which ensures rotating by a fraction of a degree.

4.6.2 Experimental set up for measurement of the spectral characteristics of the laser

The tuning range of the laser was measured with a spectrometer (SPEX Industries, Inc., model 340E) using a blazed reflection grating in a Czerny-Turner configuration. For a detailed theoretical description of the principles of a grating spectrometer, please see Appendix F.

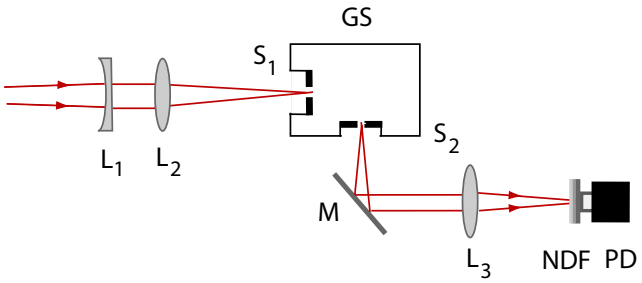

Figure 4.38: Experimental set up for measuring the tuning range of Cr^{4+}:YAG with a grating spectrometer. L_1, L_2: lens combination to match the f-number of the spectrometer, GS: grating spectrometer, S_1, S_2: entrance and exit slits, M: aluminum coated folding mirrors, L_3: focusing lens, NDF: neutral density filter, PD: photo detector.

The SPEX spectrometer had a wavelength readout corresponding only to the original grating. The grating used for these experiments was different: it had a groove density of 150 gr/mm and a blaze wavelength of 4 μm for the first diffraction order. Therefore, the instrument was first calibrated using a He:Ne laser at 632.8 nm up to the 13-th diffraction order in a similar arrangement as shown in Fig. 4.38. The correct wavelength was nonlinear with the wavelength readout due to some problems of the driver rotating the grating mount. The spectral measurements of the laser output of Cr^{4+}:YAG were performed with the set-up presented in Fig. 4.38. The laser beam was first expanded with a PLCC lens L_1 and than focused onto the entrance slit (slit opening $\approx$100 μm) with a PLCX lens L_2. The throughput was focused on a photodetector and observed with an oscilloscope. Initially, the f-number of the lens

L_2 exactly matched the f-number of the collimating mirror of the spectrometer (M_1 in Fig. F.1). Unfortunately, this produced a beam spot so large on the mirror and grating surfaces that it was not sufficiently observable with a sensitive IR viewing card. As a result the alignment of the beam through the spectrometer was not possible. In order to ensure a brighter and observable spot, i.e. proper alignment, another lens combination was used with a larger f-number (L_1 with f=1 m and L_2 with f=–0.1 m). This projected a visible spot on the viewing card but it did not illuminate the entire grating. Consequently, the accuracy of the measurements of the IR beam was reduced to ±2 nm and the spectral resolution was estimated to 0.5 nm.

4.6.3 Experimental results

Tuning range and output energy as a function of the resonator length, the output coupling and the temperature of the crystal

The tunability of both resonator configurations for absorbed energy of 105 mJ is presented in Fig. 4.39. A maximum tuning range of 198 nm (from 1325 nm to 1523 nm) was obtained in the shorter resonator (Fig. 4.39(a)) with the OC's transmission of 10 % and T_{opt}= 34 °C. The peak wavelength was 1447 nm which seems to be an experimental error. When the transmission of the OC was increased to 20 %, the tuning range decreased from both ends approximately the same amount (30 nm) down to 136 nm and the peak wavelength shifted to 1432 nm. This is the gain maximum of Cr^{4+}–ions [38]. However, with this OC, higher output energy was obtained for the spectral range 1364–1485 nm. For temperature of the crystal 20 °C and OC $\mathcal{R}$=80 % the output energy decreased at all wavelengths.

Approximately the same tuning range as with the shorter resonator with $\mathcal{R}$=90 % was obtained with the longer resonator with $\mathcal{R}$=90 % and T_{opt}= 30 °C only less output energy (see Fig. 4.39). For $\mathcal{R}$=80 % and T_{opt}= 34 °C the output energy and the tuning range decreased. The output energy around the peak wavelength of 1430 nm was approximately the same as for 10 % output coupling. Interestingly, with the OC $\mathcal{R}$=80 %, a slightly broader tuning range and higher output energy at the wavelength regions 1371–1375 nm and 1470–1477 nm was obtained for T= 20 °C. This effect was not observed using the shorter resonator. When the laser was aligned to oscillate at the fundamental mode, the tuning range and the peak wavelength remained the same as in multimode operation.

The spectral dependence of the pulse width and the build up time was also measured and is presented in Fig. 4.40. The pulse duration was 29–33 ns and 100–120 ns around the peak wavelength for the resonators with L_2= 0.135 m and L_2= 0.57 m, respectively. The pulse length and the delay variation with the crystal temperature was ≤1 % for the entire spectral range for both configurations. Both temporal parameters were shorter for 10 % output coupling.

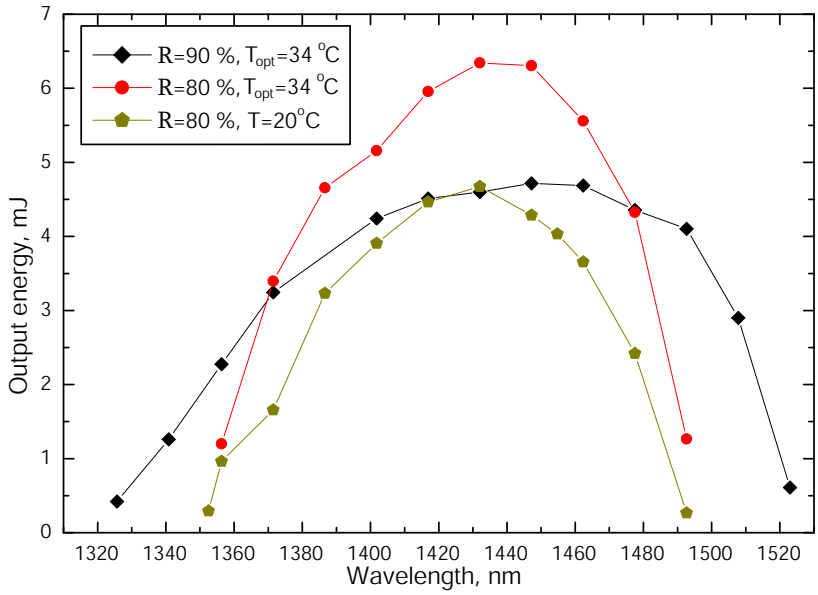

(a) Resonator configuration L_1=0.065 m, L_2=0.135 m, R_2=2 m

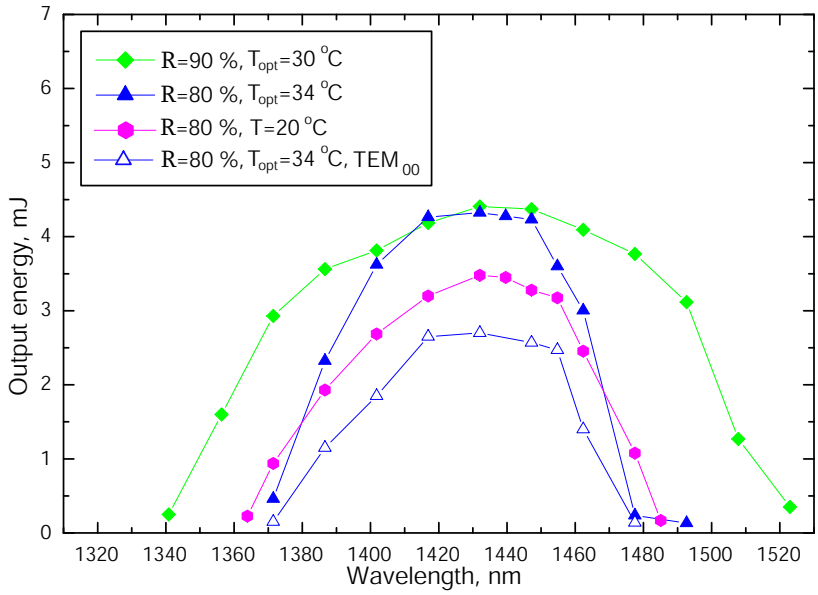

(b) Resonator configuration L_1=0.065 m, L_2=0.57 m, R_2=2 m

Figure 4.39: Tuning curves of two resonator configurations for 105 mJ absorbed pump energy. The reflectivity of the output coupler and the crystal's temeperature were varied as indicated in the legends. T_{opt} was the optimal temperature of the crystal for 105 mJ absorbed pump energy. The laser was operating in a multimode regime except for the case indicated with TEM_{00} in (b).

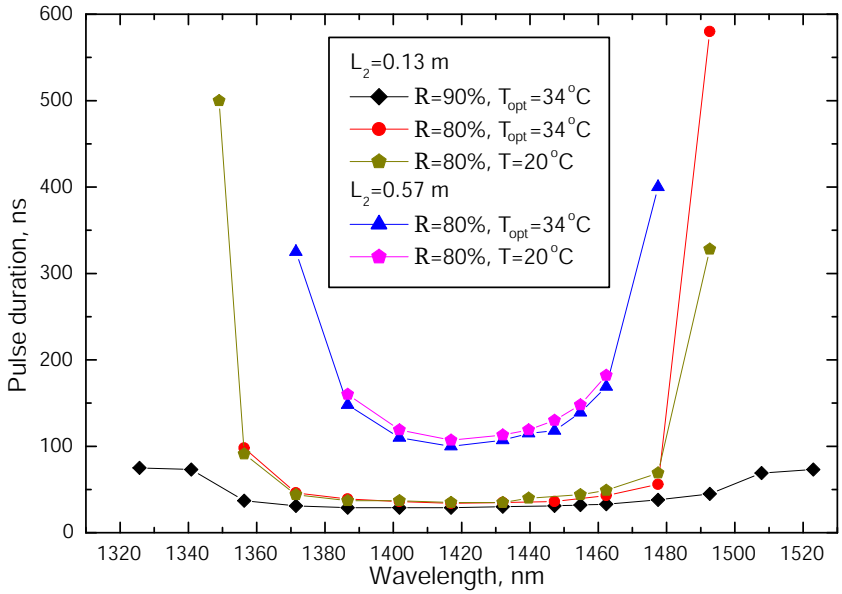

(a) Pulse width

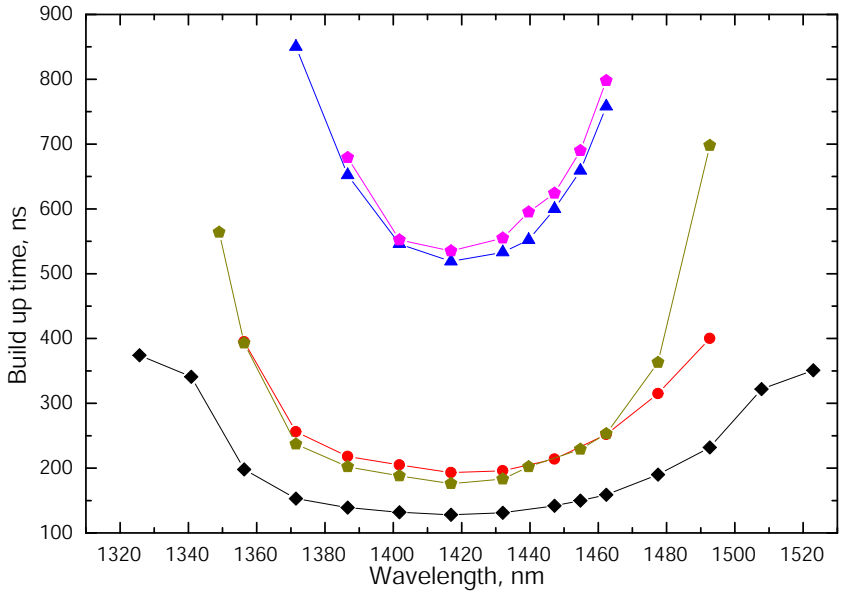

(b) Build up time

Figure 4.40: Pulse width and build up time as a function of the laser wavelength for 105 mJ absorbed pump energy. The data were obtained from two resonator configurations using output couplers with different reflectivity and keeping the laser crystal at different temperatures as indicated in the legend. $L_1 = 0.065$ m and the radius of curvature of the output coupler was $R_2 = 2$ m.

The laser was tuned at the peak wavelength of 1432 nm and the power curves were recorded. In the shorter resonator (see Fig. 4.41), the optimal conditions in terms of low laser threshold and high output energy were $\mathcal{R}$=80 % and T_{opt}= 34 °C. The laser threshold increased for 30 % output coupling and lower temperature of the crystal. The saturation of the ouput energy occured at 90 mJ absorbed energy for $\mathcal{R}$=70 % and >115 mJ for $\mathcal{R}$=80 %. In the fundamental mode regime with $\mathcal{R}$=80 % and T_{opt}= 34 °C, the laser threshold was substantially higher and the maximum output energy lower by a factor of 4.5 compared to the operation in multimode regime.

The output energy as a function of the absorbed energy was measured for the 20 % output coupling and optimal temperature of the crystal without the BF. About 6–7 % more energy was extracted compared to the case of the same cavity with the BF tuned at the peak wavelength.

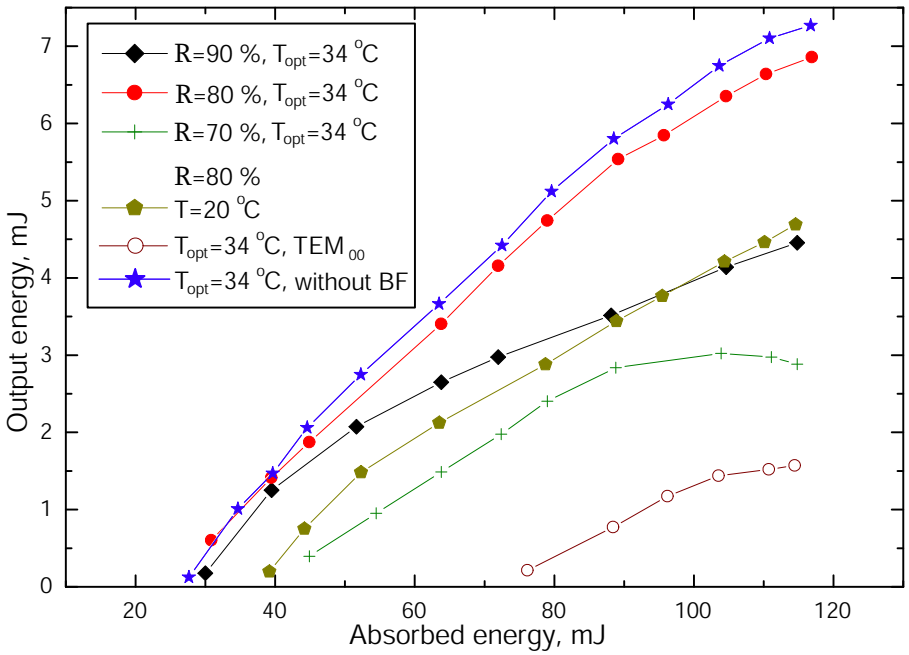

Figure 4.41: Output energy at 1432 nm vs. absorbed energy of the resonator configuration L_1= 0.065 m, L_2= 0.135 m, R_2= 2 m. The reflectivity of the output coupler and the crystal's temperature were varied as indicated in the legend. T_{opt} was the optimal temperature of the crystal for 115 mJ absorbed pump energy. The laser was operating in multimode regime except the case indicated with TEM_{00}.

In the case of the resonator with L_2= 0.57 m (see Fig. 4.42) the optimal conditions for multimode operation were 10 % output coupling and T_{opt} = 30 °C. It delivered less output energy compared to the shorter resonator. This is a result of the generation of lower order modes TEM_{mn} (see Section 4.5.4). However, this resonator showed better performance in the fundamental mode regime due to larger mode size (see Fig. 4.9(a)).

By utilizing the values of the thermal lens for T= 15 °C the calculated ratio of the fundamental mode area in the longer to the shorter resonators is 1.66. The maximum output energy, obtained with the longer resonator was 1.6 times higher than with the shorter resonator which is in good agreement with the theoretical calculation.

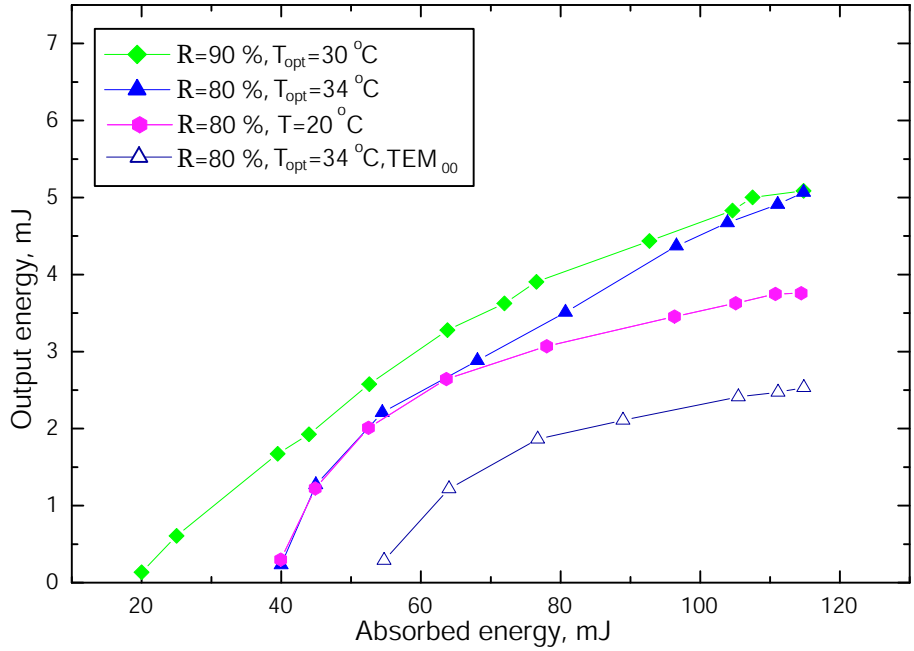

Figure 4.42: Output energy at 1432 nm vs. absorbed energy of the resonator configuration L_1= 0.065 m, L_2= 0.57 m, R_2= 2 m. The reflectivity of the output coupler and the crystal's temperature were varied as indicated in the legend. T_{opt} was the optimal temperature of the crystal for 115 mJ absorbed pump energy. The laser was operating in multimode regime except for the case indicated with TEM_{00}.

Tuning range as a function of the pump level for two different resonator configurations

Next, the dependence of the spectral output of both resonator configurations with OC $\mathcal{R}$=80 % and T_{opt}= 34 °C was investigated for different pump levels. The data are illustrated in Fig. 4.43. In the short resonator, the output energy was proportional to the absorbed energy for all wavelengths except 1493 nm. In the long resonator and in both ends of the tuning curve, higher output was obtained for lower pump energy. During these measurements it was observed that the longer wavelengths saturate at lower pump level, which explains this behavior.

Eilers et al. [38] have reported that the tuning range can be expanded towards shorter wavelengths for high pump energies and towards longer wavelengths by re-

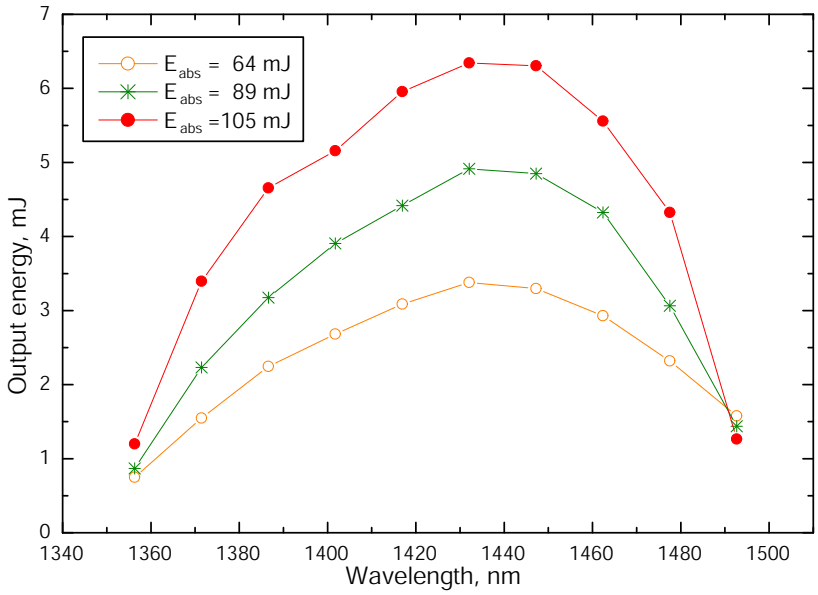

(a) Resonator configuration L_1= 0.065 m, L_2= 0.135 m, R_2= 2 m, $\mathcal{R}$=80 %, T_{opt}= 34 °C

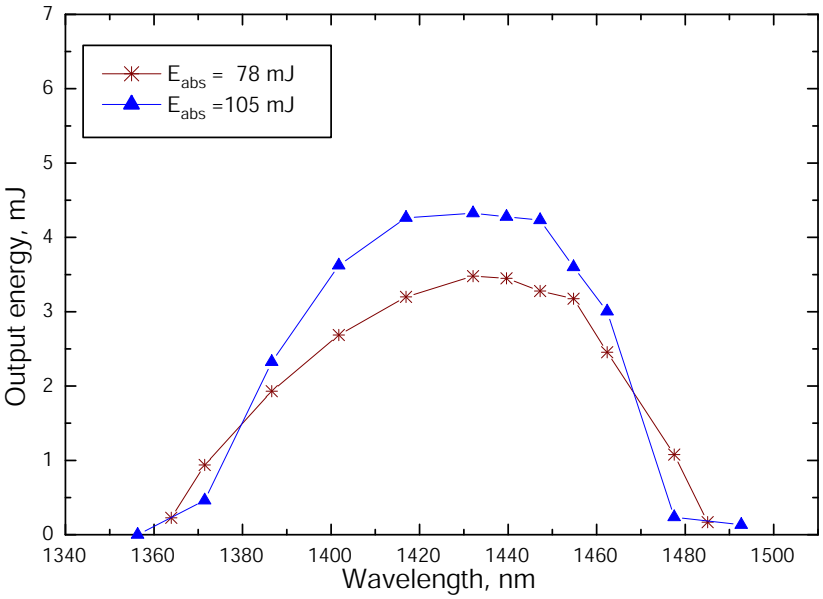

(b) Resonator configuration L_1= 0.065 m, L_2= 0.57 m, R_2= 2 m, $\mathcal{R}$=80 %, T_{opt}= 34 °C

Figure 4.43: Tuning curves for different absorbed pump energies, obtained from two resonator configurations in multimode regime.

ducing the pump energy. The exact limits of the tuning range were not determined in the experiments presented here due to the coarse rotation of the birefringent filter.

Linewidth

The linewidth at 1455 nm was determined for the short resonator with output couplers with $\mathcal{R}$=90 % and $\mathcal{R}$=80 %. The temperature of the crystal was optimal at 34 °C. The measurement was performed with the grating spectrometer and the set up illustrated on Fig. 4.38. The experimental data were fitted with a Gaussian function (see Fig. 4.44) and the FWHM was determined. The linewidth was approximately 1.4 nm (198 GHz). This result was confirmed by an additional measurement using a Fabry-Perot interferometer-based spectrum analyzer (EXFO Burleigh, TL-1500-NIR). The Fabry-Perot interferometer was in a plano-mirror configuration with mirror separation of 0.1 mm. The corresponding free spectral range was 1500 GHz and the minimum resolvable bandwidth was 10 GHz.

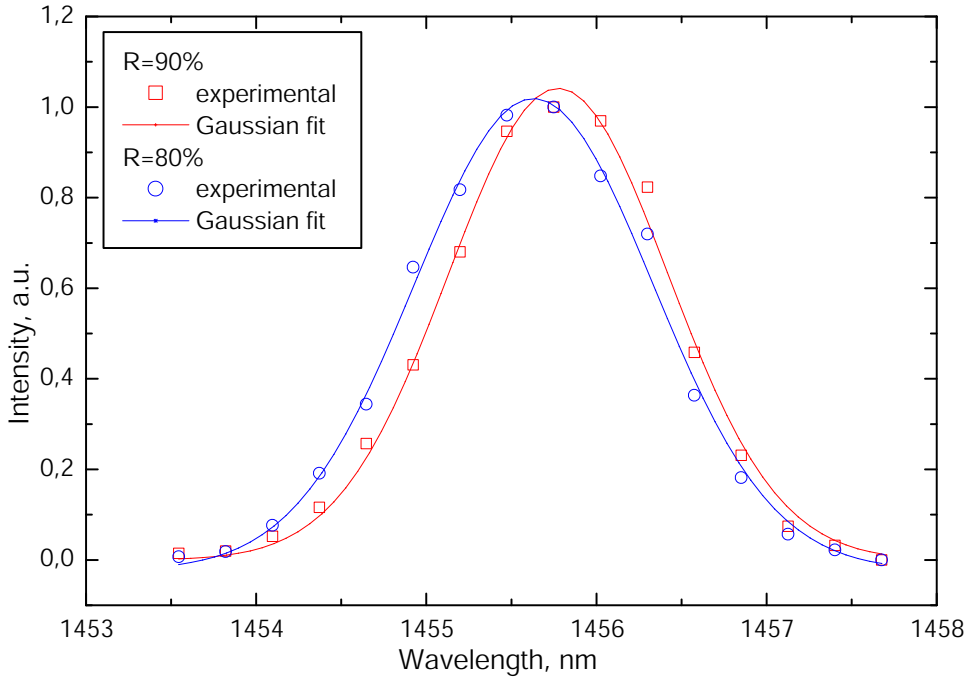

Figure 4.44: Linewidth at 1455 nm, obtained with the resonator L_2= 0.135 m and R_2= 2 m with reflectivity $\mathcal{R}$ =90 % and $\mathcal{R}$ =80 %. The experimental data are fitted with a Gaussian function.

The linewidth of the longer resonator is expected to be narrower due to the higher number of transits through the BF.

Beam profiles and M^2 measurement

It was shown earlier (see Eq. 2.12) that the extracted output energy is a function of the laser mode size which depends upon the order of the mode. This subsection presents observations of the beam profile, how the modes develop, and their impact on the beam propagation factor.

Here, the generation of higher order modes with increasing pump energy was observed using an IR camera placed at 1.78 m after the OC. The cavity was L_2= 0.135 m, R_2= 2 m, $\mathcal{R}$=80 %, and without a birefringent filter. The temperature of the crystal was kept optimal at 34 °C. Fig. 4.45 shows that higher order modes started oscillating from absorbed energy of ≈ 65 mJ. At this pump level the gain of higher order modes overcomes the diffraction losses in the cavity. The laser beam diameter increased and consequently so did the output energy.

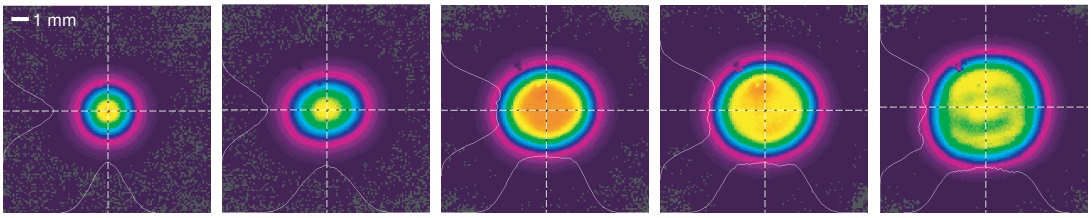

(a) E_{abs}=38 mJ, E_{out}=1.5 mJ (b) E_{abs}=64 mJ, E_{out}=3.7 mJ (c) E_{abs}=78 mJ, E_{out}=5.0 mJ (d) E_{abs}=90 mJ, E_{out}=5.9 mJ (e) E_{abs}=105 mJ, E_{out}=6.9 mJ

Figure 4.45: Generation of high order modes by increasing the pump energy. The resonator configuration was L_2= 0.135 m and R_2= 2 m, $\mathcal{R}$=80 %, T_{opt}= 34 °C and without the birefringent filter. The beam profiles were observed 1.78 m after the output coupler. The absorbed pump energy and the extracted output energy are indicated below each image.

In Fig. 4.46, the pump beam profiles obtained with different resonator configurations are compared for maximum pump energy of 130 mJ. In the case of the short resonator (Fig. 4.46(a)–4.46(c)) the beam cross-sections appeared very similar in terms of size, shape, and mode structure despite the output coupling and the presence or not of a BF. The beams were superposition of high order modes resulting in a top-hat profile with small variations of the energy distribution. However, the beam profile for T= 20 °C (Fig. 4.46(d)) was elliptical and, in general, smaller than that of the optimal temperature of the crystal. Also, the beam was comprised of lower order modes compared to the same cavity with T_{opt}= 34 °C, which explains the lower extracted energy (see Fig. 4.41). Apparently, T_{opt}= 34 °C was a favorable condition for generating higher order modes (see Section 4.5.4).

The beam profile of the longer resonator (Fig. 4.46(e)) does not contain modes of such high order as the shorter resonator. The energy in the center was only 1/3 of

the maximum energy and the beam profile resembled the mode refered to as "donut" which has a low intensity core. The temperature of the crystal was optimal and thus the laser operated in the highest possible order modes. The generation of even higher modes was restricted by the geometry of the cavity (see Section 4.5.4).

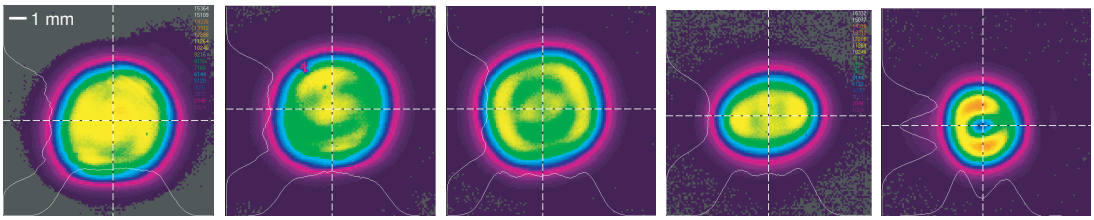

(a) L_2= 0.135 m, $\mathcal{R}$=90 % (b) L_2= 0.135 m, $\mathcal{R}$=80 %, without BF (c) L_2= 0.135 m, $\mathcal{R}$=80 % (d) L_2= 0.135 m, $\mathcal{R}$=80 %, T= 20°C (e) L_2= 0.57 m, $\mathcal{R}$=80 %

Figure 4.46: Laser beam profile at a distance 1.78 m (1.88 m in (d)) after the output coupler for various resonator configurations with output coupler R_2= 2 m. The temperature of the crystal was T_{opt}= 34 °C if not indicated otherwise. The absorbed pump energy was 115 mJ. The lasers with the BF were tuned at 1432 nm.

The beam propagation factor M^2 of both resonators was measured as described in Section 2.6.3. The focusing lens was a PLCX lens with nominal focal length of 500 mm which corresponds to f=620 mm at 1400 nm placed at 1.477 m after the output coupler. The transformation of the beam profile after the lens is presented in Figs. 4.47–4.50.

M^2 of the resonator with L_2= 0.135 m was measured for operation in the fundamental mode and multimode. The beam propagation factor was 1×1 for TEM_{00} and 3.6 × 3.7 for the multimode regime in the x- and y- planes, respectively. The beam was slightly astigmatic and the waist separation was about 10–20 mm. The beam divergence for TEM_{00} (Fig. 4.47) was estimated to 0.83×0.86 mrad in the sagittal and tangential plane, respectively, which agrees well with the predictions by the resonator design program (again using the thermal lens measured at 15 °C). The experimentally obtained divergence of the multimode beam was 1.6×1.7 mrad (Fig. 4.48). This is also consistent with the theoretical values predicted by Eq. 2.64 utilizing the measured M^2: 1.7×1.8 mrad. It is important to point out, that the beam was changing only size by focusing with the lens. The energy distribution remained unchanged in all planes.

As expected due to oscillation of lower order modes, the M^2 of the resonator with L_2=0.57 m was smaller: 1.8×1.76 (Fig. 4.49). The half angle beam divergence was 1–1.2 mrad. The beam was slightly astigmatic with 10-mm beam waist separation.

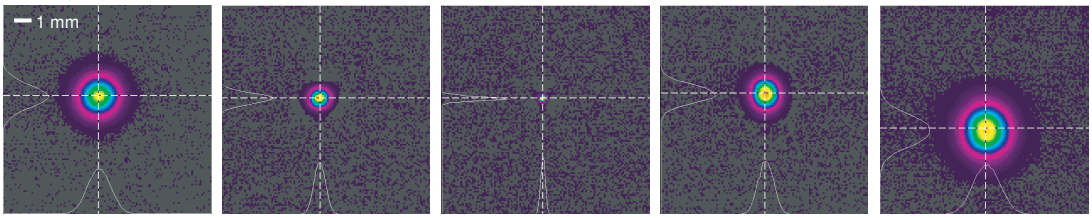

(a) d=0.18 m (b) d=0.5 m (c) d=0.75 m (d) d=1.2 m (e) d=1.53 m

Figure 4.47: Beam propagation after PLCX lens with focal length f=620 mm. The resonator configuration was L_1= 0.065 m, L_2= 0.135 m, R_2= 2 m, $\mathcal{R}$=80 %, with BF and T_{opt}= 34 °C. The laser was operating in the fundamental mode regime at 1432 nm wavelength. The distance from the lens d is indicated below each figure.

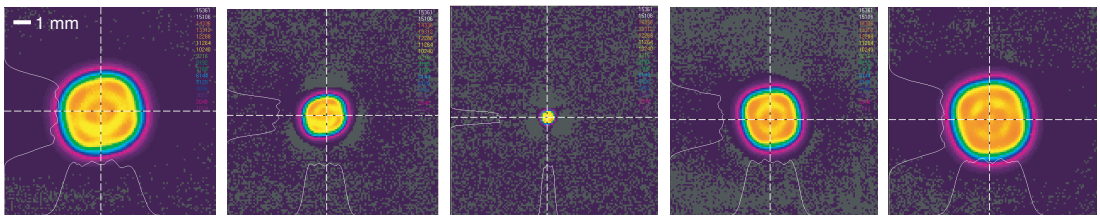

(a) d=0.18 m (b) d=0.48 m (c) d=0.75 m (d) d=1.23 m (e) d=1.48 m

Figure 4.48: Beam propagation after PLCX lens with focal length f=620 mm. The resonator configuration was L_1= 0.065 m, L_2= 0.135 m, R_2= 2 m, $\mathcal{R}$=80 %, with BF and T_{opt}= 34 °C. The laser was operating in multimode regime at 1432 nm. The distance from the lens d is indicated below each image.

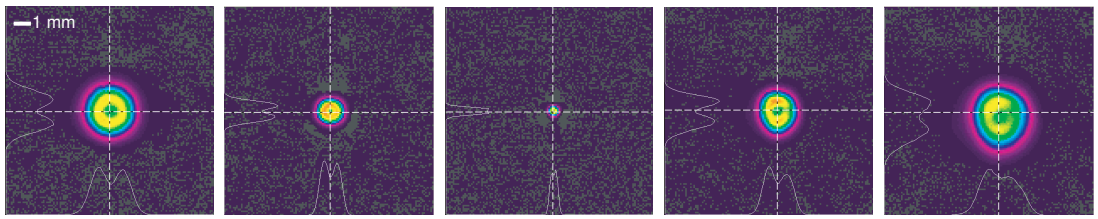

(a) d=0.18 m (b) d=0.49 m (c) d=0.75 m (d) d=1.23 m (e) d=1.48 m

Figure 4.49: Beam propagation after PLCX lens with focal length f=620 mm. The resonator configuration was L_1= 0.065 m, L_2= 0.57 m, R_2= 2 m, $\mathcal{R}$=80 %, with BF and T_{opt}= 34 °C. The laser was operating in multimode regime at 1454 nm. The distance from the lens d is indicated below each image.

The beam propagation factor of the shorter resonator without the BF was approximately the same as when the laser was tuned at 1432 nm: 3.3×3.4. The energy distribution was also similar (Fig. 4.50).

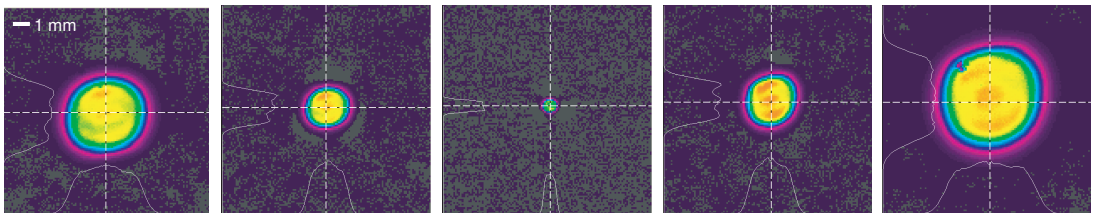

(a) d=0.18 m (b) d=0.48 m (c) d=0.75 m (d) d=1.18 m (e) d=1.58 m

Figure 4.50: Beam propagation after PLCX lens with focal length f=620 mm. The resonator configuration was L_1= 0.065 m, L_2= 0.135 m, $\mathcal{R}$=80 %, without BF and T_{opt}= 34 °C. The laser was operating in multimode regime. The distance from the lens d is indicated below each image.

Chapter 5

Summary

The goal of this project was to develop a Cr^{4+}:YAG wavelength converter for an eye-safe all-solid-state lidar transmitter. The transmitter was to be used for a ground-based mobile scanning backscatter lidar. Thus the main requirements for the wavelength converter included high average power, low beam divergence and a compact design. However, due to failure of one the components of the high-power diode laser pumped Nd:YAG laser of IBL followed by a delay in the delivery of the pump laser, this project was completed at NCAR, Boulder, using one of the EOL's Nd:YAG pump lasers. The pump laser was a flash-lamp pumped Q-switched Continuum Surelite III capable of delivering up to 850 mJ at 10 Hz.

The development of the Cr^{4+}:YAG wavelength converter included the following procedures and results:

– **Characterization of the pump laser**
Both pump lasers used in this study were first characterized in terms of output power, pointing stability, polarization and beam quality. The beam propagation factor was measured in order to calculate a suitable focusing configuration to pump the laser crystal (see Chapter 3).

– **Design of a vacuum spatial filter**
The IBL laser had a near Gaussian profile and allowed to pump the Cr^{4+}:YAG directly (without additional beam shaping) with energy up to 200 mJ. The Surelite pump laser had hot spots in the beam profile that can damage optical components, including the crystal, even for low pump energy. Therefore, a vacuum spatial filter was designed, built and applied to the Surelite pump laser to filter the hot spots of its beam. The VSF was ≈3 m long which is in contradiction to the design goal of a compact configuration. Furthermore, the VSF required periodic adjustment to maintain constant pressure which makes it unsuitable for unattended operation. However, with the VSF, a nearly Gaussian-shaped beam was obtained that enabled safe pumping of the Cr^{4+}:YAG crystal with pulse energies in excess of 100 mJ (see Section 3.2).

Therefore, the VSF was used to simulate pumping the laser crystal with a future high-power laser.

– **Investigation of the saturation behaviour of the pump radiation**
The conversion efficiency is proportional to the pumping efficiency. Therefore, the absorption of the pump radiation was considered.

The ground-state bleaching in Cr^{4+}:YAG was measured in a 20-mm long crystal with an initial absorption coefficient of $2.2\,cm^{-1}$ and pump energy fluence of up to $4\,J/cm^2$. The absorption of the crystal was 55–60 % for energy density $>1\,J/cm^2$. Based on this measurement and the aid of a theoretical model, the ground-state absorption cross-section and the ESA at the pump wavelength were determined. The obtained values of $\sigma_{GSA} = 5 \times 10^{-18}cm^2$ and $\sigma_{ESA_P} = 8 \times 10^{-19}cm^2$ are in good agreement with [39]. These parameters were used to calculate the length and the doping level of a new crystal required to increase the absorption to >95 %. The absorption of the new rod was higher compared to the shorter rod but not as high as predicted by the model. The new experimental data were fitted for a different value of the ESA ($\sigma_{ESA_P} = 4.8 \times 10^{-19}cm^2$) which agrees with [15] (see Section 4.2). This kind of a discrepancy in the ESA cross-section and consequently the saturation behavior of the crystal has also been reported by other groups. In fact, the published values of all cross-sections (GSA, SE and ESA at the pump and emission wavelengths) of Cr^{4+}:YAG differ from each other, some by an order of magnitude (see Tab. 4.2). Possible reasons for these discrepancies are: (i) the laser crystals were grown under different conditions, which affected the crystal's properties and (ii) the cross-sections were determined using different methods (spectroscopic measurement or theoretical fit with a model). The latter comes into consideration because the cross-sections can not be determined independently.

– **Investigation of the pump induced thermal lensing in the crystal**
The thermal lens was measured for average pump power ranging from 1.3 W to 32 W at PRFs of 10 Hz, 125 Hz, and 250 Hz (see Section 4.3 and Appendix C). In all these measurements the temperature of the crystal was stabilized to 15 °C. Strong thermal lensing was observed for pump power ≥ 13.5 W. The obtained values at 1.3 W were applied in the design of a dynamically stable resonator. The values of the thermal lens at higher pump powers can be implemented in the design of future Cr^{4+}:YAG lasers.

– **Extensive design of a dynamically stable resonator**
A program for calculating dynamically stable resonators utilizing one and two rods was written in Mathematica. It can be used to determine the resonator geometry for a given thermal lens and desired mode size at the crystal. The stability zone and the mode propagation in the cavity can be also plotted. Only a few resonator configurations with one rod were tested experimentally. An example of a two-rod cavity is

also presented in the Appendix D.

– **Experimental optimization of the output energy**
The laser performance in terms of output energy was investigated for a number of resonator configurations (see Section 4.5). As expected, low laser threshold of 15–20 mJ (∼0.15 J/cm^2) was obtained. An increase of the output energy of 15 % to 40 % (depending on the resonator configuration) for pump energy density of 1 J/cm^2 was achieved by enlarging the pump beam diameter at the crystal from 2 mm to 3 mm. This effect is attributed to the fact that a larger volume of the active medium was excited and consequently higher order transverse modes were generated. Further increase of the output energy by 12 % to 25 % was acquired by optimizing the crystal's temperature. The optimal temperature differed for each resonator configuration. In general, the optimal temperature for the maximum pump energy of 130 mJ (1 J/cm^2 for pump beam size of 3 mm) was ∼32–35 °C. A possible reason for this effect is that better mode matching was achieved for the optimal crystal temperature due to the corresponding thermal lensing. The temperature dependence of the ESA cross-section at the emission wavelength and the stimulated cross-section may have also contributed to the increase of output energy at higher temperatures.

– **Fit of the experimental data with the rate equation model**
Some of the power curves were fitted utilizing the rate equation model applied throughout this thesis. The ESA and SE cross-sections were determined from the fits (see Subsection 4.5.4). The obtained values $\sigma_{SE} = 2.65 \times 10^{-19}\text{cm}^2$ and $\sigma_{ESA_L} = 1.75 \times 10^{-19}\text{cm}^2$ are in a good agreement with [107].

– **Tunability and linewidth**
Tuning experiments of Cr^{4+}:YAG laser were performed using a 3-stage birefringent filter (see Section 4.6). The tunability range of 1360–1500 nm was demonstrated with peak output energy at 1430–1450 nm. A maximum of 7 mJ at 1432 nm and pulse duration of 35 ns was achieved. The spectral linewidth was ≈200 GHz.

– **Beam propagation factor**
The beam propagation factor for operation at the fundamental mode was 1. By generating higher order modes in order to extract more output energy the M^2 increased to ≈4 which corresponds to a half-ange divergence of ≈2 mrad. The beam profile was top-hat with some small scale inhomogeneities (see Subsection 4.6.3).

– **Suitability of Cr^{4+}:YAG laser as lidar trasmitter**
The Cr^{4+}:YAG laser developed in this work fulfills the requirements for short pulses and low beam divergence stated in Tab. 1.1. The laser is tunable in the 1400–1500 nm spectral range, which covers suitable water-vapor absorption lines for DIAL. The average power requirement was not met yet due to the use of a low PRF (10 Hz)

pump laser. However, the Cr^{4+}:YAG has a potential for higher pulse energy which is discussed in Chapter 6.

In the current configuration, the Cr^{4+}:YAG laser can be employed as an eye-safe transmitter for a non-scanning backscatter lidar after a narrow-band birefringent filter is installed. The low laser pulse energy poses a limit of the lidar performance. Therefore, integration over many laser shots would be essential in order to achieve a good SNR. Given that the laser operates at a PRF of 10 Hz, this will result in a temporal resolution on the order of a few minutes. However, a vertical pointing Cr^{4+}:YAG laser-based aerosol lidar will be very useful for monitoring boundary layer height. In addition, the lidar can be used to locate elevated aerosol layers from pollution, dust storms (Asian and African dust), distant forest fires, and volcanic activity.

Chapter 6

Conclusions and outlook

The Cr^{4+}:YAG laser developed in this project delivers comparable output energy to what was already demonstrated by Mathieu et. al [101]. However, previous research reports lack information about the design considerations, the laser mode operation, and the beam quality. This study provides important details regarding the design and optimization of the laser performance. The crystal properties and optimization of parameters such as active ion concentration and geometry of the rod are discussed. For first time, to the author's knowledge, the thermal focal length of Cr^{4+}:YAG was measured in pulsed mode. Moreover, the laser performance including linewidth, beam profile, and beam propagation factor were characterized. This is a sufficient set of data obtained with a single crystal that can be used together with additional spectroscopic measurements to model the performance of the laser.

The Cr^{4+}:YAG laser with maximum output energy of 7 mJ at 1430 nm at 10 Hz fulfills the requirements for short pulses ($\sim$35 ns) and sufficiently low divergence ($M^2 \approx 4$, which is acceptable for use in a lidar system utilizing InGaAs APDs in the receiver [147]). However, the size of the laser (including the pump laser, the vacuum spatial filter and the Cr^{4+}:YAG wavelength converter) restricts its use to the laboratory. In order to employ the laser in the field on a mobile platform, the pump laser must be exchanged with another pump laser with good beam profile that does not require the use of a VSF. In addition, the spectral linewidth of Cr^{4+}:YAG laser should be reduced to a few GHz, by using a different birefringent filter with narrow-band transmission (see Appendix 4.6.1) in order to avoid water vapor absorption.

The biggest limitation of Cr^{4+}:YAG is the low conversion efficiency at high pump pulse energy. In order to obtain a sufficient lidar signal-to-noise ratio for practical use, averaging backscatter for a few minutes will be required. Therefore, it is recommenced to increase the PRF to $\sim$100 Hz. Otherwise, such a laser can be employed in a vertically pointing lidar that provides altitude vs. time images of slowly changing atmospheric structures. For further improved performance of a vertically pointing lidar, or for applications of Cr^{4+}:YAG as a transmitter for a scanning lidar, more research is necessary towards increasing its output pulse energy. Based on the exper-

imental results obtained within this study, here are some recommendations of how to achieve higher output energy:

– Long (6–8 cm) or multiple highly doped ($\geq 10^{18}\,\mathrm{cm}^{-3}$ if possible) crystals with diameters ∼5–7 mm should be used in order to improve the pumping efficiency (by maximizing the absorption of the pump energy) and consequently the conversion efficiency at high pump pulse energy. For high PRF, a slab geometry of the crystal can be considered for more efficient cooling.

– The pump beam should have a large diameter approaching the diameter of the rod in order to generate high order modes and extract energy of the larger volume of the low gain active medium. The pump energy fluence can be close to full saturation of the pump radiation ($\sim 1\,\mathrm{J/cm}^2$). Thus, it is recommended to use a smooth top-hat profile rather than a Gaussian. Due to the low pump fluence, the rod can have plane anti-reflection coated end surfaces instead of Brewster-cut. This will allow one to exploit the crystal cross-section more efficiently. Also, by using an AR coated rod, the proper orientation of the crystal can be easily determined whereas for a Brewster angled crystal if the plane of incidence of these cuts is not properly oriented with the crystallographic axis, the laser performance decreases.

– The temperature of the crystal should be optimized experimentally. Most likely the optimal temperature is near or above room temperature.

– The shortest possible stable resonator should be chosen in order to generate high order modes.

– The crystals should be pumped from both ends, each with maximum energy fluence $\sim 1\,\mathrm{J/cm}^2$, in order to create more homogeneous gain.

– It is desirable to use an injection-seeded single longitudinal mode pump laser and injection-seed the Cr^{4+}:YAG laser. This will result in narrower spectral linewidth and lower M^2 factor [173].

After performing these improvements the output energy may be increased by a factor of 2–3. The main limitations for high output energy are the ESA of the pump and the emission wavelengths.

An alternative is a RISTRA OPO [7], which provides very high single shot pulse energy. The RISTRA OPO has not yet been applied as a lidar transmitter. However, given the achieved beam parameters it has potential for good lidar performance. Moreover, as a solid-state tunable transmitter, that also features a compact design, it can potentially be employed in an airborne DIAL.

Another option is stimulated Raman scattering in methane [148], that offers output pulse energy >100 mJ. The performance of a scanning lidar using a Raman shifter has been successfully demonstrated with the Raman-shifted Eye-safe Aerosol Lidar (REAL) [148]. REAL operates in the field unattended with 150–200 mJ pulse energy at 10 Hz. Recently, Spuler and Mayor [147] produced up to 390 mJ pulse energy at 50 Hz in the laboratory by pumping the Raman cell with ∼900 mJ. This corresponds to ≈40 % conversion efficiency. They achieved good beam quality and a narrow spectral line. Therefore, REAL is currently the only eye-safe high pulse energy scanning

lidar that can gather aerosol backscatter at distances on the order of 5–10 km without averaging backscatter from multiple pulses. This capability enables capturing rapidly evolving atmospheric structures and dispersion of aerosol plumes. It is unlikely that so much energy at 1500 nm can be produced by using a solid-state wavelength converter, such as KTP and Cr^{4+}:YAG, due to much lower damage threshold. Unfortunately, the REAL transmitter is tunable only over 1 nm [147], which with the current pump wavelength and gas, does not span across a water-vapor absorption line.

Cr^{4+}:YAG has the unique capability of generating tunable radiation in the 1400–1500 nm wavelength region. This unique feature makes it more suitable for water vapor DIAL. Lidar operation around 1450 nm has not been demonstrated with an OPO. This application of Cr^{4+}:YAG requires, in addition to the effort for increasing the output energy, frequency stabilization and narrowing the spectral linewidth to a few 100's of MHz. The knowledge achieved within this thesis is a unique basis for the design and performance of future high-power, pulsed, high-repetition rate Cr^{4+}:YAG lasers.

Appendix A

Suitable water vapor absorption lines for DIAL

Based on simulations of the performance of a water-vapor differential lidar (DIAL) in the troposphere, Wulfmeyer and Walther [181, 182] have determined the optimal parameters for water vapor absorption lines. Suitable absorption lines must have line strength on the order of $10^{-24} - 10^{-22}$ cm and ground-state energy $< 300\,\mathrm{cm}^{-1}$. Also, for a sufficient resolution and range, the differential optical thickness (optical depth) must be between 0.03 and 0.1 [179].

Water vapor absorption lines in the spectral range of 1400–1550 nm and meeting the above requirements were selected from the spectroscopic database HITRAN [124] and presented in Fig. A.1. There are approximately 200 potential absorption lines for water vapor DIAL in this wavelength region. The optical depth for these lines was calculated using a standard atmosphere and 100-m path length. Many of the lines have optical depth outside the determined interval and/or overlap with other water-vapor absorption lines. Only a few suitable absorption lines were chosen. They are listed in Tab. A.1 and are indicated in the plots of the optical depth (Figs. A.2 and A.3). Some of the potential lines (with the right strength, ground-state energy and optical depth, but overlapping) are also marked for a comparison.

The standard atmosphere conditions correspond to a mixing ratio $m_r = 4.8\,\mathrm{g/kg}$ (the mass of the water vapor to the mass of dry air in unit volume). For a constant temperature the optical depth is proportional to the mixing ratio. For example, an increase of the water vapor content by a factor of two ($m_r = 9.6\,\mathrm{g/kg}$) results in an increase of the optical depth also by a factor of two. Thus, the absorption line e.g. at 1458.68 nm will be still a good choice for the measurement. The line at 1502.75 nm, on the other hand, will have very large optical depth of 0.22. In order to ensure the same resolution and range, the laser wavelength must be tuned off the center of the line to a place with optical depth 0.03–0.1. In the opposite case of a drier air, the absorption line at 1458.68 nm will not have sufficient optical depth but the line at 1502.75 nm will be still within the required range.

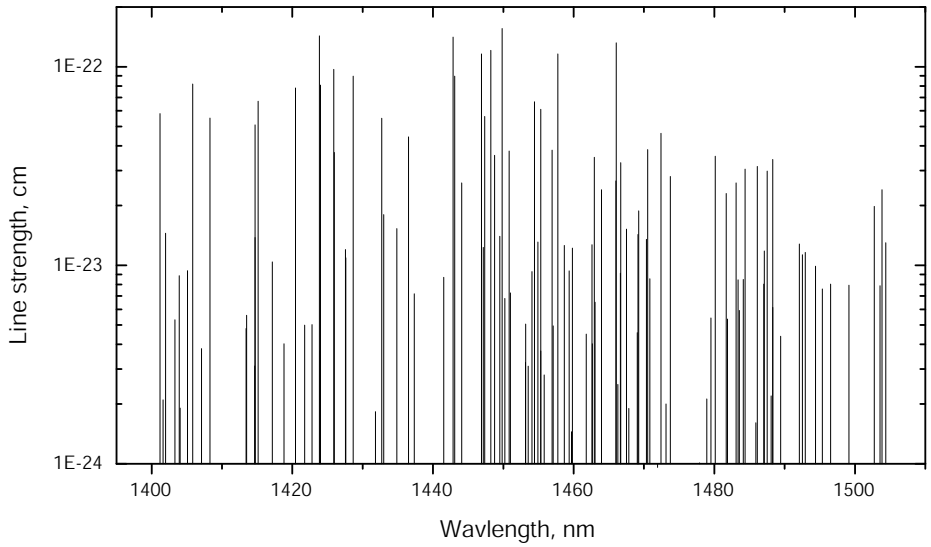

(a) Line strength

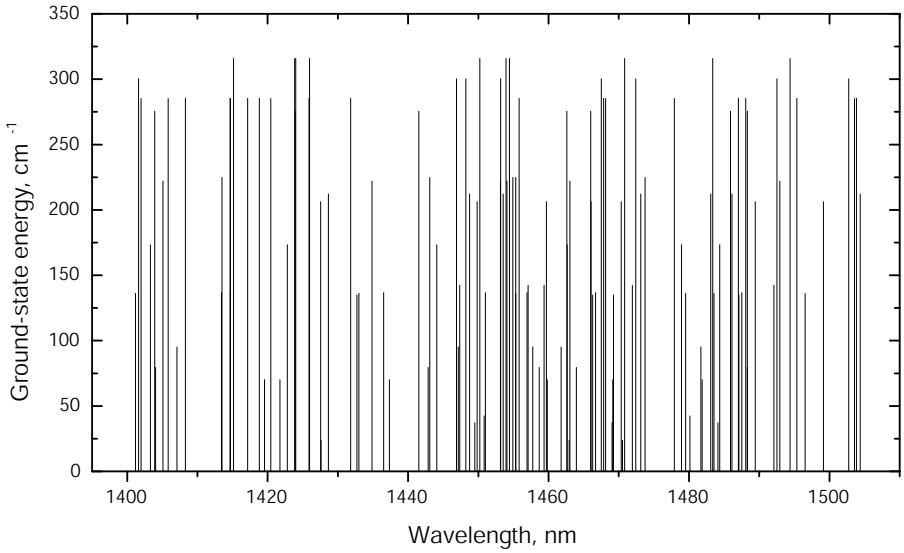

(b) Ground-state energy

Figure A.1: Water-vapor absorption lines in the spectral region 1400–1550 nm with line strength of $10^{-24} - 10^{-22}$ cm and ground-state energy $< 320\,\mathrm{cm}^{-1}$.

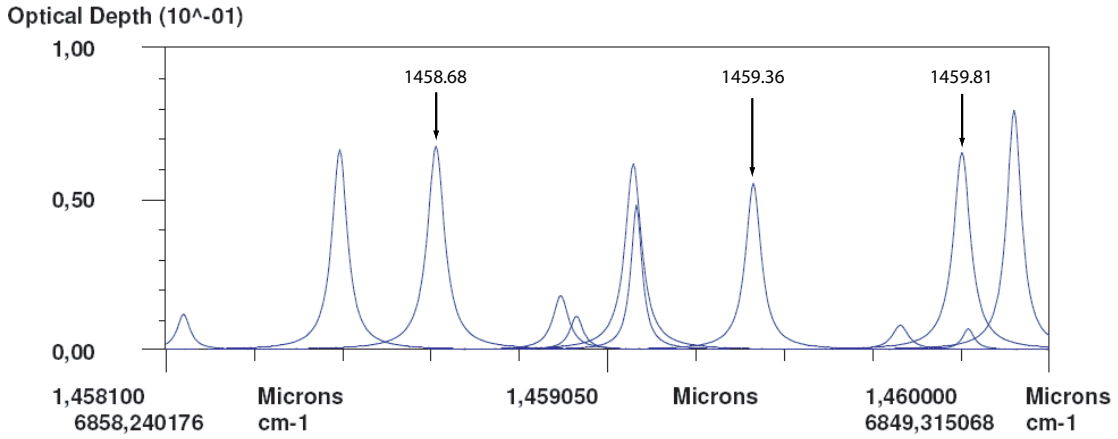

(a) spectral region around 1458 nm

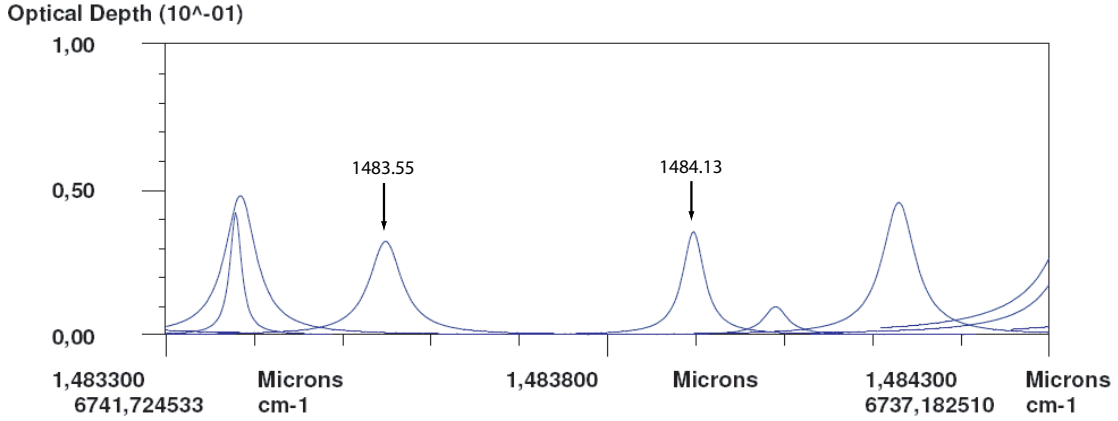

(b) spectral region around 1484 nm

Figure A.2: Optical depth of water vapor absorption lines in different spectral regions for standard atmosphere (altitude: sea level, air temperature: 296 K, partial pressure: 775 Pa) and 100 m path length.

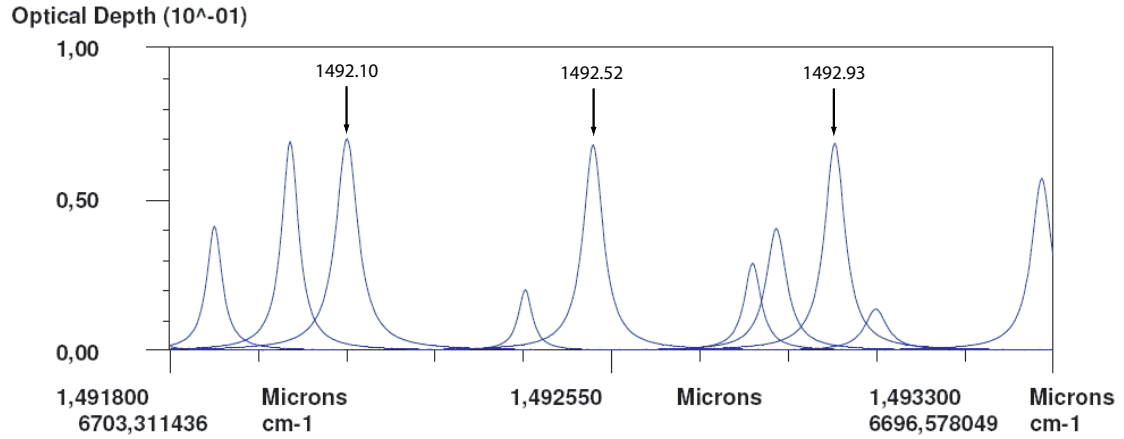

(a) spectral region around 1492 nm

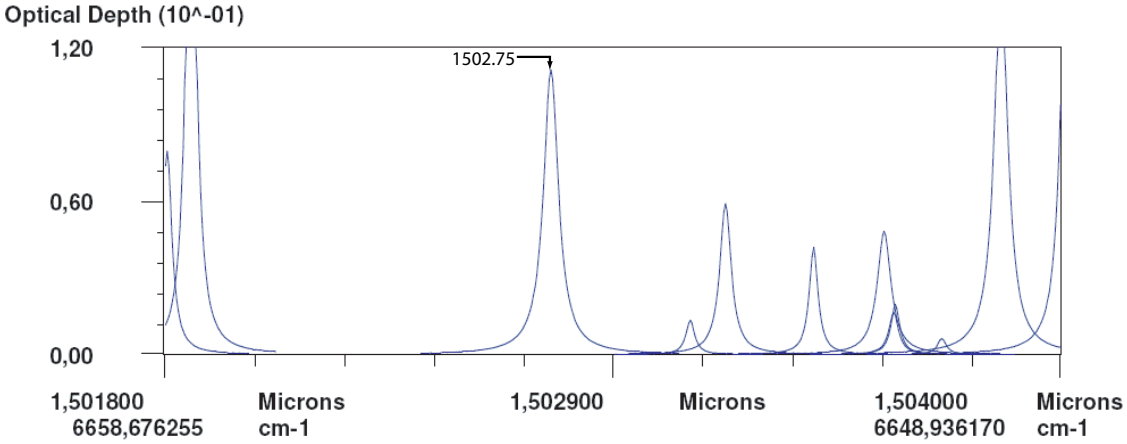

(b) spectral region around 1500 nm

Figure A.3: Optical depth of water vapor absorption lines in different spectral regions for standard atmosphere (altitude: sea level, air temperature: 296 K, partial pressure: 775 Pa) and 100 m path length.

Table A.1: Suitable water vapor absorption lines for ground-based DIAL. The optical depth corresponds to standard atmosphere (altitude: sea level, air temperature: 296 K, partial pressure: 775 Pa) and 100-m path length.

Wavelength, nm	Line strength, cm	Lower state energy, cm^{-1}	Optical depth
1458.680728	1.26×10^{-23}	79.496	0.037
1459.364597	9.38×10^{-24}	142.279	0.076
1483.548218	5.92×10^{-24}	136.164	0.036
1484.129635	8.49×10^{-24}	37.137	0.052
1492.51751	1.13×10^{-23}	300.362	0.076
1502.754902	1.98×10^{-23}	300.362	0.12

Appendix B

Ray transfer matrix

Ray transfer matrix describing beam propagation through a medium with length l and index of refraction n

$$\begin{pmatrix} A & B \\ C & D \end{pmatrix} = \begin{pmatrix} 1 & \frac{l}{n} \\ 0 & 1 \end{pmatrix}. \tag{B.1}$$

Ray transfer matrix for a thin lens with focal length f

$$\begin{pmatrix} A & B \\ C & D \end{pmatrix} = \begin{pmatrix} 1 & 0 \\ -\frac{1}{f} & 1 \end{pmatrix}. \tag{B.2}$$

Ray transfer matrix for a curved mirror with radius of curvature R

$$\begin{pmatrix} A & B \\ C & D \end{pmatrix} = \begin{pmatrix} 1 & 0 \\ -\frac{2}{R} & 1 \end{pmatrix}. \tag{B.3}$$

Ray transfer matrix for a tilted slab with length l and index of refraction n in the tangential plane. θ_i and θ_r are the angles of incidence and refraction, respectively.

$$\begin{pmatrix} A & B \\ C & D \end{pmatrix} = \begin{pmatrix} 1 & \frac{L}{n} \cdot \left(\frac{\cos\theta_\mathrm{i}}{\cos\theta_\mathrm{r}}\right)^2 \\ -\frac{2}{R} & 1 \end{pmatrix}. \tag{B.4}$$

In the sagittal plane the ray transfer matrix is for an aligned slab given by Eq. B.1.

Appendix C

Thermal lensing of Cr^{4+}:YAG for PRF 125 Hz and 250 Hz

The thermal lens of the 40-mm crystal was measured with the IBL laser for average pump power ranging from 13.5 W (at 125 Hz) to 32 W (at 250 Hz). The experimental set up was as illustrated in Fig. 4.7. Due to strong thermal lensing no additional lens was used after the crystal. The pump beam size at the crystal was slightly different when the laser operated at different PRFs and consequently the absorption of the pump radiation was different. Therefore, the thermal focal length is presented as a function of the absorbed pump power in Fig. C.1. The relative error was less than 10 %.

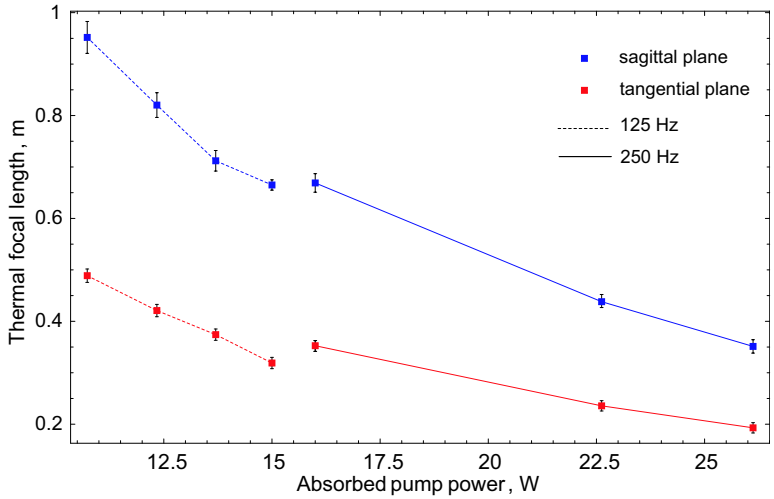

Figure C.1: Thermal lens focal length as a function of the absorbed pump power. The pump laser was operated at 125 Hz and 250 Hz. The pump beam radius at the crystal was 1.1 mm for 125 Hz and 1.25 mm for 250 Hz. The temperature of the crystal was stabilized to 15 °C. The error bars represent the absolute error.

Appendix D

Two-rod resonator

In order to generate higher output energy, two Cr^{4+}:YAG rods should be tested, pumped from opposing ends (Fig. D.1).

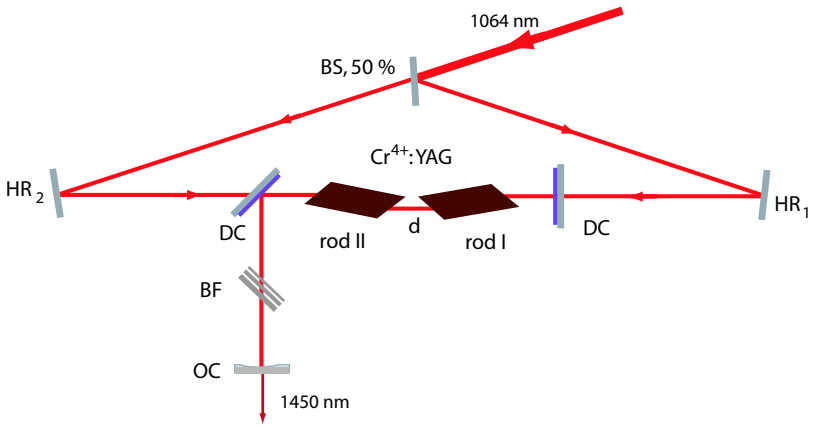

Figure D.1: Experimental arrangement for a two-rod cavity pumped from opposing ends with the equivalent pump energy. BS: 50 % beam splitter, HR: high reflectivity mirror, DC: dichroic mirror with high transmission of the pump wavelength and high reflectivity for the emission wavelength, BF: birefringent filter, OC: output coupler.

Based on the method presented in Section 2.5, and the measured thermal lensing for a 130 mJ pump pulse energy, dynamically stable configurations are calculated for a two-rod resonator. It is assumed 130 mJ of incident energy on each crystal that induces thermal focal length f_{tan}=4.5 m and f_{sag}=15 m. The rear mirror is flat and the beam radius at the first rod is ω_3=0.5 mm. The resonator configurations are calculated by varying the distance L_1 between the rear mirror and the first rod and the distance d between the rods. The results for the tangential and the sagittal plane are presented in Figs. D.2–D.5. An example for the stability zones and the mode propagation of one of the dynamically stable configurations is presented in Figs: D.6 and D.7, respectively.

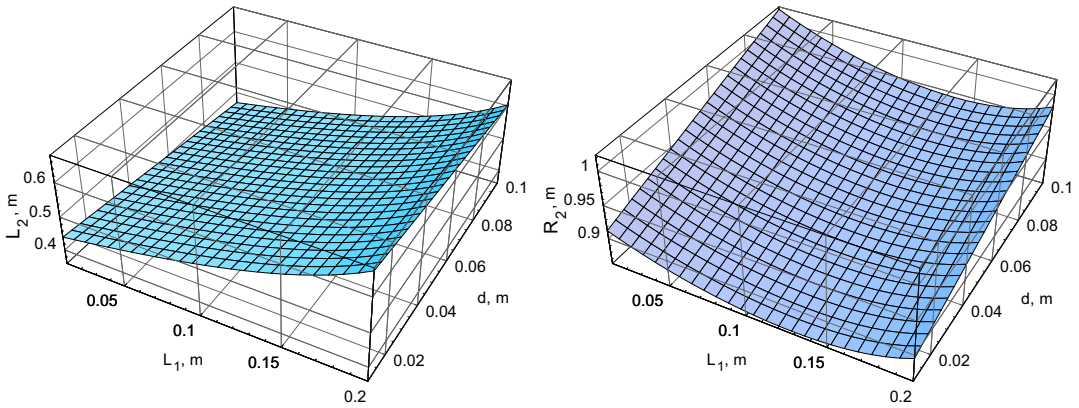

(a) distance between the second rod and the output coupler

(b) radius of curvature of the output coupler

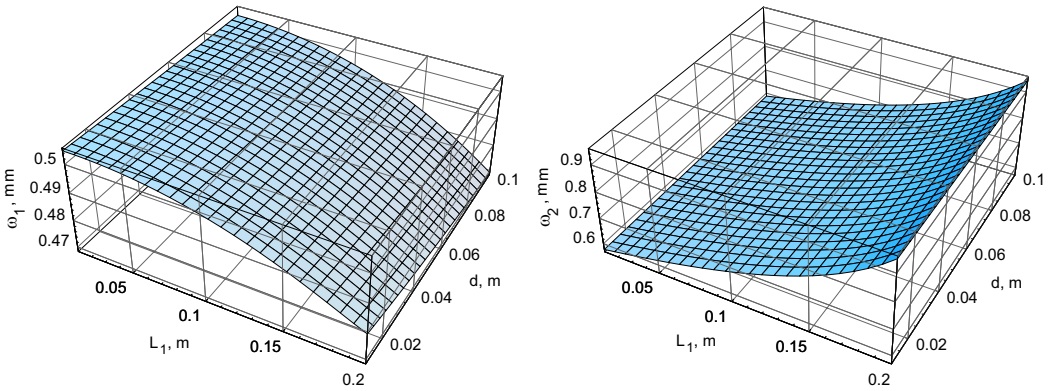

(c) beam radius at the rear mirror

(d) beam radius at the output coupler

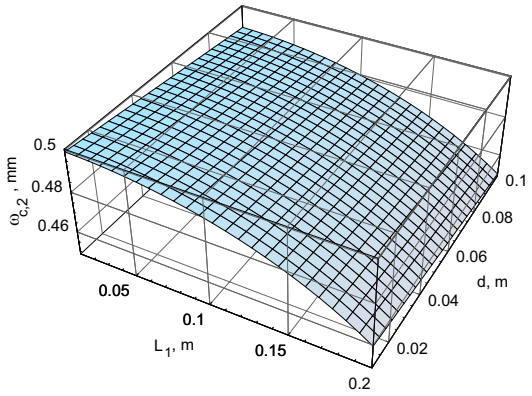

(e) beam radius at the second rod

Figure D.2: Resonator parameters as a function of the distance between the rear mirror and the first rod L_1 and the distance between the rods d in the tangential plane. The rear mirror is flat, the beam radius at the first rod is 0.5 mm, f_{tan}=4.5 m for both rods.

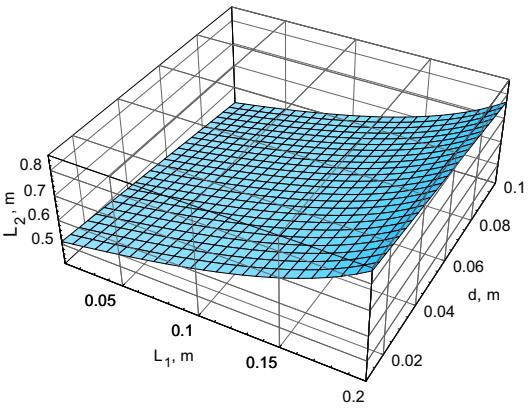

(a) distance between the second rod and the output coupler

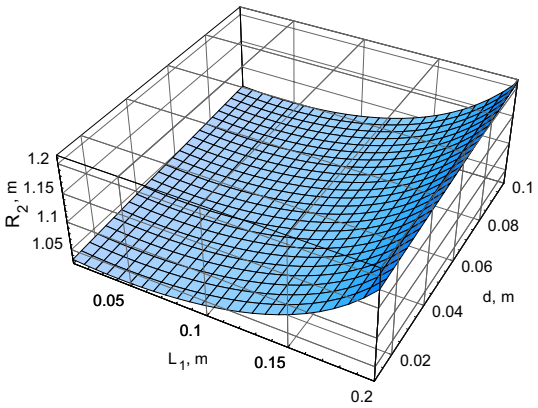

(b) radius of curvature of the output coupler

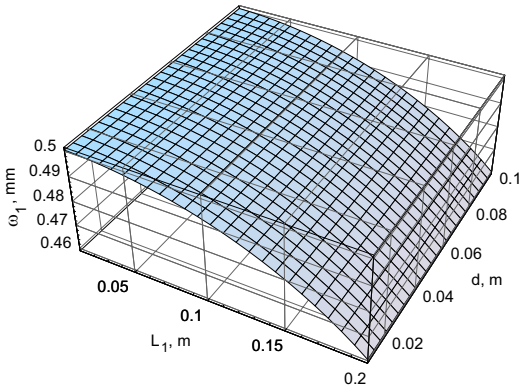

(c) beam radius at the rear mirror

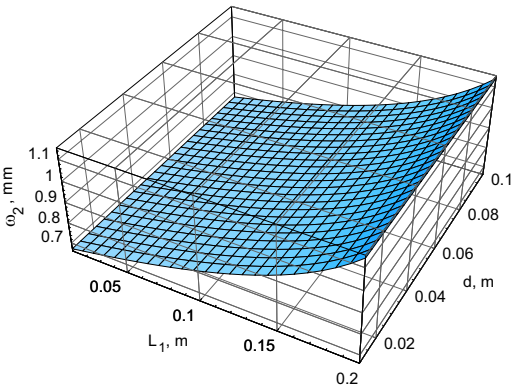

(d) beam radius at the output coupler

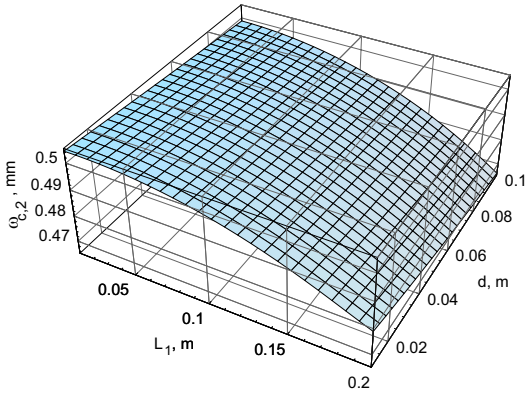

(e) beam radius at the second rod

Figure D.3: Resonator parameters as a function of the distance between the rear mirror and the first rod L_1 and the distance between the rods d in the sagittal plane. The rear mirror is flat, the beam radius at the first rod is 0.5 mm, f_{sag}=15 m for both rods.

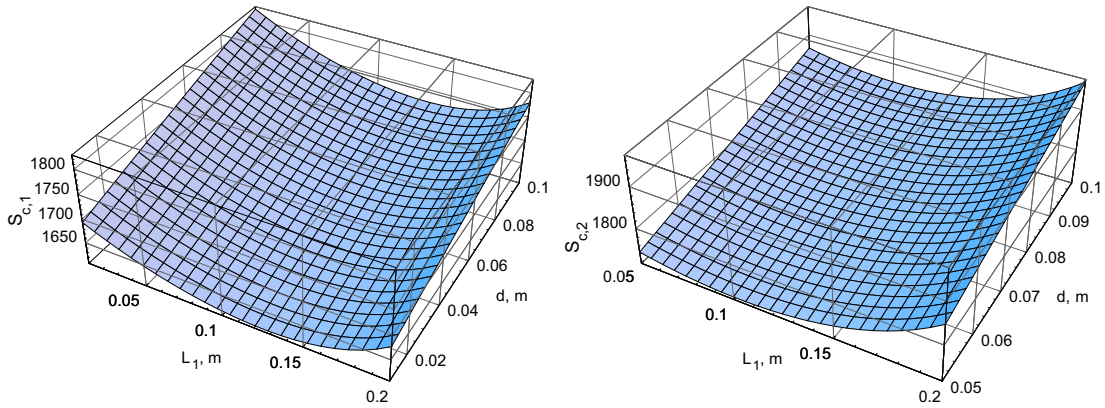

(a) misalignment sensitivity of the first rod (b) misalignment sensitivity of the second rod

Figure D.4: Sensitivity of the laser rods to misalignment of the cavity mirrors as a function of the distance between the rear mirror and the first rod L_1 and the distance between the rods d in the tangential plane. The rear mirror is flat, the beam radius at the first rod is 0.5 mm, f_{tan}=4.5 m for both rods.

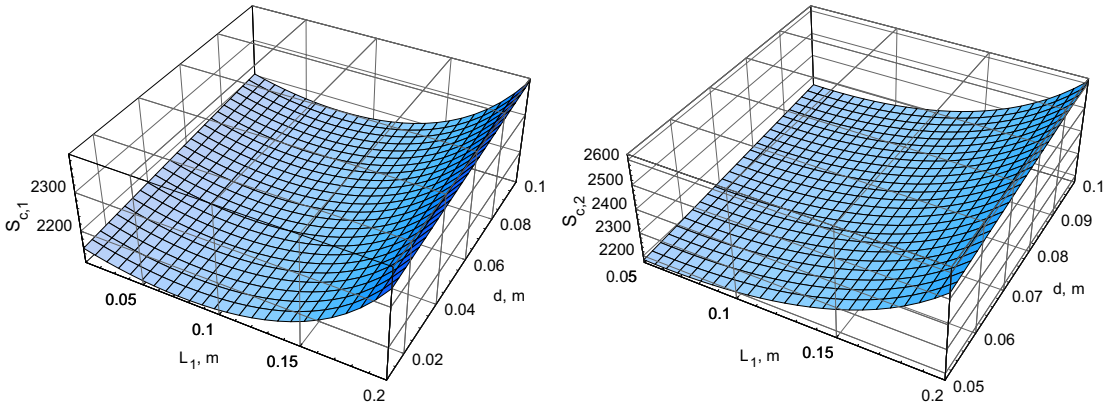

(a) misalignment sensitivity of the first rod (b) misalignment sensitivity of the second rod

Figure D.5: Sensitivity of the laser rods to misalignment of the cavity mirrors as a function of the distance between the rear mirror and the first rod L_1 and the distance between the rods d in the sagittal plane. The rear mirror is flat, the beam radius at the first rod is 0.5 mm, f_{sag}=15 m for both rods.

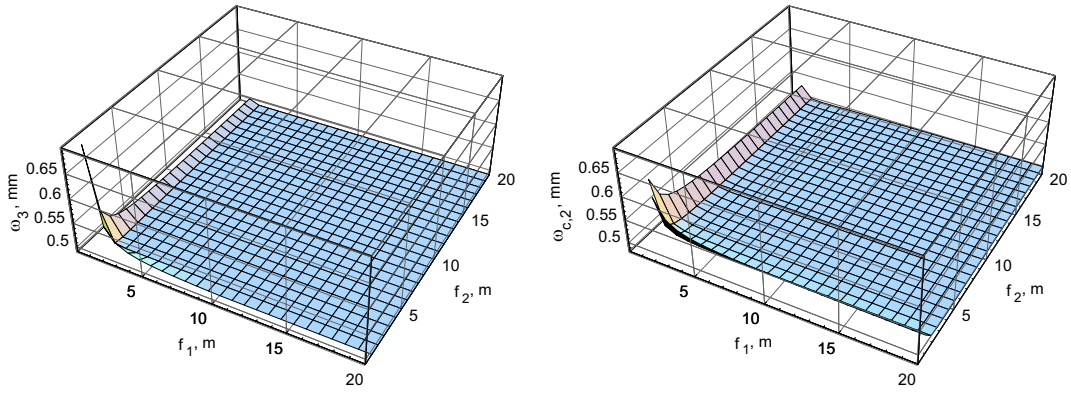

(a) beam radius at the first rod as a function of the thermal focal length of both crystals

(b) beam radius at the second rod as a function of the thermal focal length of both crystals

Figure D.6: Stability zones for the resonator with $R_1{=}\infty$ m, $L_1{=}0.05$ m, $R_2{=}1$ m, $L_2{=}0.45$ m, and $d{=}0.02$ m.

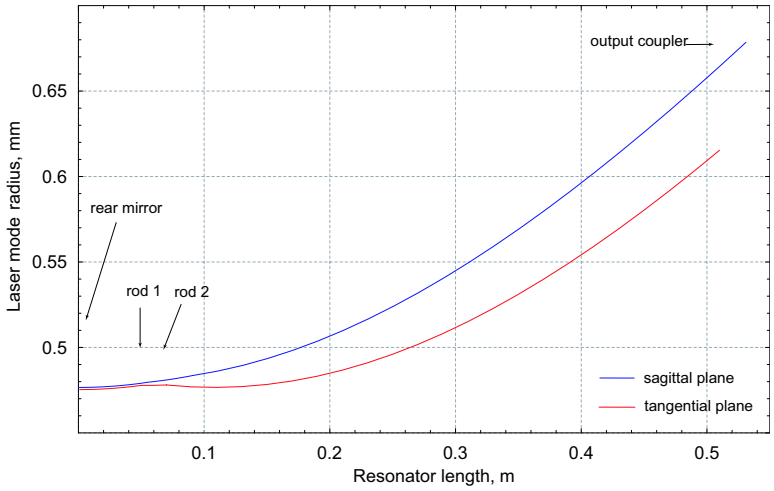

Figure D.7: Propagation of the fundamental laser mode in a 2-rod resonator. The resonator configuration is as follows: $R_1{=}\infty$ m, $L_1{=}0.05$ m, $R_2{=}1$ m, $L_2{=}0.45$ m, $d{=}0.02$ m, $f_{tan}{=}4.5$ m and $f_{sag}{=}15$ m for both rods.

Appendix E

Birefringent filter

In order to use Cr^{4+}:YAG laser as a transmitter for backscatter lidar, it should be tuned to a wavelength that is not absorbed by water vapor. For a standard atmosphere and 100-m path length suitable lines close to the gain peak of Cr^{4+}:YAG laser are 1416.2 nm, 1430.5 nm, 1453.8 nm and 1464.6 nm. In addition, the spectral linewidth should be on the order of a few GHz. Here, a 5-stage birefringent filter is suggested that has optimal performance ($\gamma \approx 45^{\circ}$, Section 4.6.1) for those wavelengths and features narrow-band-transmission. The transmission of the BF as a function of the wavelength for one pass is presented in Fig. E.1. A transmission maximum, e.g. at 1430.5 nm is obtained for rotational angle $\gamma = 51^{\circ}$, and at 1464.6 nm for $\gamma = 44.6^{\circ}$.

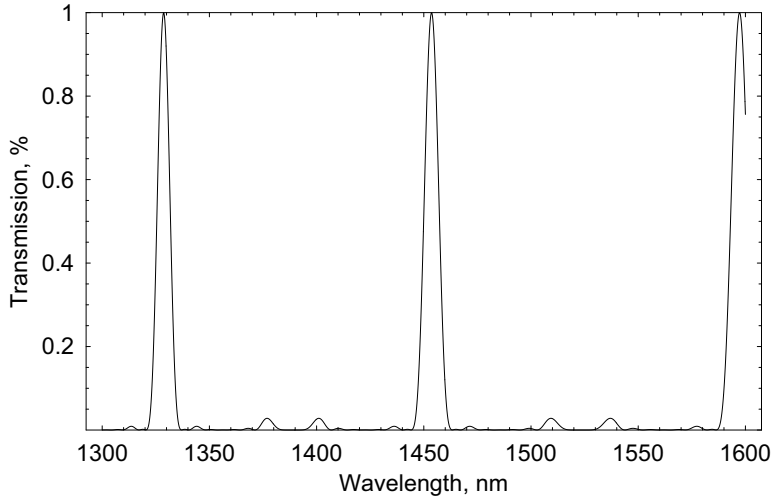

Figure E.1: Transmission of a 5-stage birefringent filter for single pass. The thickness of the birefringent plates is in a ratio 1:2:3:5:7 with the thinnest plate being 1.7 mm. The FWHM is 7.4 nm. The angle of rotation for transmission maximum at 1453.8 nm is 46.7°.

Appendix F

Grating spectrometer

A spectrometer using a blazed reflection grating in a Czerny-Turner configuration is shown schematically in Fig. F.1.

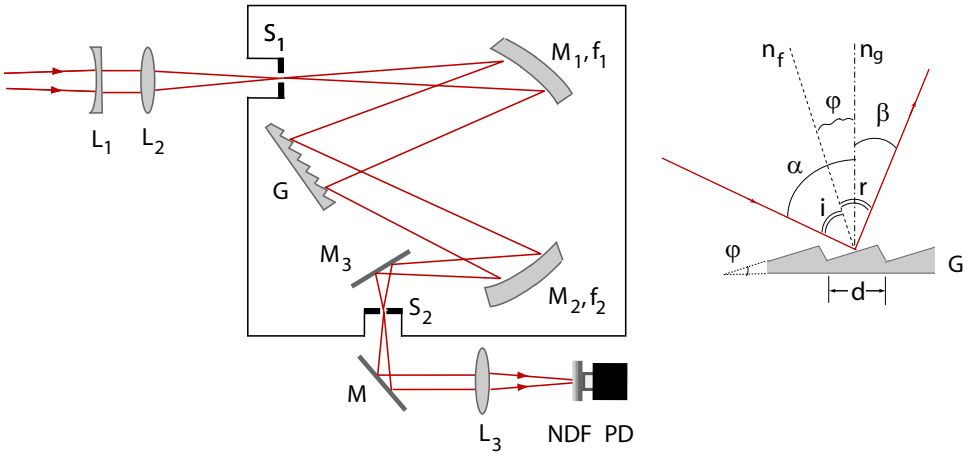

Figure F.1: Grating spectrometer in Czerny-Turner configuration. The box indicates the spectrometer. L_1, L_2: lens combination to match the f-number of the spectrometer, S_1, S_2: entrance and exit slits, M_1, M_2: aluminum coated curved mirrors with focal length f_1 and f_2, respectively, G: reflective diffraction grating, M_3, M: aluminum coated folding mirrors, L_3: focusing lens, NDF: neutral density filter, PD: photo detector. On the left hand side is shown diffraction of the blazed reflecting grating. , α and β: angles of incidence and diffraction, respectively, measured from the normal n_g to the surface of the grating, i and r: angles of incidence and reflection of the facet surface, respectively, measured from the normal n_f of the facet surface, φ: blaze angle, d: groove spacing

The fundamental grating equation is [34, 56]

$$d(\sin\alpha + \sin\beta) = m\lambda,\ m = 0,\ \pm1,\ \pm2, ... \tag{F.1}$$

Here, α and β are the angles of incidence and diffraction, respectively, m is the diffraction order, λ is the wavelength, and d is the groove spacing which is the reciprocal value of the groove density of the grating (in grooves/mm). In the spectrometer, the location of the entrance and exit slits are fixed and the grating rotates around a plane through the center of its face (see Fig. 4.38). The angle, $(\beta - \alpha)$ is, therefore, a constant. By rotating the grating and thus changing the incident angle, constructive interference in direction β is obtained for wavelengths which satisfy Eq. F.1.

The efficiency of the grating can be enhanced for a desired wavelength and diffraction order (usually m=1) by fabricating the reflecting facets so that the direction of the exit rays coincides with specular reflection of the entrance rays off the facet faces ($r = i$), as illustrated in Fig. F.1. For a fixed angle of incidence α, the facet angle φ can be chosen so that the corresponding exit angle β satisfies the specular reflection condition $\beta = 2\,\varphi - \alpha$ for a specific set of wavelengths for the various orders of interference. These wavelengths are called blazed wavelengths for the various orders and φ is the blazed angle.

The theoretical resolving power of the spectrometer is proportional to the total number of illuminated grooves and the diffraction order.

$$R_P = \frac{\lambda}{\Delta\lambda} = mN. \tag{F.2}$$

The maximum resolution is achieved when the beam illuminates the full width of the grating i.e. the f-number of the incident beam matches the f-number of the collimating mirror M_1. The f-number is defined as the ratio of the focal length to the diameter of the entrance pupil. Another factor influencing the resolution of the instrument is the width of the entrance and exit slits. The opening s of the slits determines the spectral bandpass. When the slits are so wide that diffraction can be neglected, the wavelength interval $\Delta\lambda$ is defined by geometrical factors only: the angular dispersion A_ν and the angular width of the wider slit:

$$\Delta\lambda = (s_j/f_j)\, A_\nu, \quad \text{with } j = 1, 2. \tag{F.3}$$

Bibliography

[1] A. J. Alcock, P. Scorah, and K. Hnatovsky. Broadly tunable continuous-wave diode-pumped Cr^{4+}:YAG laser. *Opt. Commun.*, 215:153–157, 2002.

[2] N. B. Angert, N. I. Borodin, V. M. Garmash, V. A. Zhinyuk, A. G. Okhrimchuk, and A. V. Shestakov. Lasing due to impurity color centers in yttrium aluminum garnet crystals at wavelengths in the range 1.35–1.45 μm. *Sov. J. Quant. Electron.*, 18:73–74, 1988.

[3] American National Standard for the Safe Use of Lasers ANSI. Standard for the safe use of lasers. Technical Report ANSI Z136.1-2000, American National Standards Institute, New York, 2000.

[4] G. Arisholm, E. Lippert, G. Rustad, and K. Stenersen. Efficient conversion from 1 to 2 μm by a KTP-based ring optical parametric oscillator. *Opt. Lett.*, 27:1336–1338, 2002.

[5] G. Arisholm, Ø. Nordseth, and G. Rustad. Optical parametric master oscillator and power amplifier for efficient conversion of high-energy pulses with high beam quality. *Opt. Eng.*, 12:4189–4197, 2004.

[6] D. J. Armstrong and A. V. Smith. Demonstration of improved beam quality in an image-rotating optical parametric oscillator. *Opt. Lett.*, 27:40–42, 2002.

[7] D. J. Armstrong and A. V. Smith. 150-mJ 1550-nm KTA OPO with good beam quality and high efficiency. In *Proceedings of SPIE*, volume 5337, pages 71–80. SPIE, Bellingham, WA, 2004.

[8] P. Avizonis and R. Grotbeck. Experimental and theoretical ruby laser amplifier dynamics. *J. Appl. Phys.*, 37:687–693, 1996.

[9] R. Bascom, P. A. Bromberg, D. A. Costa, R. Devlin, D. W. Dockery, M. W. Frampton, W. Lambert, J. M. Samet, F. E. Speizer, and M. Utell. Health effects of outdoor air pollution, Part 2. *Am. J. Respir. Crit. Care Med.*, 153:477–498, 1996.

[10] P. Baues. Huygens' principle in inhomogeneous, isotropic media and a general integral equation applicable to optical resonators. *Opto-Electronics*, 1:37–44, 1969.

[11] H. Baumhacker, G. Brederlow, E. Fill, R. Volk, S. Witkowski, and K. J. Witte. Layout and performance of the Asterix IV iodine laser at MPQ, Garching. *Appl. Phys. B*, 61:325–332, 1995.

[12] A. Behrendt, V. Wulfmeyer, P. Di Girolamo, C. Kiemle, H. S. Bauer, T. Schaberland D. Summa, D. N. Whiteman, B. B. Demoz, E. V. Browell, S. Ismail, R. Ferrare, S. Kooi, G. Ehret, and J. Wang. Intercomparison of water vapor data measured with lidar during IHOP_2002. Part I: Airborne to ground-based lidar systems and comparisons with chilled-mirror hygrometer radiosondes. *J. Atmos. Ocean. Technol.*, 24:3–21, 2007.

[13] A. L. Bloom. Modes of a laser resonator containing tilted birefringent plates. *J. Opt. Soc. Am.*, 64:447–452, 1974.

[14] R. Boers, E. W. Eloranta, and R. L. Coulter. Lidar observations of mixed layer dynamics: tests of parameterized entrainment models of mixed layer growth rate. *J. Appl. Meteor.*, 23:247–266, 1984.

[15] N. I. Borodin, V. A. Zhitnyuk, A. G. Okhrimchuk, and A. V. Shestakov. Oscillation of a $Y_3Al_5O_{12}$:Cr^{4+} laser in wavelength region 1.34–1.6 μm. *Bull. Acad. Sci. USSR, Phys. Ser.*, 54:54–60, 1990.

[16] J. Bösenber. Ground-based differential absorption lidar for water-vapor profiling: methodology. *Appl. Optics*, 37:3845–3860, 1998.

[17] E. Browell, A. Carter, S. Shipley, R. Allen, C. Butler, M. N. Mayo, J. H. Siviter Jr., and W. M. Hall. NASA multipurpose airborne DIAL system and measurements of ozone and aerosol profiles. *Appl. Optics*, 22:522–534, 1983.

[18] E. V. Browell, S. Ismail, and W. B. Grant. Differential absorption lidar (DIAL) measurements from air and space. *Appl. Phys. B*, 67:399–410, 1998.

[19] E. V. Browell, T. D. Wilkerson, and T. J. McIlrath. Water vapor differential absorption lidar development and evaluation. *Appl. Optics*, 18:3474–3482, 1979.

[20] E.V. Browell. Differential absorption lidar sensing of ozone. *Proc. IEEE*, 77:419–432, 1989.

[21] S. Camacho-Lopez, R. P. M. Green, G. J. Crofts, and M. J. Damzen. Intensity-induced birefringence in Cr^{4+}:YAG laser. *J. Mod. Opt.*, 44:209–219, 1997.

[22] W. Carnuth and T. Trickl. A powerful eyesafe infrared aerosol lidar: Application of stimulated Raman backscattering of 1.06 micron radiation. *Rev. Sci. Instr.*, 65:3324–3331, 1994.

[23] P. M. Celliers, K. G. Estabrook, R. J. Wallance, J. E. Murray, L. B. Da Silva, B. J. MacGowan, B. M. Van Wonterghem, and K. R. Manes. Spatial filter pinhole for high-energy pulsed lasers. *Appl. Optics*, 37:2371–2378, 1998.

[24] Y. F. Chen. Efficient 1521-nm Nd:$GdVO_4$ Raman laser. *Opt. Lett.*, 29:2632–2634, 2004.

[25] Y. F. Chen. High-power diode-pumped actively Q-switched Nd:$GdVO_4$ self-Raman laser: influence of dopant concentration. *Opt. Lett.*, 29:1915–1917, 2004.

[26] H. H. Chu, S. Y. Huang, L. S. Yang, T. Y. Chien, Y. F. Xiao, J. Y. Lin, S. Y. Chen, and J. Wang. A versatile 10–TW laser system with robust passive controls to achieve high stability and spatiotemporal quality. *Appl. Phys. B*, 79:193–201, 2004.

[27] A. J. Cohen, H. R. Anderson, B. Ostro, K. D. Pandeyand M. Krzyzanowski, N. Kunzli, K. Gutschmidt, C. A. Pope III, I. Romieu, J. M., and K. Smith. The global burden of disease due to outdoor air pollution. *Journal of Toxicology and Environmental Health Part A*, 68:1–7, 2005.

[28] S. A. Cohn and W. M. Angevine. Boundary layer height and entrainment zone thickness measured by lidars and wind-profiling radars. *J. Appl. Meteor.*, 39:1233–1247, 2000.

[29] S. A. Cohn, S. D. Mayor, C. J. Grund, T. M. Weckwerth, and C. Senff. The lidars in flat terrain (LIFT) experiment. *Bull. Amer. Meteor. Soc.*, 79:1329–1343, 1998.

[30] A. K. Cousins. Temperature and thermal stress scaling in finite-length end-pumped laser rods. *IEEE J. Quantum Electron.*, 28:1057–1069, 1992.

[31] J. Czochralski. Ein neues Verfahren zur Messung des Kristallisations−geschwindigkeit der Metalle. *Z. phys. Chemie*, 92:219–221, 1918.

[32] S. De Silvestri, P. Laporta, and V. Magni. Misalignment sensitivity of solid-state laser resonators with thermal lensing. *Opt. Commun.*, 59:43–48, 1986.

[33] J. J. Degnan. Theory of the optimally coupled Q-switched laser. *IEEE J. Quantum Electron.*, 25:214–220, 1989.

[34] W. Demtroder. *Laserspektroskopie-Grundlagen und Techniken*, page 75. Springer Verlag, Berlin, 1993.

[35] N. M. Dickey and S. C. Holswade. *Laser beam shaping. Theory and technology.*, pages 349–422. Marcel Dekker, Inc., New York, 2000.

[36] K. P. Driedger, R. M. Iffländer, and H. Weber. Multirod resonators for high-power solid-state lasers with improved beam quality. *IEEE J. Quantum Electron.*, 24:665–674, 1988.

[37] G. Ehret, C. Kiemle, W. Renger, and G. Simmet. Airborne remote sensing of tropospheric water vapor with a near-infrared differential absorption lidar system. *Appl. Optics*, 32:4534–4551, 1993.

[38] H. Eilers, W. M. Dennis, W. M. Yen, S. Kück, K. Petermann, G. Huber, and W. Jia. Performance of a Cr:YAG laser. *IEEE J. Quantum Electron.*, 29:2508–2512, 1993.

[39] H. Eilers, K. R. Hoffman, W. M. Dennis, S. M. Jacobsen, and W. M. Yen. Saturation of 1.064 μm absorption in Cr, Ca:$Y_3Al_5O_{12}$ crystals. *Appl. Phys. Lett.*, 61:2958–2960, 1992.

[40] E. W. Eloranta and D. K. Forrest. Volume-imaging lidar observations of the convective structure surrounding the flight path of a flux-measuring aircraft. *J. Geophys. Res.*, 97:18383–18393, 1992.

[41] E. W. Eloranta and T. Uttal. Arctic observations with the University of Wisconsin High Spectral Resolution Lidar. In *AMS 12th Conference on Cloud Physics and Atmospheric Radiation*, Boston, 2006.

[42] J. N. Farmer, M. S. Bowers, and Jr. W. S. Scharpf. High brightness eye safe optical parametric oscillator using confocal unstable resonators. In *Advanced Solid-State Lasers, OSA TOPS*, volume 26, pages 567–571. Optical Society of America,Washington D.C., 1999.

[43] B. J. Finlayson-Pitts and Jr. J. N. Pitts. *Chemistry of the upper and lower atmosphere*. Academic press, 2000.

[44] P. M. W. French, N. H. Rizvi, J. R. Taylor, and A. V. Shestakov. Continuous-wave mode-locked Cr^{4+}:YAG laser. *Opt. Lett.*, 18:39–41, 1993.

[45] E. Georgiou, O. Musset, J. P. Boquillon, B. Denker, and S. E. Sverchkov. 50 mJ/ 30 ns FTIR Q-switched diode-pumped Er:Yb:glass 1.54 μm laser. *Opt. Commun.*, 198:147, 2001.

[46] A. Gerrard and J. M. Burch. *Introduction to matrix methods in optics*, page 251. John Wiley & Sons, Ltd., London, 1975.

[47] A. Giez, G. Ehret, R. L. Schwiesow, K. J. Davis, and D. H. Lenschow. Water vapor flux measurements from ground-based vertically pointing water vapor differential absorption and Doppler lidars. *J. Atmos. Ocean. Technol.*, 16:237–250, 1999.

[48] C. J. Grund, R. M. Banta, Joanne L. George, James N. Howell, Madison J. Post, Ronald A. Richter, and Ann M. Weickman. High-resolution Doppler lidar for boundary layer and cloud research. *J. Atmos. Ocean. Technol.*, 18:376–393, 2001.

[49] C. J. Grund and E. W. Eloranta. University of Wisconsin high spectral resolution lidar. *Opt. Eng.*, 30:6–12, 1991.

[50] S. Guch and C. Jones. Alexandrite–laser performance at high temperature. *Opt. Lett.*, 7:608–610, 1982.

[51] G. Hansson, H. Karlsson, and F. Laurell. Unstable resonator optical parametric oscillator based on quasi-phase-matched $RbTiOAsO_4$. *Appl. Optics*, 40:5446–5451, 2001.

[52] R. Häring, R. Paschotta, R. Fluck, E. Gini, H. Melchior, and U. Keller. Passively Q -switched microchip laser at 1.5 μm. *J. Opt. Soc. Am. B*, 18:1805–1812, 2001.

[53] S. R. Harrell, W. Wilcox, D. Killinger, G. A. Rines, and R. Schwarz. High-power, eye-safe 1.57 μm OPO lidar for atmospheric boundary layer measurements. *Proc. SPIE*, 2366:354–357, 1995.

[54] R. Hauck, H. P. Kortz, and H. Weber. Misalignment sensitivity of optical resonators. *Appl. Optics*, 19:598–601, 1980.

[55] E. Hecht. *Optics*, page 604. Addison Wesley Longman, Inc., 1998.

[56] E. Hecht. *Optics*, page 465. Addison Wesley Longman, Inc., 1998.

[57] S. W. Henderson, C. P. Hale, J. R. Magee, M. J. Kavaya, and A. V. Huffaker. Eye-safe coherent laser radar system at 2.1 micron using Tm, Ho:YAG lasers. *Opt. Lett.*, 16:773–775, 1991.

[58] N. S. Higdon, E. V. Browell, P. Ponsardin, B. E. Grossmann, C. F. Butler, T. H. Chyba, M. N. Mayo, R. J. Allen, A. W. Heuser, W. B. Grant, S. D. Mayor, and A. F. Carter. Airborne differential absorption lidar system for measurements of atmospheric water vapor and aerosols. *Appl. Optics*, 33:6422–6438, 1994.

[59] I. J. Hodgkinson and J. I. Vukusic. Birefringent filters for tuning flashlamp-pumped dye lasers: simplified theory and design. *Appl. Optics*, 17:1944–1948, 1978.

[60] N. Hodgson and H. Weber. *Optical resonators: fundamentals, advanced concepts and applications*, pages 7–53. Springer-Verlag, London, 1997.

[61] R. F. Hotz. Thermal transient effects in repetitively pulsed flashlamp-pumped YAG:Nd and YAG:Nd, Lu laser material. *Appl. Optics*, 12:1834–1838, 1973.

[62] B. Humbert and A. Burneau. Jones matrices of tilted birefringent plates in a tunable dye laser: modes at low gain and temperature effect. *Appl. Optics*, 31:7022–7027, 1992.

[63] J. T. Hunt, J. A. Glaze, W. W. Simmons, and P. A. Renard. Suppression of self-focusing through low-pass spatial filtering and relay imaging. *Appl. Optics*, 17:2053, 1978.

[64] M. E. Innocenzi, H. T. Yura, C. L. Fincher, and R. A. Fields. Thermal modeling of continuous-wave end-pumped solid-state lasers. *Appl. Phys. Lett.*, 56:1831–1833, 1990.

[65] Intergovernmental Panel on Climate Change IPCC. Climate Change 2007– The physical science basis: Contribution of working group I to the Forth Assesment Report of IPCC. Technical report, 2007.

[66] International Organization for Standardization ISO. Lasers and laser-related equipment −Test methods for laser beam widths, divergence angles and beam propagation ratios −Part1: Stigmatic and simple astigmatic beams. Technical Report ISO: 11146-1, 2005.

[67] Y. Kalisky. Cr^{4+}-doped crystals: their use as lasers and passive Q–switches. *Progress in Quant. Electron.*, 28:249–303, 2004.

[68] C. Kiemle, G. Ehret, A. Giez, K. J. Davis, D. H. Lenschow, and S. P. Oncley. Estimation of boundary layer humidity fluxes and statistics from airborne differential absorption lidar (DIAL). *J. Geophys. Res.*, 102:29189–29204, 1999.

[69] M.V. Klein and T. E. Furtak. *Optik*, page 362. Springer Verlag, Berlin, 1988.

[70] W. Koechner. Absorbed pump power, thermal profile and stresses in a cw pumped Nd:YAG crystal. *Appl. Optics*, 9:1429–1434, 1970.

[71] W. Koechner. Thermal lensing in a Nd:YAG laser rod. *Appl. Optics*, 9:2548–2553, 1970.

[72] W. Koechner. *Solid-state laser engineering*, page 216. Springer series in optical sciences, New York, 1989.

[73] W. Koechner. *Solid-state laser engineering*, page 236. Springer series in optical sciences, New York, 1989.

[74] W. Koechner. *Solid-state laser engineering*, pages 406–468. Springer series in optical sciences, New York, 1989.

[75] W. Koechner. *Solid-state laser engineering*, page 48. Springer series in optical sciences, New York, 1989.

[76] H. Kogelnik. Imaging of optical modes-resonators with internal lenses. *Bell System Technical Journal*, 44:455–494, 1965.

[77] H. Kogelnik. On the propagation of Gaussian beams of light through lenslike media including those with a loss or gain variation. *Appl. Optics*, 4:1562–1569, 1965.

[78] H. Kogelnik and T. Li. Laser beams and resonators. *Appl. Optics*, 5:1550–1567, 1966.

[79] H. P. Kortz and H. Weber. Diffraction losses and mode structure of equivalent TEM_{00} optical resonators. *Appl. Optics*, 20:1936–1940, 1981.

[80] V. A. Kovalev and W. E. Eichinger. *Elastic lidar-theory, practice, and analysis methods*. John Wiley & Sons, Inc., Hobboken, New Jersey, 2004.

[81] V. Kubeček, H. Jelínková, Y. Takagi, A. Agnesi, and M. R. Kokta. Continuously pumped Cr:YAG laser. *Proc. SPIE*, 4016:354–359, 2000.

[82] S. Kück. *Spektroskopie und Lasereigenschaften von* Cr^{4+}*-dotierten oxidischen Kristallen*. PhD thesis, University of Hamburg, Hamburg, Germany, 1994.

[83] S. Kück. Laser - related spectroscopy of ion-doped crystals for tunable solid-state crystals. *Appl. Phys. B*, 72:515–562, 2001.

[84] S. Kück, K. Peterman, and G. Huber. Spectroscopic investigation of the Cr^{4+}-center in YAG. *OSA Proceedings on Advanced Solid-State Lasers*, 10:92–94, 1991.

[85] S. Kück, K. Peterman, U. Pohlmann, U. Schönhoff, and G. Huber. Tunable room-temperature laser action of Cr^{4+}-doped $Y_3Sc_xAl_{5-x}O_{12}$. *Appl. Phys. B*, 58:153–156, 1994.

[86] S. Kück, K. Petermann, U. Pohlmann, and G. Huber. Near-infrared emission of Cr^{4+}-doped garnets: Lifetimes, quantum efficiencies, and emission cross sections. *Phys. Rev. B*, 51:17323–17331, 1995.

[87] S. Kück, K. Petermann, U. Pohlmann, and G. Huber. Electronic and vibronic transitions of the Cr^{4+}-doped garnets $Lu_3Al_5O_{12}$, $Y_3Al_5O_{12}$, $Lu_3Ga_5O_{12}$. *J. Lumin.*, 68:1–14, 1996.

[88] K. E. Kunkel, E. W. Eloranta, and S. T. Shipley. Lidar observations of the convective boundary layer. *J. Appl. Meteor.*, 16:1306–1311, 1977.

[89] A. A. Lagatsky, C. T. A. Brown, W. Sibbett, and W. Knox. Self-starting passively mode-locked femtosecond Cr^{4+}:YAG laser diode pumped by a Yb-fiber. In *OSA Trends in Optics and Photonics (TOPS)*, volume 73 of *Conference on Lasers and Electro-Optics, OSA Technical Digest*, pages 339–340. Optical Society of America, Washington D.C., 2002.

[90] A. A. Lagatsky, Leburn, C. T. A. Brown, W. Sibbett, and W. H. Knox. Compact self-starting femtosecond Cr^{4+}:YAG laser diode pumped by a Yb-fiber. *Opt. Commun.*, 217:363–367, 2003.

[91] A. Lavrov, A. B. Utkin, R. Vilar, and A. Fernandes. Application of lidar in ultraviolet, visible and infrared ranges for early forest fire detection. *Appl. Phys. B*, 76:87–95, 2003.

[92] U. Lohmann and J. Feichter. Global indirect aerosol effects: a review. *Atmos. Chem. Phys.*, 5:715–737, 2005.

[93] J. P. Lörtscher, J. Steffen, and G. Herziger. Dynamic stable resonators: a design procedure. *Optical and Quantum Electronics*, 7:505–514, 1975.

[94] M. Lothon, D. H. Lenschow, and S. D. Mayor. Coherence and scale of vertical velocity in the convective boundary layer from a doppler lidar. *Bound. Layer Meteor.*, 121:521–536, 2006.

[95] J. L. Machol, T. Ayers, K. T. Schwenz, K. W. Koenig, R. M. Hardesty, C. J. Senff, M. A. Krainak, J. B. Abshire, H. E. Bravo, and S. P. Sandberg. Preliminary measurements with an automated compact differential absorption lidar for profiling water vapor. *Appl. Optics*, 43:3110–3121, 2004.

[96] V. Magni. Resonators for solid-state lasers with large-volume fundamental mode and high alignment stability. *Appl. Optics*, 25:107–117, 1986.

[97] V. Magni. Multielement stable resonators containing a variable lens. *J. Opt. Soc. Am. A*, 4:1962–1969, 1987.

[98] V. Magni, G. Valentini, and S. De Silvestri. Recent developments in laser resonator design. *Optical and Quantum Electronics*, 23:1105–1134, 1991.

[99] P. Mahnke, H. H. Klingenberg, A. Fix, and M. Wirth. Investigation of a KTP optical parametric oscillator. In *Conference on Lasers and Electro-Optics/Quantum Electronics and Laser Science Conference and Photonic Applications Systems Technologies*, pages 8–16. Optical Society of America, Washington D.C., 2006.

[100] P. Mamidipudi and D. Killinger. Optimal detector selection for a 1.5 micron KTP OPO atmospheric lidar. In *SPIE Conference on Laser Radar Technology and Applications IV*, volume 3707, pages 327–335. SPIE, 1999.

[101] P Mathieu, A. Parent, K. Snell, and D. Peressini. Tunable gain-switched chromium YAG laser. *Proc. SPIE*, 2041:348–356, 1994.

[102] S. D. Mayor and E. W. Eloranta. Two-dimensional vector wind fields from volume imaging lidar data. *J. Appl. Meteor.*, 40:1331–1346, 2001.

[103] S. D. Mayor and S. M. Spuler. Raman-shifted eye-safe aerosol lidar (REAL). *Appl. Optics*, 43:3915–3924, 2004.

[104] S. D. Mayor, G. J. Tripoli, and E. W. Eloranta. Evaluating large-eddy simulations using volume imaging lidar. *Mon. Wea. Rev.*, 131:1428–1452, 2003.

[105] A. J. McGrath, J. Munch, G. Smith, and P. Veitch. Injection-seeded, single-frequency, Q–switched Erbium:glass laser for remote sensing. *Appl. Optics*, 37:5706–5709, 1998.

[106] I. T. McKinnie and M. J. Davis. Temporal characteristics and dynamics of gain-switched Cr:YAG lasers. *Pure Appl. Opt.*, 6:759–772, 1997.

[107] I. T. McKinnie, J. C. Diettrich, R. T. White, and D. M. Warrington. Dynamics of gain-switched Cr:YAG lasers. *Proc. SPIE*, 3265:295–305, 1998.

[108] R. Measures. *Laser remote sensing- fundamentals and applications*. Krieger Publishing Company, Malabar, Florida, 1984.

[109] I. J. Miller, A. J. Alcock, and J. E. Bernard. Experimental investigation of Cr^{4+} in YAG as a passive Q–switch. In *OSA Proceedings Series*, volume 13 of *Advanced Solid-State Lasers*, pages 322–325, 1992.

[110] M. I. Mishchenko, J. W. Hovenier, and L. D. Travis (Eds.). *Light scattering by nonspherical particles: theory, measurements, and applications*. Academic Press, San Diego, 2000.

[111] J. E. Murray, D. Milam, C. D. Boley, K. G. Estabrook, and J. A. Caird. Spatial filter pinhole development for the National Ignition Facility. *Appl. Optics*, 39:1405–1420, 2000.

[112] J. T. Murray, R. C. Powell, N. Peyghambarian, D. Smith, W. Austin, and R. A. Stolzenberger. Generation of 1.5-μm radiation through intracavity solid-state raman shifting in $Ba(NO_3)_2$ nonlinear crystals. *Opt. Lett.*, 20:1017–1019, 1995.

[113] A. G. Okhrimchuk and A. V. Shestakov. Performance of YAG:Cr^{4+} laser crystal. *Opt. Mater.*, 3:1–13, 1994.

[114] A. G. Okhrimchuk and A. V. Shestakov. Absorption saturation mechanism for YAG:Cr^{4+} crystals. *Phys. Rev. B*, 61:988–995, 2000.

[115] M. Ostermeyer, P. Kappe, R. Menzel, and V. Wulfmeyer. Diode pumped nd:yag mopa with high pulse energy, excellent beam quality and frequency stabilized master oscillator as a basis for a next generation lidar system. *Appl. Optics*, 44:582–590, 2005.

[116] N. Pavel, T. Dascalu, and V. Lupei. Stable resonators for fundamental mode operation. *Opt. Eng.*, 35:1239–1246, 1996.

[117] A. Peters and D. W. Dockery. Air pollution and health effects: Evidence from epidemiologic studies. *Lung Biology in Health and Disease*, 204:1–19, 2005.

[118] A. K. Piironen and E. W. Eloranta. An accuracy analysis of wind profiles calculated from volume imaging lidar data. *J. Geophys. Res.*, 100:25559–25567, 1995.

[119] A. V. Podlipensky, V. G. Shcherbitsky, N. V. Kuleshov, V. P. Mikhailov, V. I. Levchenko, and V. N. Yakimovich. Cr^{2+}ZnSe and Co^{2+}ZnSe saturable-absorber Q switches for 1.54-μm Er:glass lasers. *Opt. Lett.*, 24:960–962, 1999.

[120] M. J. Post and R. E. Cupp. Optimizing a pulsed Doppler lidar. *Appl. Optics*, 29:4115–4158, 1990.

[121] D. R. Preuss and J. L. Gole. Three-stage birefringent filter tuning smoothly over he visible region: theoretical treatment and experimental design. *Appl. Optics*, 19:702–710, 1980.

[122] D. A. Richter, N. S. Higdon, P. Ponsardin, D. Sanchez, T. H. Chyba, D. A. Temple, W. Gong, R. Battle, M. Edmondson, A. Futrell, D. Harper, L. Haughton, D. Johnson, K. Lewis, and R. S. Payne-Baggott. Design validation of an eye-safe scanning aerosol lidar with the Center for Lidar and Atmospheric Sciences students (CLASS) at Hampton University. In *Lidar Remote Sensing for Industry and Environment Monitoring* II, volume 4484, pages 8–16. SPIE, 2002.

[123] N. W. Rimington, S. L. Schieffer, and W. A. Schroeder. Thermal lens shaping in Brewster gain media: a high power, diode-pumped Nd:$GdVO_4$ laser. *Optics Express*, 12:1426–1436, 2004.

[124] L. S. Rothman, C. P. Rinsland, A. Goldman, S. T. Massie, D. P. Edwards, J. M. Flaud, A. Perrin, C. Camy-Peyret, V. Dana, J. Y. Mandin, J. Schroeder, A. McCann, R. R. Gamache, R. B. Wattson, K. Yoshino, K. V. Chance, K. W. Jucks, L. R. Brown, V. Nemtchinov, and P. Varanasi. The HITRAN molecular spectroscopic database. *Journal of Quantitative Spectroscopy & Radiative Transfer*, 60:665–710, 1996.

[125] K. Sassen. The polarization lidar technique for cloud research: a review and current assessment. *Bull. Amer. Meteor. Soc.*, 72:1848–1866, 1991.

[126] Research Division Schwartz Elecro-Optics Inc. High-energy, eye-safe lidar for long-range, high-resolution aerosol detection. Technical report, final report for period from 22 March 1995 to 31 December 1997, contract NAS1-20476 [Phase II, Small Business Innovative Research (SBIR)], prepared for NASA Langley Research Center, Research Division Schwartz Elecro-Optics, Inc., 135 South Road, Bedford, Mass. 01730, 1997.

[127] S. E. Schwarz. The whitehouse effect–shortwave radiative forcing of climate by anthropogenic aerosols. An overview. *J. Atmos. Sci.*, 27:359–382, 1996.

[128] C. J. Senff, R. M. Hardesty, R. J. Alvarez, and S. D. Mayor. Airborne lidar characterization of power plant plumes during the 1995 southern oxidants study. *J. Geophys. Res.*, 103:31173–31189, 1998.

[129] A. Sennaroglu. Continuous-wave power transmission and thermal lensing of a saturable absorber subject to excited-state absorption. *Appl. Optics*, 38:3334–3337, 1999.

[130] A. Sennaroglu. Broadly tunable Cr^{4+}-doped solid-state lasers in the near infrared and visible. *Progress in Quant. Electron.*, 26:287–352, 2002.

[131] A. Sennaroglu and C. R. Pollock. Efficient continuous-wave chromium-doped YAG laser. *J. Opt. Soc. Am. B*, 12:930–937, 1995.

[132] M. L. Shand and H. P. Jenssen. Temperature dependence of the excited-state absorption of alexandrite. *IEEE J. Quantum Electron.*, 19:480–484, 1983.

[133] Y. Shimony, Z. Burshtein, and Y. Kalisku. Cr^{4+}:YAG as passive Q–switch and brewster plate in a pulsed nd:yag laser. *IEEE J. Quantum Electron.*, 31:1738–1741, 1995.

[134] A. E. Siegman. *Lasers*, page 491. University Science Books, Sausalito, CA, 1986.

[135] A. E. Siegman. *Lasers*, page 316. University Science Books, Sausalito, CA, 1986.

[136] A. E. Siegman. *Lasers*, page 465. University Science Books, Sausalito, CA, 1986.

[137] A. E. Siegman. *Lasers*, page 266. University Science Books, Sausalito, CA, 1986.

[138] A. E. Siegman. *Lasers*, page 626. University Science Books, Sausalito, CA, 1986.

[139] A. E. Siegman. *Lasers*, page 682. University Science Books, Sausalito, CA, 1986.

[140] A. E. Siegman. *Lasers*, page 690. University Science Books, Sausalito, CA, 1986.

[141] A. E. Siegman. How to (maybe) measure laser beam quality. In M. W. Dowley, editor, *DPSS Lasers: Applications and Issues (OSA TOPS)*, volume 17, pages 184–199. Optical Society of America,Washington D.C., 1998.

[142] A. V. Smith and D. J. Armstrong. Nanosecond optical parametric oscillator with 90° image rotation: design and performance. *J. Opt. Soc. Am. B*, 19:1801–1814, 2002.

[143] I. T. Sorokina, S. Naumov, E. Sorokin, E. Wintner, and A. V. Shestakov. Directly diode-pumped tunable continuous-wave room-temperature Cr^{4+}:YAG laser. *Opt. Lett.*, 22:1578–1580, 1999.

[144] K. Spariosu, W. Chen, R. Stulyz, and M. Birnbaum. Dual Q switching and laser action at 1.06 and 1.44 μm in a Nd^{4+}:YAG–Cr^{4+}:YAG oscillator at 300 K. *Opt. Lett.*, 10:814–816, 1993.

[145] J. D. Spinhirne. Micro pulse lidar. *IEEE Trans. Geosci. Remote Sens.*, 31:48–55, 1993.

[146] J. D. Spinhirne, S. Chudamani, J. F. Cavanaugh, and J. L. Bufton. Aerosol and cloud backscatter at 1.06, 1.54, and 0.53 μm by airborne hard-target-calibrated Nd:YAG/methane Raman lidar. *Appl. Optics*, 36:3475–3490, 1997.

[147] M. S. Spuler and S. D. Mayor. Raman-shifter optimized for lidar at 1.5 μm wavelength. *Appl. Optics*, 46:2990–2995, 2007.

[148] S. M. Spuler and S. D. Mayor. Scanning eye-safe elastic backscatter lidar at 1.54 microns. *J. Atmos. Ocean. Technol.*, 22:696–703, 2005.

[149] J. T. Sroga, E. W. Eloranta, and T. Barber. Lidar measurements of wind velocity profiles in the boundary layer. *J. Appl. Meteor.*, 19:598–605, 1980.

[150] B. Stevens and D. H. Lenschow. Observations, experiments, and large eddy simulations. *Bull. Amer. Meteor. Soc.*, 82:283–294, 2001.

[151] D. H. Stone and M. D. Rotondaro. Transient thermal-lensing effects on the performance of repetitively pulsed solid-state lasers. *Appl. Optics*, 31:1314–1317, 1992.

[152] R. B. Stull. *An introduction to boundary layer meteorology*. Kluwer Academic Publishers, Dordrecht, 1988.

[153] A. Suda, A. Kadoi, K. Nagasaka, H. Tashiro, and K. Midorikawa. Absorption and oscillation characteristics of a pulsed Cr^{4+}:YAG laser investigated by a double-pulse pumping technique. *IEEE J. Quantum Electron.*, 35:1548–1553, 1999.

[154] G. I. Taylor. The spectrum of turbulence. *Proc. R. Soc. A*, 164:476–490, 1938.

[155] M. M. Tilleman and S. M. Jackeland I. Moshe. High-power, high-fracture-strength, eye-safe Er:glass laser. *Opt. Eng.*, 37:2512–2520, 1998.

[156] S. Twomey. The nuclei of natural cloud formation, part II: The supersaturation in natural clouds and the variation of cloud droplet concentration. *Geofis. Pura Appl.*, 43:243–249, 1959.

[157] S. Twomey. Aerosols, clouds, and radiation. *Atmos. Environ.*, 25:2435–2442, 1991.

[158] H. C. Van de Hulst. *Light scattering by small particles*. Dover, New York, 1981.

[159] A. Vilar and A. Lavrov. Estimation of required parameters for detection of small smoke plumes by lidar at 1.54 μm. *Appl. Phys. B*, 71:225–229, 2000.

[160] G. Wagner, M. Shiler, and V. Wulfmeyer. Simulations of thermal lensing of a Ti:Sapphire crystal end-pumped with high average power. *Optics Express*, 13:8045–8055, 2005.

[161] X. Wang and J. Yao. Transmitted and tuning characteristics of birefringent filters. *Appl. Optics*, 31:4505–4508, 1992.

[162] T. Warner, P. Benda, S. Swerdlin, J. Knievel, E. Argenta, B. Aronian, B. Balsley, J. Bowers, R. Carter, P. A. Clark, K. Clawson, J. Copeland, A. Crook, R. Frehlich, M. L. Jensen, S. Mayor Y. Liu, Y. Meillier, B. Morley, R. Sharman, S. Spuler, D. Storwold, J. Sun, J. Weil, M. Xu, A. Yates, and Y. Zhang. The Pentagon shield field program toward critical infrastructure protection. *Bull. Amer. Meteor. Soc.*, 88:167–176, 2007.

[163] M. S. Webb, P. F. Moulton, J. J. Kasinski, R. I. Burnham, G. Loiacono, and R. Stolzenberger. High-average-power $KTiOAsO_4$ optical parametric oscillator. *Opt. Lett.*, 23:1161–1163, 1998.

[164] T. M. Weckwerth and D. B. Parsons. A review of convection initiation and motivation for IHOP_2002. *Mon. Wea. Rev.*, 134:5–22, 2006.

[165] T. M. Weckwerth, D. B. Parsons, S. E. Koch, J. A. Moore, M. A. LeMone, B. B. Demoz, C. Flamant, B. Geerts, J. H. Wang, and W. F. Feltz. An overview of the international H_2O project (IHOP_2002) and some preliminary highlights. *Bull. Amer. Meteor. Soc.*, 85:253, 2004.

[166] T. M. Weckwerth, V. Wulfmeyer, R. M. Wakimoto, R. M. Hardesty, J. W. Wilson, and R. M. Banta. NCAR/ NOAA lower-tropospheric water vapor workshop. *Bull. Amer. Meteor. Soc.*, 80:2339–2357, 1999.

[167] C. Weitkamp (Ed.). *Lidar: range-resolved optical remote sensing of the atmosphere*, page 187. Springer Science+Business Media Inc., New York, 2005.

[168] C. Weitkamp (Ed.). *Lidar: range-resolved optical remote sensing of the atmosphere*, page 325. Springer Science+Business Media Inc., New York, 2005.

[169] C. Weitkamp (Ed.). *Lidar: range-resolved optical remote sensing of the atmosphere*, page 6. Springer Science+Business Media Inc., New York, 2005.

[170] D. Welford and A. Jaspan. Single-frequency operation of a Cr^{4+}:YAG laser from 1332 to 1554 nm. *J. Opt. Soc. Am. B*, 21:2137–2141, 2004.

[171] World Health Organization (WHO). Air quality guidelines. Global update 2005. Particulate matter, ozone, nitrogen dioxide and sulfur dioxide. Technical report, WHO Regional Office for Europe, 2006.

[172] R. Wu, J. D. Myers, and M. J. Myers. In *Advanced Solid State Lasers, OSA TOPS*, volume 26, 1999.

[173] V. Wulfmeyer. *DIAL-Messungen von vertikalen Wasserdampfverteilungen. Ein Lasersystem für Wasserdampf- und Temperaturmessungen in der Troposphäre.* PhD thesis, University of Hamburg, Hamburg, Germany, 1995.

[174] V. Wulfmeyer. Ground-based differential absorption lidar for water-vapor and temperature: development and specifications of a high-performance laser transmitter. *Appl. Optics*, 37:3804–3824, 1998.

[175] V. Wulfmeyer. Investigation of turbulent processes in the lower troposphere with water-vapor DIAL and radar-RASS. *J. Atmos. Sci.*, 56:1055–1076, 1999.

[176] V. Wulfmeyer. Investigations of humidity skewness and variance profiles in the convective boundary layer and comparison of the latter with large eddy simulation results. *J. Atmos. Sci.*, 56:1077–1087, 1999.

[177] V. Wulfmeyer, H. S. Bauer, S. Crewell, G. Ehret, O. Reitebuch, C. Werner, M. Wirth, D. Engelbart, A. Rhodin, W. Wergen, A. Giesen, H. Grassl, G. Huber, H. Klingenberg, P. Mahnke, U. Kummer C. Wuhrer, P. Ritter, R. Wallenstein, and U. Wandinger. Lidar research network water vapor and wind. *Meteorologische Zeitschrift*, 12:15–24, 2003.

[178] V. Wulfmeyer and J. Bösenberg. Ground-based differential absorption lidar for water-vapor profiling: assessment of accuracy, resolution and meteorological applications. *Appl. Optics*, 37:3825–3844, 1998.

[179] V. Wulfmeyer and J. Bösenberg. Ground-based differential absorption lidar for water-vapor profiling: assessment of accuracy, resolution and meteorological applications. *Appl. Optics*, 37:3825–3844, 1998.

[180] V. Wulfmeyer, M. Randall, A. Brewer, and R. M. Hardesty. 2-micron Doppler lidar transmitter with high frequency stability and low chirp. *Opt. Lett.*, 25:1228–1230, 2000.

[181] V. Wulfmeyer and C. Walther. Future performance of a ground-based and airborne water-vapor differential absorption lidar. I. Overview and theory. *Appl. Optics*, 40:5304–5320, 2001.

[182] V. Wulfmeyer and C. Walther. Future performance of a ground-based and airborne water-vapor differential absorption lidar. II. Simulations of the precision of a near-infrared, high-power system. *Appl. Optics*, 40:5321–5336, 2001.

[183] T. Yanagisawa, K. Asaka, K. Hamazu, and Y. Hirano. 11-mJ, 15-Hz single-frequency diode-pumped Q -switched Er, Yb:phosphate glass laser. *Opt. Lett.*, 26:1262–1264, 2001.

[184] G. M. Zverev and A. V. Shestakov. Tunable near-infrared oxide crystal lasers. In M. Shand and H. P. Jenssen, editors, *OSA Proceedings Series*, volume 5 of *Tunable Solid-State Lasers*, pages 66–70. Optical Society of America, Washington D.C., 1989.